To the Graduate Council:

I am submitting herewith a dissertation written by Richard Anton Marschall entitled "Aspects of the Numerical Solution of the Helmholtz Equation." I have examined the final copy of this dissertation for form and content and recommend that it be accepted in partial fulfillment of the requirements for the degree of Doctor of Philosophy, with a major in Engineering Science.

John E. Caruthers

John E. Caruthers, Major Professor

We have read this dissertation
and recommend its acceptance:

Dennis Keefer

Bruce Bowman

R. Snyder

Accepted for the Council:

C W Minkel

Associate Vice Chancellor
and Dean of The Graduate School

ASPECTS OF THE NUMERICAL SOLUTION OF THE HELMHOLTZ EQUATION

A Dissertation

Presented for the

Doctor of Philosophy

Degree

The University of Tennessee, Knoxville

Richard Anton Marschall

May 1993

Copyright © Richard Anton Marschall, 1993

All rights reserved under International and Pan-American Copyright Conventions. This work may not be translated or copied in whole or in part without the written permission of the copyright holder (Richard A. Marschall, Marschall Acoustics, 42 Music Square West, Suite 291, Nashville, Tennessee 37203 USA), except for brief excerpts in connection with reviews or scholarly analysis. Use in connection with any form of information storage and retrieval, electronic adaptation, computer software, or by similar or dissimilar methodology now known or hereafter developed is forbidden. Processes, algorithms, and technologies described in this document may be protected by patents, both U.S. and foreign. This document conveys no license in algorithms described or in the technology disclosed.

ACKNOWLEDGMENTS

The training of a doctoral engineer is a long and expensive process. Many people share in the development of this expertise, and the molding of outlook and approach. Professors whose lessons have stood the test of time and have been especially applicable to the formulation of this work include Dr. Eugene Zaustinsky, Dr. Richard Dollinger, and Dr. Demetrios Kazakos, then all with the State University of New York. Dr. Kazakos continued to teach me signal analysis up to an advanced level when we were both at the University of Virginia. This preparation in particular, together with additional signal analysis instruction from Dr. Bruce Bomar of the University of Tennessee, enabled me to create the heart of this dissertation.

After my arrival at the University of Tennessee, Dr. Dennis Keefer was quick to show me where the gaps in my background were, as well as how to fill them. My advisor, Dr. John Caruthers, lead the effort to strengthen my theoretical background in acoustics. Chapter 1 of this dissertation is a result of this work and will be appearing as a separate journal article by Dr. Caruthers and me. Assistance in areas ancillary to acoustics, structural vibrations and discrete time signal processing, was provided by Dr. Remi Engels and Dr. Montgomery Smith, respectively. Drs. Donald Tippett and Max Hailey provided me with the project management skills to complete the Ph.D. program in a timely manner.

I would like to thank my committee, Drs. Bruce Bomar, John Caruthers, Remi Engels, and Dennis Keefer, for their concern and guidance, and for their close reading of the draft. Additionally, I wish to thank my advisor not only for his encouragement of independence, but also for his helpful brain-storming sessions.

ABSTRACT

A straightforward and robust Boundary Element Method (BEM) for the numerical solution of the exterior Helmholtz problem is specified. The BEM algorithm employs the Combined Helmholtz Integral Equation Formulation (CHIEF) and then Singular Value Decomposition (SVD) to solve the resulting system. Its accuracy and convergence characteristics are examined and compared to the simplest boundary element method for exterior problems, the Helmholtz Integral Equation Formulation or HIEF. The CHIEF algorithm described is found to largely avoid the numerical difficulties of the HIEF technique while retaining theoretical and practical implementation simplicity.

An algorithm of order $N\log_2 N$ for numerically finding Green's functions in general inhomogeneous media is developed. This method is referred to as the Iterative Dual Domain Method, or IDDM, since iterations occur in both transformed and untransformed domains. The algorithm's performance is demonstrated by examples of: wave focusing through a thick lens, scattering from an inclusion, and guided waves in layered media.

The appropriate conditions under which to combine IDDM with BEM to solve many inhomogeneous media wave propagation problems are described. Problems for which the IDDM can be best used alone are outlined.

PREFACE

This dissertation deals with the numerical solution of linear partial differential equations, specifically the Helmholtz equation. The Helmholtz equation was chosen since it models a broad range of energy and wave propagation problems of present physical interest. The methods presented, however, readily extend to other classes of partial differential equations. Application to Laplace's equation, for example, would be very simple.

Chapter 1 presents a straightforward and robust Boundary Element Method (BEM) in sufficient detail to allow non-experts in BEM to develop their own implementations and variations. The boundary element and auxiliary point requirements to obtain BEM solutions of a desired accuracy are described.

A fast numerical method using inverse fast Fourier transforms, IFFTs, for finding Green's functions in a homogeneous media is developed in Chapter 2. The necessary background for understanding Chapter 3 is also presented here. It is not necessary to read Chapter 1 in order to understand the material presented in Chapters 2 and 3.

Chapter 3 represents the heart of the dissertation. It presents an original algorithm, of order $N\log_2 N$ for numerically finding Green's functions in general inhomogeneous media. This method is referred to as the Iterative Dual Domain Method, or IDDM. The algorithm's performance is demonstrated by examples of: wave focusing through a lens, scattering from an inclusion, and guided waves in layered media.

Chapter 4 describes when and how to combine the BEM of Chapter 1 with the IDDM of Chapter 3 to solve many inhomogeneous media wave propagation problems. This extends the uses of the BEM considerably. The IDDM can also

be used alone, and for certain kinds of problems this is desirable. These kinds of problems are outlined. Finally, extension to higher dimensional problems is addressed and results summarized.

TABLE OF CONTENTS

Chapter		Page
1	THE BOUNDARY ELEMENT METHOD	1
	Introduction	1
	Surface Helmholtz Integral Formulation	3
	Interior Helmholtz Integrals and the CHIEF Formulation	7
	Robin Boundary Conditions	9
	Integrands for the Two-Dimensional Problem	10
	Implementation Specifics	16
	Test Cases and Exact Solution	19
	Results and Discussion	20
2	GREEN'S FUNCTIONS FOR THE HELMHOLTZ EQUATION	30
	Green's Functions	30
	Exact Green's Functions	31
	Fourier Transform Methods for Green's Functions	34
	Green's Functions by Numerical Transforms	38
3	NUMERICAL GREEN'S FUNCTIONS FOR THE INHOMOGENEOUS MEDIA HELMHOLTZ EQUATION	52
	Background	52
	A Preliminary Iterative Method	53
	The Iterative Dual Domain Method	56
	Focusing Through a Circular Lens	59
	Scattering by a Higher Speed Circular Inclusion	69
	Waves in Layered Media	79

4 INHOMOGENEOUS MEDIA GREEN'S FUNCTIONS AND THE BOUNDARY ELEMENT METHOD 90

Background 90

Inhomogeneous Media with a Strong Influence on a Body's Nearfield Radiation 91

Inhomogeneous Media with a Weak Influence on a Body's Nearfield Radiation 94

Higher Dimensions 97

Summary 97

LIST OF REFERENCES 100

VITA 110

LIST OF FIGURES

Figure		Page
1	Nomenclature for the exterior Helmholtz problem	4
2	Nomenclature for the two-dimensional boundary element method	12
3	Maximum percent amplitude errors	21
4	Maximum phase errors	22
5	Root Mean Square (RMS) percent amplitude errors	23
6	Root Mean Square (RMS) percent phase errors	24
7	Amplitude errors versus number of elements, $\kappa = 2.40483$	26
8	Amplitude errors versus number of elements, $\kappa = 5.52008$	27
9	Maximum amplitude errors versus number of CHIEF points	28
10	Maximum phase errors versus number of CHIEF points	29
11	$\Re(G)$ exact values on a 128 x 128 grid, $\kappa = 0.5 - 0.0j$	32
12	$\Im(G)$ exact values on a 128 x 128 grid, $\kappa = 0.5 - 0.0j$	33
13	$\Re(\mathcal{F}\{G\})$ computed on a 64 x 64 grid, $\kappa = 0.5 - 0.03j$	40
14	$\Im(\mathcal{F}\{G\})$ computed on a 64 x 64 grid, $\kappa = 0.5 - 0.03j$	41
15	Schematic of wrap around order	42
16	$\Re(G)$ found by IFFT on a 64 x 64 grid, $\kappa = 0.5 - 0.03j$	44
17	$\Im(G)$ found by IFFT on a 64 x 64 grid, $\kappa = 0.5 - 0.03j$	45
18	$\Re(\mathcal{F}\{G\})$ computed on a 128 x 128 grid, $\kappa = 0.5 - 0.01j$	47
19	$\Im(\mathcal{F}\{G\})$ computed on a 128 x 128 grid, $\kappa = 0.5 - 0.01j$	48
20	$\Re(G)$ found by IFFT on a 128 x 128 grid, $\kappa = 0.5 - 0.01j$	50
21	$\Im(G)$ found by IFFT on a 128 x 128 grid, $\kappa = 0.5 - 0.01j$	51

22 Variation of α in media, circle interior propagation velocity 76% of exterior 60

23 Focusing of $\Re(G)$ through circle with interior propagation velocity 76% of exterior, $\kappa_0 = 0.5 - 0.03j$ 62

24 Focusing of $\Im(G)$ through circle with interior propagation velocity 76% of exterior, $\kappa_0 = 0.5 - 0.03j$ 63

25 First quadrant of $\Re(\mathcal{F}\{G\})$ for circle with interior propagation velocity 76% of exterior, $\kappa_0 = 0.5 - 0.03j$ 65

26 First quadrant of $\Im(\mathcal{F}\{G\})$ for circle with interior propagation velocity 76% of exterior, $\kappa_0 = 0.5 - 0.03j$ 66

27 Less focusing and greater diffraction at lower frequencies, $\kappa_0 = 0.25 - 0.03j$, $\Re(G)$ through circle with interior propagation velocity 76% of exterior 67

28 Less focusing and greater diffraction at lower frequencies, $\kappa_0 = 0.25 - 0.03j$, $\Im(G)$ through circle with interior propagation velocity 76% of exterior 68

29 Variation of α in media, circle interior propagation velocity 200% of exterior 70

30 Scattering of $\Re(G)$, circle with interior propagation velocity 200% of exterior, $\kappa_0 = 0.5 - 0.03j$ 72

31 Scattering of $\Im(G)$, circle with interior propagation velocity 200% of exterior, $\kappa_0 = 0.5 - 0.03j$ 73

32 First quadrant of $\Re(\mathcal{F}\{G\})$ for circle with interior propagation velocity 200% of exterior, $\kappa_0 = 0.5 - 0.03j$ 75

33 First quadrant of $\Im(\mathcal{F}\{G\})$ for circle with interior propagation velocity 200% of exterior, $\kappa_0 = 0.5 - 0.03j$ 76

34 Diffraction of lower frequencies, $\kappa_0 = 0.25 - 0.03j$, $\Re(G)$ through circle with interior propagation velocity 200% of exterior 77

35 Diffraction of lower frequencies, $\kappa_0 = 0.25 - 0.03j$, $\Im(G)$ through circle with interior propagation velocity 200% of exterior 78

36 One-dimensional variation in media, middle layer (interior) has propagation velocity 57.7% of exterior 80

37 Wavelength of $\Re(G)$ increases in higher speed exterior media, $\kappa_0 = 0.5 - 0.055j$ 81

38 Wavelength of $\Im(G)$ increases in higher speed exterior media, $\kappa_0 = 0.5 - 0.055j$ 82

39 Slower speed interior layer begins to act as a (leaky) waveguide for $\Re(G)$ at $\kappa_0 = 0.7 - 0.07j$ 83

40 Slower speed interior layer begins to act as a (leaky) waveguide for $\Im(G)$ at $\kappa_0 = 0.7 - 0.07j$ 84

41 Guided mode behavior of $\Re(G)$ in slow speed layer at $\kappa_0 = 0.9 - 0.085j$ 86

42 Guided mode behavior of $\Im(G)$ in slow speed layer at $\kappa_0 = 0.9 - 0.085j$ 87

43 First quadrant of $\Re(\mathcal{F}\{G\})$ for layered media case with $\kappa_0 = 0.9 - 0.085j$ 88

44 First quadrant of $\Im(\mathcal{F}\{G\})$ for layered media case with $\kappa_0 = 0.9 - 0.085j$ 89

45 Borehole acoustic source example. 92

46 Sidescan sonar example. 95

NOMENCLATURE

α	Robin boundary condition constant
β	an angle
δ	delta function
ε	a small number
$\in$	an element of
θ	an angle
κ	wavenumber
λ	wavelength
ξ	real parameter
ρ	density
σ	singular values
π	mathematical constant pi
ψ	an angle
ω	radial frequency
Γ	boundary
Δ	difference, increment
Υ	undetermined complex constants
Ω_x	transformed space coordinate
Ω_z	transformed space coordinate
$\bar{\Omega}$	transformed space vector
$\jmath$	$\sqrt{-1}$
$\Re$	real part of
$\Im$	imaginary part of
∂	partial derivative

∇^2	Laplacian operator
$\forall$	for all
$\mathbf{C}$	complex numbers
$\mathbf{R}$	real numbers
$\mathbf{Z}$	integers
$\mathfrak{F}$	Fourier transform
$\mathcal{F}$	discrete Fourier transform
$\star$	convolution operator
E	exterior space
G	Green's function
$\tilde{G}$	matrix used in CHIEF
$\mathbf{G}$	matrix of integrals of Green's functions
H	Hankel functions
$\tilde{H}$	matrix used in CHIEF
$\mathbf{H}$	matrix of normal derivatives of Green's functions
I	final index, also interior space
J	Bessel functions of the first kind
L	final index
M	final index
N	final index
R	final index
$\mathbf{S}$	matrix of singular values
$\mathbf{T}$	transpose operator
$\mathbf{U}$	a matrix used in singular value decomposition
$\mathbf{V}$	a matrix used in singular value decomposition
Y	Bessel functions of the second kind

$\bar{b}$	a vector
c	wave propagation speed
d	differential operation
f	a function
g	Fourier transform of the Green's function
$\tilde{g}$	element of $\tilde{G}$ matrix
$\tilde{h}$	element of $\tilde{H}$ matrix
i	index
j	index
k	index
ℓ	index
m	index
n	index, also a normal
p	index
$\bar{q}$	a point
r	a radius
u	the potential function
$\bar{u}$	vector of potentials
x	spatial coordinate
y	spatial coordinate
z	spatial coordinate
AEDC	Arnold Engineering Development Center
BEM	Boundary Element Method
BIE	Boundary Integral Equation
CHIEF	Combined Helmholtz Integral Equation Formulation
FEM	Finite Element Method

FFT	Fast Fourier Transform
HIEF	Helmholtz Integral Equation Formulation
IDDM	Iterative Dual Domain Method
IFFT	Inverse Fast Fourier Transform
SVD	Singular Value Decomposition

CHAPTER 1

THE BOUNDARY ELEMENT METHOD

INTRODUCTION

The proposition that the equation describing the acoustic velocity potential, i.e. the Helmholtz equation:

$$\nabla^2 u + \kappa^2 u = 0. \tag{1}$$

where u is the velocity potential and κ is the wavenumber, could be solved in terms of boundary integral equations by use of Green's theorems was put forth by H. Helmholtz in 1859 [1]. The observation that the solution of the resulting Boundary Integral Equations, as they are now called, are indeterminant at "values of κ corresponding to the periods of the possible modes of simple harmonic vibration which may take place within a closed rigid envelope having the form" of the boundary surface was reported by J. W. S. Rayleigh in 1877 [2]. By 1932, H. Lamb [3] described these phenomena in somewhat more precise mathematical terms, and observed the difficulties in solving exterior problems with boundary integral equations at the eigenvalues of the corresponding interior problem. These existence and uniqueness issues are discussed at length in the 1958 paper by R. Leis [4].

As the first solid-state electronic computers appeared in the early 1960s, it became feasible to discretize these classical boundary integral equations. Various approaches were tried and have been reported by L. H. Chen and D. G. Schweikart [5], G. Chertock [6], G. B. Brundrit [7], and L. G. Copley [8], among others.

Many techniques to avoid possible non-uniqueness and non-existence problems with numerical boundary integral equation formulations have emerged since the early 1960s. H. A. Schenck published a technique in 1967 [9] that he called the Combined Helmholtz Integral Equation Formulation or CHIEF. The CHIEF method combines discretized surface and interior Helmholtz integral equations to obtain an overdetermined system. If the interior points do not all happen to fall on a nodal surface of an interior normal mode, then this method uniquely solves the Helmholtz integral equation for all wavenumbers.

In the original CHIEF paper [9], a linear least squares approach was proposed to solve the overdetermined system. This chapter adopts such an approach, in particular complex singular value decomposition, and describes its actual implementation and effectiveness. A Lagrange multiplier approach apparently has been used successfully for some time by A. F. Seybert, C. Y. R. Cheng, T. K. Rengarajan, F. J. Rizzo, D. J. Shippy, B. Soenarko, T. W. Wu, and X. F. Wu, although a precise description does not appear to have been published [10–18].

Alternatives to the CHIEF method include, but are not limited to, variations on the: Gradient Helmholtz Integral Equation or GHIE [19–24], Composite Outward Normal Derivative Overlap Relation or CONDOR [25–26], and Coupled Helmholtz Integrals or CHI [27]. A discussion of the CHIEF method versus its competitors is outside the scope of this dissertation. References [9–27] examine the various advantages and shortcomings of the several approaches. The paper by K. A. Cunefare, G. Koopmann and K. Brod [17] presents a recent comparison in some depth. More recently, comparisons between boundary element methods and finite element methods are the topics of the series of papers by I. Harari and T. J. R. Hughes [28, 29].

This chapter seeks to provide the reader with (a) a precise description of a practical implementation of a numerical boundary element method using CHIEF, and (b) both qualitative and quantitative guidelines as to the method's rates of convergence, element resolution requirements, and CHIEF point requirements, in order to obtain solutions to a desired accuracy. For reasons of clarity, the presentation deals with the two-dimensional Helmholtz equation, although most of the methods and results also apply for higher dimensions.

SURFACE HELMHOLTZ INTEGRAL FORMULATION

The use of the Helmholtz integrals to develop boundary element methods are fairly widely published. An accessible exposition is that by C. A. Brebbia and S. Walker [30]. A formal mathematical treatment of the derivation of the boundary integral equations can be found in the review article by R. E. Kleinman and G. F. Roach [31].

Referring to Figure 1, the Helmholtz integral equation for a point i anywhere in the space $E \cup \Gamma \cup I$ applied to an arbitrary body with interior I, exterior E, and bounded by a simply connected sufficiently smooth closed surface Γ is:

$$\int_\Gamma \left(u \frac{\partial G}{\partial n} - G \frac{\partial u}{\partial n} \right) d\Gamma = \begin{cases} u_i & i \in E \quad (2a) \\ \frac{1}{2} u_i & i \in \Gamma \quad (2b) \\ 0 & i \in I \quad (2c) \end{cases}$$

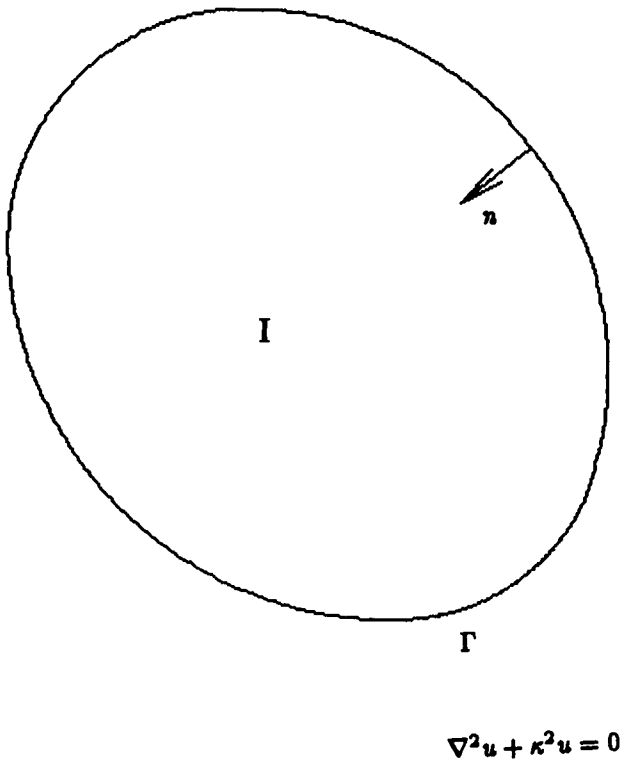

Figure 1: Nomenclature for the exterior Helmholtz problem.

where, n is the unit normal facing outward from the region of acoustic propagation, u is the acoustic potential, and G is the free space Green's function. The Green's function G is the fundamental solution of the Helmholtz equation with a point source inhomogeneity, i.e.

$$\nabla^2 G + \kappa^2 G = -\delta. \tag{3}$$

Considering the boundary Γ to be divided into M straight elements with the values of the potential u, and its normal derivative $\frac{\partial u}{\partial n}$, to be constant on each element, equation (2b) can be discretized to:

$$-\frac{1}{2}u_i + \sum_{j=1}^{M} u_j \, \bar{\int}_{\Gamma_j} \left(\frac{\partial G}{\partial n}\right)_{ij} d\Gamma = \sum_{j=1}^{M} \left(\frac{\partial u}{\partial n}\right)_j \int_{\Gamma_j} G_{ij} d\Gamma \tag{4}$$

for points i and j on the boundary elements Γ_j, where the bar through the integral sign denotes exclusion of the singular point. This can be expressed in matrix form as,

$$\mathbf{H}\bar{u} = \mathbf{G}\overline{\left(\frac{\partial u}{\partial n}\right)} \tag{5}$$

where the elements of the M by M matrix $\mathbf{H}$ are:

$$h_{ij} = \begin{cases} -\frac{1}{2} & i = j \\ \int_{\Gamma_j} \left(\frac{\partial G}{\partial n}\right)_{ij} d\Gamma & i \neq j \end{cases} \tag{6}$$

and the elements of the M by M matrix $\mathbf{G}$ are:

$$g_{ij} = \int_{\Gamma_j} G_{ij} d\Gamma, \tag{7}$$

with:

$$\bar{u} = (u_1, \ldots, u_M)^{\mathrm{T}} \tag{8}$$

$$\left(\overline{\frac{\partial u}{\partial n}}\right) = \left(\left(\frac{\partial u}{\partial n}\right)_1, \ldots, \left(\frac{\partial u}{\partial n}\right)_M\right)^{\mathrm{T}} \tag{9}$$

For a Dirichlet problem $\bar{u}$ is known and $\left(\overline{\frac{\partial u}{\partial n}}\right)$ is sought. A Neumann problem has the situation reversed, $\left(\overline{\frac{\partial u}{\partial n}}\right)$ is known and $\bar{u}$ is to be found.

Assuming that κ is a value for which a solution exists, once $\bar{u}$ and $\left(\overline{\frac{\partial u}{\partial n}}\right)$ on the boundary are known, the acoustic potentials can be found at exterior points by using equation (2a). For a point $i \in E$, the discretized version of equation (2a) is:

$$\sum_{j=1}^{M} u_j \int_{\Gamma_j} \left(\frac{\partial G}{\partial n}\right)_{ij} d\Gamma - \sum_{j=1}^{M} \left(\frac{\partial u}{\partial n}\right)_j \int_{\Gamma_j} G_{ij} d\Gamma = u_{i\,exterior} \tag{10}$$

In matrix form, for M boundary elements and N exterior points, equation (10) has the form:

$$\begin{array}{c} \\ \uparrow \\ N \\ \downarrow \end{array} \overset{\leftarrow M \rightarrow}{\begin{pmatrix} & & \\ & \int_{\Gamma_j} \left(\frac{\partial Q}{\partial n}\right)_{ij} d\Gamma & \\ & & \end{pmatrix}} \begin{pmatrix} u_1 \\ \vdots \\ u_M \end{pmatrix}_{boundary} - \overset{\leftarrow M \rightarrow}{\begin{pmatrix} & & \\ & \int_{\Gamma_j} G_{ij}\ d\Gamma & \\ & & \end{pmatrix}} \begin{pmatrix} \left(\frac{\partial u}{\partial n}\right)_1 \\ \vdots \\ \left(\frac{\partial u}{\partial n}\right)_M \end{pmatrix}_{boundary} = \begin{pmatrix} u_1 \\ \vdots \\ u_i \\ \vdots \\ u_N \end{pmatrix}_{exterior} \tag{11}$$

Note in equations (10) and (11), the points indexed by j are on the boundary and the points indexed by i are exterior, so the points are never the same and

no singularities occur in the integrands. Hence, the versions of the **H** and **G** matrices for external points are straightforward to compute. Once these are found, the entire left-hand side of equation (11) is known. The vector of exterior potentials, the right-hand side of equation (11), then can be calculated by a few simple matrix operations.

INTERIOR HELMHOLTZ INTEGRALS AND THE CHIEF FORMULATION

As discussed in the introduction, the system of equations (4), or alternatively (5), have non-unique solutions for values of the wavenumber κ at the eigenfrequencies of the corresponding interior problem. One way, although perhaps not necessarily the "best" way, to overcome this deficiency is to combine with the equations derived from the surface Helmholtz integral equation (2b) additional equations derived from the interior Helmholtz integral equation (2c), hence the name Combined Helmholtz Integral Equation Formulation or CHIEF.

Similar to the discretization of the surface Helmholtz integral equation, considering the boundary Γ to be divided into M elements with the values of the potential u and its normal derivative $\left(\frac{\partial u}{\partial n}\right)$, taken to be constant on each element, then for L interior points at locations denoted by subscript l, the interior Helmholtz equation (2c) yields:

$$\sum_{j=1}^{M} u_j \int_{\Gamma_j} \left(\frac{\partial G}{\partial n}\right)_{lj} d\Gamma = \sum_{j=1}^{M} \left(\frac{\partial u}{\partial n}\right)_j \int_{\Gamma_j} G_{lj} d\Gamma \tag{12}$$

Introducing,

$$\tilde{h}_{lj} = \int_{\Gamma_j} \left(\frac{\partial G}{\partial n}\right)_{lj} d\Gamma \tag{13}$$

and

$$\tilde{g}_{\ell j} = \int_{\Gamma_j} G_{\ell j} d\Gamma \tag{14}$$

the matrix equation for the boundary potentials $\bar{u}$ and the vector of its normal derivatives $\left(\overline{\frac{\partial u}{\partial n}}\right)$ becomes:

$$\begin{array}{c} \\ \uparrow \\ \\ M \\ + \\ L \\ \\ \downarrow \end{array} \begin{array}{c} \begin{array}{ccc} \leftarrow & M & \rightarrow \end{array} \\ \begin{pmatrix} h_{11} & \cdots & h_{1M} \\ \vdots & & \vdots \\ h_{M1} & \cdots & h_{MM} \\ \tilde{h}_{11} & \cdots & \tilde{h}_{1M} \\ \vdots & & \vdots \\ \tilde{h}_{L1} & \cdots & \tilde{h}_{LM} \end{pmatrix} \end{array} \begin{array}{c} \\ \begin{pmatrix} u_1 \\ \vdots \\ u_M \end{pmatrix} \end{array} \begin{array}{c} \uparrow \\ M \\ \downarrow \end{array} = \begin{array}{c} \\ \uparrow \\ \\ M \\ + \\ L \\ \\ \downarrow \end{array} \begin{array}{c} \begin{array}{ccc} \leftarrow & M & \rightarrow \end{array} \\ \begin{pmatrix} g_{11} & \cdots & g_{1M} \\ \vdots & & \vdots \\ g_{M1} & \cdots & g_{MM} \\ \tilde{g}_{11} & \cdots & \tilde{g}_{1M} \\ \vdots & & \vdots \\ \tilde{g}_{L1} & \cdots & \tilde{g}_{LM} \end{pmatrix} \end{array} \begin{array}{c} \\ \begin{pmatrix} \left(\frac{\partial u}{\partial n}\right)_1 \\ \vdots \\ \left(\frac{\partial u}{\partial n}\right)_M \end{pmatrix} \end{array} \begin{array}{c} \uparrow \\ M \\ \downarrow \end{array} \tag{15}$$

where h_{ij}'s and g_{ij}'s are defined by equations (6) and (7), respectively.

Denoting the submatrix of the $\tilde{h}_{\ell j}$'s by $\tilde{H}$, the submatrix of the $\tilde{g}_{\ell j}$'s by $\tilde{G}$, and the vectors $\bar{u}$ and $\left(\overline{\frac{\partial u}{\partial n}}\right)$ as defined by equations (8) and (9) respectively, then the CHIEF system (15) can be written concisely as:

$$\begin{pmatrix} H \\ - - \\ \tilde{H} \end{pmatrix} \bar{u} = \begin{pmatrix} G \\ - - \\ \tilde{G} \end{pmatrix} \left(\overline{\frac{\partial u}{\partial n}}\right) \tag{16}$$

Here, as in equations (5) and (11), the matrices are continuous functions of the wavenumber κ. If at least one of the L CHIEF points does not lie on or nearly on a nodal line or surface of an eigenmode corresponding to the particular value of κ, then the system of equations (16) is non-singular. If more than one CHIEF

point is off a nodal surface for an interior resonant κ, or if there is no interior resonance at the particular value of κ, then the system (16) is overdetermined.

ROBIN BOUNDARY CONDITIONS

Frequently in acoustic and vibration problems, the boundary conditions are neither Dirichlet (u known, $\frac{\partial u}{\partial n}$ sought) or Neumann ($\frac{\partial u}{\partial n}$ known, u sought) , but mixed or Robin conditions. Robin boundary conditions can be written in the form:

$$u + \alpha \frac{\partial u}{\partial n} = 0. \tag{17}$$

When u represents the acoustic velocity potential, then

$$\alpha = -\frac{jz}{2\pi f \rho} \tag{18}$$

where $j = \sqrt{-1}$, z is the acoustic impedance, f is the frequency, and ρ is the density.

In the discretized boundary element formulations developed thus far, if the normal derivatives for the first R elements, $\left(\frac{\partial u}{\partial n}\right), \ldots, \left(\frac{\partial u}{\partial n}\right)_R$ are taken to be given (e.g. specified element velocities), and the $M - R$ remaining boundary elements are taken to have constant α's, indexed $\alpha_{R+1}, \ldots, \alpha_M$, as given, (e.g. specified element impedances) then:

$$\left(\frac{\partial u}{\partial n}\right) = \left(\left(\frac{\partial u}{\partial n}\right)_1, \ldots, \left(\frac{\partial u}{\partial n}\right)_R, \frac{-u_{R+1}}{\alpha_{R+1}}, \ldots, \frac{-u_M}{\alpha_M}\right)^T \tag{19}$$

Substituting the right-hand side of equation (19) into equation (5) and manipulating via elementary although tedious matrix operations, the matrix equation

in terms of the unknown vector of potentials $\bar{u}$, for only the surface Helmholtz integral formulation can be expressed as:

$$\left(\begin{array}{ccc|ccc} h_{11} & \cdots & h_{1R} & \left(h_{1\,R+1}+\frac{g_{1\,R+1}}{\alpha_{R+1}}\right) & \cdots & \left(h_{1\,M}+\frac{g_{1\,M}}{\alpha_M}\right) \\ \vdots & \vdots & \vdots & \vdots & \vdots & \vdots \\ h_{M1} & \cdots & h_{MR} & \left(h_{M\,R+1}+\frac{g_{M\,R+1}}{\alpha_{R+1}}\right) & \cdots & \left(h_{M\,M}+\frac{g_{M\,M}}{\alpha_M}\right) \end{array}\right)\left(\begin{array}{c} u_1 \\ \vdots \\ u_M \end{array}\right) = \left(\begin{array}{ccc} g_{11} & \cdots & g_{1R} \\ \vdots & \vdots & \vdots \\ g_{M1} & \cdots & g_{MR} \end{array}\right)\left(\begin{array}{c} \left(\frac{\partial \phi}{\partial n}\right)_1 \\ \vdots \\ \left(\frac{\partial \phi}{\partial n}\right)_R \end{array}\right) \tag{20}$$

Likewise, the substitution of equation (19) into equations (15) or (16) results in an expression for the CHIEF method with Robin boundary conditions:

$$\left(\begin{array}{ccc|ccc} h_{11} & \cdots & h_{1\,R} & \left(h_{1\,R+1}+\frac{g_{1\,R+1}}{\alpha_{R+1}}\right) & \cdots & \left(h_{1\,M}+\frac{g_{1\,M}}{\alpha_M}\right) \\ \vdots & \vdots & \vdots & \vdots & \vdots & \vdots \\ h_{M1} & \cdots & h_{M\,R} & \left(h_{M\,R+1}+\frac{g_{M\,R+1}}{\alpha_{R+1}}\right) & \cdots & \left(h_{M\,M}+\frac{g_{M\,M}}{\alpha_M}\right) \\ \tilde{h}_{11} & \cdots & \tilde{h}_{1\,R} & \left(\tilde{h}_{1\,R+1}+\frac{\tilde{g}_{1\,R+1}}{\alpha_{R+1}}\right) & \cdots & \left(\tilde{h}_{1\,M}+\frac{\tilde{g}_{1\,M}}{\alpha_M}\right) \\ \vdots & \vdots & \vdots & \vdots & \vdots & \vdots \\ \tilde{h}_{L1} & \cdots & \tilde{h}_{L\,R} & \left(\tilde{h}_{L\,R+1}+\frac{\tilde{g}_{L\,R+1}}{\alpha_{R+1}}\right) & \cdots & \left(\tilde{h}_{L\,M}+\frac{\tilde{g}_{L\,M}}{\alpha_M}\right) \end{array}\right)\left(\begin{array}{c} u_1 \\ \vdots \\ u_M \end{array}\right) = \left(\begin{array}{ccc} g_{11} & \cdots & g_{1R} \\ \vdots & \vdots & \vdots \\ g_{M1} & \cdots & g_{MR} \\ \tilde{g}_{11} & \cdots & \tilde{g}_{1R} \\ \vdots & \vdots & \vdots \\ \tilde{g}_{L1} & \cdots & \tilde{g}_{LR} \end{array}\right)\left(\begin{array}{c} \left(\frac{\partial \phi}{\partial n}\right)_1 \\ \vdots \\ \left(\frac{\partial \phi}{\partial n}\right)_R \end{array}\right) \tag{21}$$

INTEGRANDS FOR THE TWO-DIMENSIONAL PROBLEM

The boundary element formulation presented thus far has been completely general in terms of the dimensionality of the problem. For the three-dimensional Helmholtz problem, the elements Γ_j are surfaces and the appropriate 3-D Green's function and normal derivative would be integrated over the surface elements

Γ_j to arrive at the matrix elements h_{ij}, $\tilde{h}_{ij}$, g_{ij}, and $\tilde{g}_{ij}$. An n-dimensional problem uses n-dimensional Green's functions and normal derivatives thereof, the elements Γ_j are then n-1 dimensional hypersurfaces, and the integrations are performed over these hypersurfaces. In the interests of clarity and computational simplicity, this chapter examines particular properties of two-dimensional examples of CHIEF and HIEF (surface Helmholtz integral formulation only) boundary element method implementations.

The properties of the fundamental solutions of the Helmholtz equation in various dimensions have been discussed throughout the literature. An introductory presentation can be found in the text by A. P. Dowling and J. E. Ffowcs Williams [32]. The treatise by G. Barton [33] examines this topic in some depth.

The Green's function of the two-dimensional Helmholtz equation for outgoing waves is:

$$G = \frac{-j}{4} H_0^{(2)}(\kappa r) \tag{22}$$

where $H_0^{(2)}$ is the Hankel function of the second kind of zero order, and r is the distance between the "source" and "receiver" points. Referring to the geometry and notation of Figure 2, denoting the source and receiver points by the subscripts i and j respectively, the Green's function (22) can be expressed as:

$$G_{ij} = \frac{-j}{4} H_0^{(2)}(\kappa r_{ij}). \tag{23}$$

The matrix elements to be evaluated also require the normal derivative of the Green's function. For the two-dimensional Helmholtz equation it is:

$$\frac{\partial G}{\partial n} = \frac{j\kappa}{4} H_1^{(2)}(\kappa r) \frac{\partial r}{\partial n} \tag{24}$$

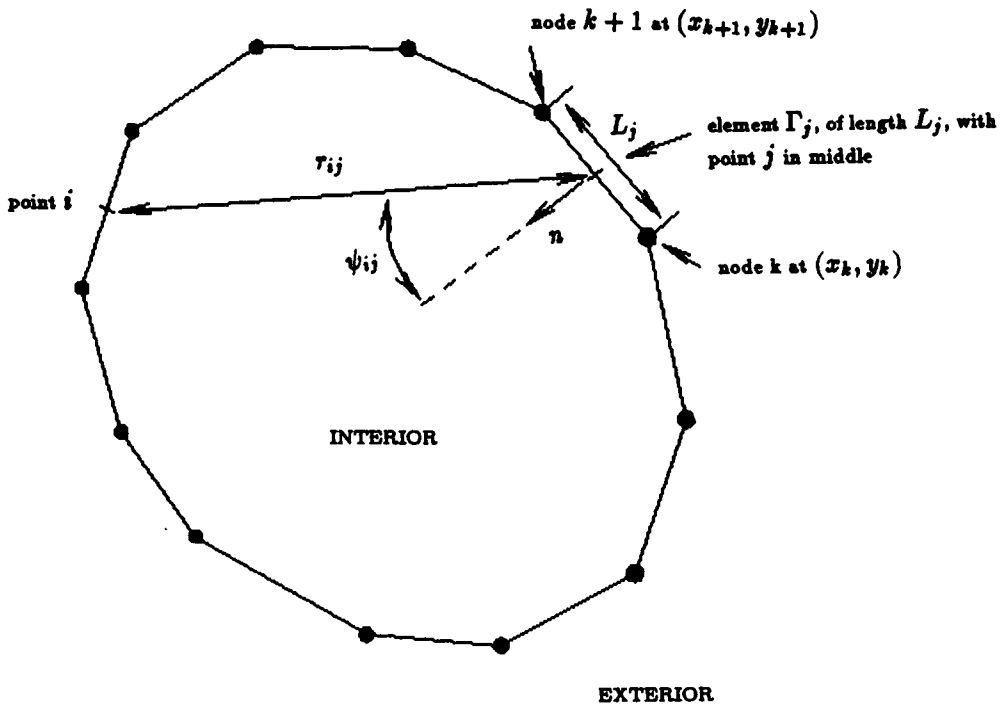

Figure 2: Nomenclature for the two-dimensional boundary element method

Thus,

$$\left(\frac{\partial G}{\partial n}\right)_{ij} = \frac{j\kappa}{4} H_1^{(2)}(\kappa r_{ij}) \left(\frac{\partial r}{\partial n}\right)_{ij} \tag{25}$$

Using the definition of the normal derivative

$$\left(\frac{\partial r}{\partial n}\right)_{ij} = \left(\frac{\partial r}{\partial x}\right)_{ij} (cos\,\theta_j) + \left(\frac{\partial r}{\partial y}\right)_{ij} (sin\,\theta_j) \tag{26}$$

where

$$tan\,\theta_j = \frac{x_k - x_{k+1}}{y_{k+1} - y_k} \tag{27}$$

and defining β_{ij} by,

$$tan\,\beta_{ij} = \frac{y_j - y_i}{x_j - x_i} \tag{28}$$

then the angle, denoted by ψ_{ij}, between the radius vector r_{ij} from the point i to the point j and the normal n at the point j can be expressed,

$$\psi_{ij} = \beta_{ij} - \theta_j \tag{29}$$

From this it follows after some trigonometric manipulations that,

$$\left(\frac{\partial r}{\partial n}\right)_{ij} = cos\,\psi_{ij} \tag{30}$$

so,

$$\left(\frac{\partial G}{\partial n}\right)_{ij} = j\frac{\kappa}{4}\left\{H_1^{(2)}(kr_{ij})\right\} cos\,\psi_{ij} \tag{31}$$

A parametric representation of the element Γ_j is:

$$x(\xi) = x_k + \xi(x_{k+1} - x_k) \tag{32a}$$

$$y(\xi) = y_k + \xi(y_{k+1} - y_k) \tag{32b}$$

where ξ goes from 0 to 1. With this parameterization, if $d\Gamma$ is a differential length element of Γ_j, then

$$d\Gamma = L_j d\xi \tag{33}$$

where L_j is the length of the element Γ_j, or

$$L_j = \sqrt{(x_{k+1} - x_k)^2 + (y_{k+1} - y_k)^2} \tag{34}$$

Also, with the parametrization (32), r_{ij} can be written as:

$$r_{ij} = \sqrt{[x_i - x_k - \xi(x_{k+1} - x_k)]^2 + [y_i - y_k - \xi(y_{k+1} - y_k)]^2} \tag{35}$$

from which it follows that:

$$\left(\frac{\partial r(\xi)}{\partial n}\right)_{ij} = \frac{[x_k + \xi(x_{k+1} - x_k) - x_i][y_{k+1} - y_k] + [y_k + \xi(y_{k+1} - y_k) - y_i][x_k - x_{k+1}]}{L_j r_{ij}(\xi)} \tag{36}$$

The ingredients needed for the computational recipes for the integrals h_{ij}, $\tilde{h}_{ij}$, g_{ij}, and $\tilde{g}_{ij}$ are now all known. Substituting the expressions (31–36) into equation (6) yields the recipe for h_{ij} in terms of real and imaginary parts as real integrals:

$$\Re[h_{ij}] = \frac{\kappa}{4}\int_0^1 \left\{Y_1[\kappa r_{ij}(\xi)]\right\} \frac{[(x_k - x_i) + \xi(x_{k+1} - x_k)][y_{k+1} - y_k] + [(y_k - y_i) + \xi(y_{k+1} - y_k)][x_k - x_{k+1}]}{r_{ij}(\xi)} d\xi$$

$i \neq j$ (37a)

$$\Im[h_{ij}] = \frac{\kappa}{4}\int_0^1 \left\{J_1[\kappa r_{ij}(\xi)]\right\} \frac{[(x_k - x_i) + \xi(x_{k+1} - x_k)][y_{k+1} - y_k] + [(y_k - y_i) + \xi(y_{k+1} - y_k)][x_k - x_{k+1}]}{r_{ij}(\xi)} d\xi$$

$i \neq j$ (37b)

$$\Re[h_{jj}] = -\frac{1}{2}$$

$i = j$ (37c)

$$\Im[h_{jj}] = 0$$

$i = j$ (37d)

The substitution of equations (31–36) into the formula (13) for $\tilde{h}_{\ell j}$ produces expressions very similar to (37a) and (37b), except in this case i's are replaced by ℓ's . The computational forms for g_{ij} and $\tilde{g}_{\ell j}$ are readily found by using formulae (31–36) in equations (7) and (14) respectively. They are:

$$\Re[g_{ij}] = -\frac{L_j}{4}\int_0^1 Y_0[\kappa r_{ij}(\xi)]d\xi \tag{38a}$$

$$\Im[g_{ij}] = -\frac{L_j}{4}\int_0^1 J_0[\kappa r_{ij}(\xi)]d\xi \tag{38b}$$

and similarly,

$$\Re[\tilde{g}_{\ell j}] = -\frac{L_j}{4}\int_0^1 Y_0[\kappa r_{\ell j}(\xi)]d\xi \tag{38c}$$

$$\Im[\tilde{g}_{\ell j}] = -\frac{L_j}{4}\int_0^1 J_0[\kappa r_{\ell j}(\xi)]d\xi \tag{38d}$$

where $r_{\ell j}(\xi)$ is the parametrized distance from an interior point ℓ to element j.

IMPLEMENTATION SPECIFICS

The computer codes used to construct and solve the system (20) for the HIEF method and the system (21) for the CHIEF method were written in FORTRAN-77 using mostly single precision (4 byte real numbers or 6 decimal digits). Double precision variables were used for various accumulators and when differencing of close numbers could be expected to occur.

The Bessel functions in the integrands were computed using the algorithm published by W. H. Press, B. P. Flannery, S. A. Teukolsky, and W. T. Vetterling [34]. The integrands for h_{ij} and g_{ij}, equations (37a, b) and (38a, b)

respectively, were computed using globally adaptive quadrature algorithms with randomization and singularity weakening based upon those of the Q1DA series of routines described by D. Kahaner, C. Moler, and S. Nash [35]. Although such exotic quadrature schemes slow the computation, they allow good global and local error tracking, crucial to the research purposes of this code. By suitable restrictions on the CHIEF point locations, i.e. not allowing them "too close" to the boundary Γ, the integrals for $\tilde{h}_{\ell j}$ and $\tilde{g}_{\ell j}$ will not contain any singularities or near singularities in their integrands. Thus these integrals could be computed using the very much simpler Bode's rule [34]. The errors in the elements h_{ij}, g_{ij}, $\tilde{h}_{\ell j}$, and $\tilde{g}_{\ell j}$ were estimated to have been kept below 0.4%. Most elements and most cases had error estimates substantially smaller than this.

The upper part of the matrices of equation (21) for the CHIEF system uses the same h_{ij}'s and g_{ij}'s as in the HIEF system (20). The actual implementation calculated these for the HIEF system, stored them, and later read them in for use again in the CHIEF system, guaranteeing that they were identical in both systems.

The HIEF system (20) was solved for the vector of potentials $\bar{u}$, by finding the complex **LU** decomposition of the left-hand side matrix using Crout's algorithm with implicit pivoting, then forward substitution and backsolving to get an initial $\bar{u}$ vector. Iterative refinement was then applied twice to arrive at the final $\bar{u}$ vector. This technique is described in detail in reference [34] and many other works dealing with numerical linear algebra. This particular implementation is for complex matrices whereas reference [34] discusses real ones. Differences in handling complex matrices instead of real matrices are discussed in the text by G. W. Stewart [36].

The iterative refinements ensure the $\bar{u}$ is nearly an exact solution for the discrete system (20). It does not, of course, ensure that the discrete system (20) provides a good estimate of the actual potential. In fact, for values of the wavenumber κ close to an eigenfrequency of the corresponding interior problem, the system (20) yields a very poor approximation of the actual potential.

As previously discussed, the CHIEF system (21) is in general overdetermined, so a solution for the potential vector $\bar{u}$ can be found in the linear least squares sense. One good way of solving for $\bar{u}$ in equation (21), chosen for the implementation here, is complex singular value decomposition.

In particular, the left-hand side matrix of the discrete system (21) was decomposed into the product of an (M+L) x M column-orthogonal matrix **U**, an M× M diagonal matrix **S** of the so-called singular values, and the conjugate transpose of an M× M orthogonal matrix **V**. This operation was carried out using a slightly modified and updated version of LINPACK [37] routine CSVDC.

Denoting the elements of the diagonal matrix **S** by σ_j, the operation of conjugate transposition by H, and the vector that results from multiplying out the right-hand side of equation (21) by $\bar{b}$, then formally:

$$\bar{u} = \mathbf{V} \cdot \left[diag\left(1 \,/\, \sigma_j\right) \right] \cdot \left(\boldsymbol{U}^H \cdot \bar{b} \right) \tag{39}$$

For σ_j's smaller in absolute value than 0.01% of the largest, the value of its reciprocal, $1/\sigma_j$, was set to zero. This corresponds to discarding the combination of equations, if any, so corrupted by numerical errors that they cannot contribute greater accuracy to the solution. The CHIEF method potential vector $\bar{u}$ was then solved for using an implementation of equation (39). The art of singular value decomposition and its uses is presented in an introductory fashion in reference [34], and in greater depth in references [36] and [37].

TEST CASES AND EXACT SOLUTION

The systems of equations (20) and (21) may correspond physically to a typical acoustic circumstance where a portion of the surface of an electromechanical device is forced to move with a prescribed velocity while the remainder of the surface passively reflects and absorbs the incident sound waves, depending upon its surface impedance characteristics. For the purpose of computing test cases, it is convenient to choose the geometry and surface impedance corresponding to a symmetrically radiating body.

Exact two-dimensional axially symmetric solutions of the Helmholtz equation for the acoustic velocity potential and its normal derivative, on the boundary of a circle of unit radius, are:

$$u = \frac{-j}{4} H_0^{(2)}(\kappa) = -\frac{1}{4}\Big\{Y_0(\kappa) + jJ_0(\kappa)\Big\} \tag{40}$$

and

$$\frac{\partial u}{\partial n} = \frac{j\kappa}{4} H_1^{(2)}(\kappa) = \frac{\kappa}{4}\Big\{Y_1(\kappa) + jJ_1(\kappa)\Big\} \tag{41}$$

Thus, the quantity α of equation (17) can be expressed:

$$\alpha = \frac{-u}{(\frac{\partial u}{\partial n})} = \frac{1}{\kappa}\left\{\frac{Y_0(\kappa) + jJ_0(\kappa)}{Y_1(\kappa) + jJ_1(\kappa)}\right\} \tag{42}$$

Using these as the necessary input to both systems HIEF (20) and CHIEF (21), solutions were obtained and the errors compared over the frequency range $0.1 < \kappa < 6.0$ This was done initially for 64 boundary elements and five randomly positioned CHIEF points. The frequency range was selected to include two of the interior homogeneous Dirichlet problem eigenvalues ($\kappa = 2.40483$ and

5.52008), the first and second interior resonant frequencies, respectively, where the previously mentioned uniqueness problem is manifested as numerical errors within the neighborhoods of these points. Following this, the error behavior was numerically examined separately as a function of the number of boundary elements and the number of CHIEF points.

Since for these test cases, there is no variation of α, u, or $\frac{\partial u}{\partial n}$ along the surface, the error results are virtually uncontaminated by the constant element approximation employed in obtaining equation (4). This is desirable in that it serves to separate accuracy questions related to the order of the element approximation from those arising from the uniqueness problem which the CHIEF method was designed to overcome.

RESULTS AND DISCUSSION

The percent error obtained using the CHIEF and HIEF methods are presented in Figures 3–6. These results were computed using 64 boundary elements and five randomly selected CHIEF points interior to the circle. Well away from the interior eigenvalues (in this case the zeros of $J_0(\kappa)$), the two methods yield, as expected, virtually the same result. In the vicinity of the first eigenvalue, the HIEF method reflects the severity of the error problem originating from the non-uniqueness of the HIEF solution. The CHIEF method remains well behaved and usefully accurate with only five CHIEF points and 64 boundary elements. Similar, but even worse error behavior is shown for the HIEF method near the second eigenvalue. Here, even the CHIEF method exhibits unacceptably large errors in the vicinity of the second eigenvalue. However, this can be largely attributed to

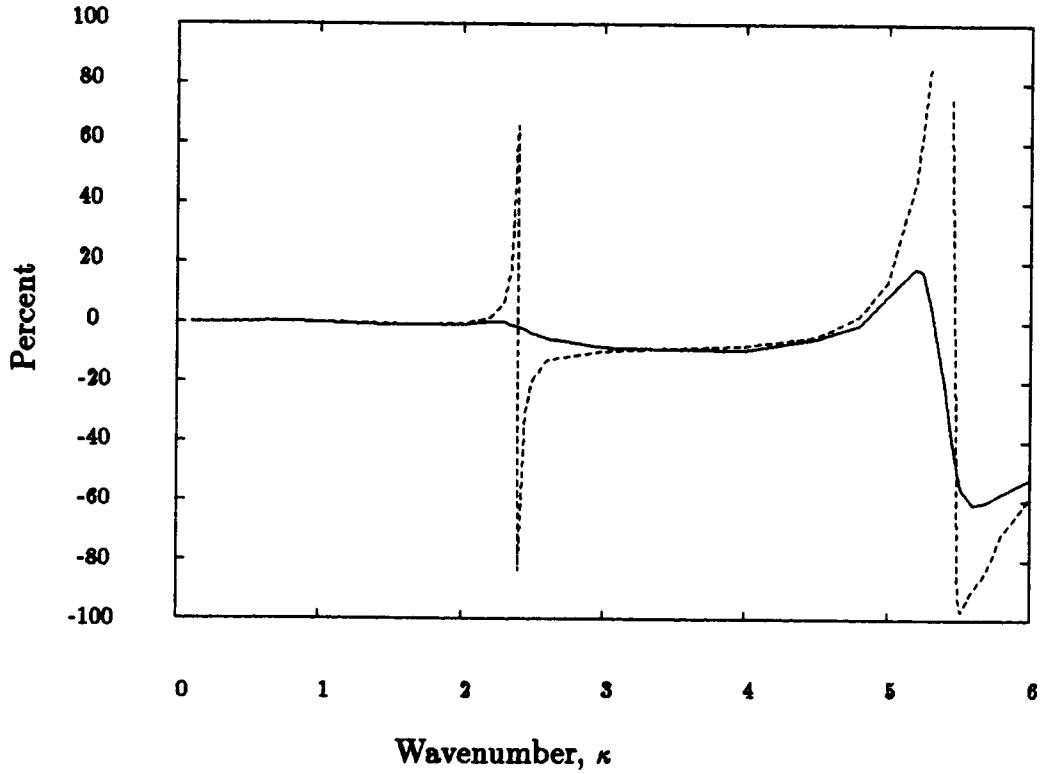

Figure 3: Maximum Percent Amplitude Errors.

Comparison of CHIEF and HIEF solutions.
64 Boundary Elements.

- - - HIEF; ——— CHIEF (5 points)

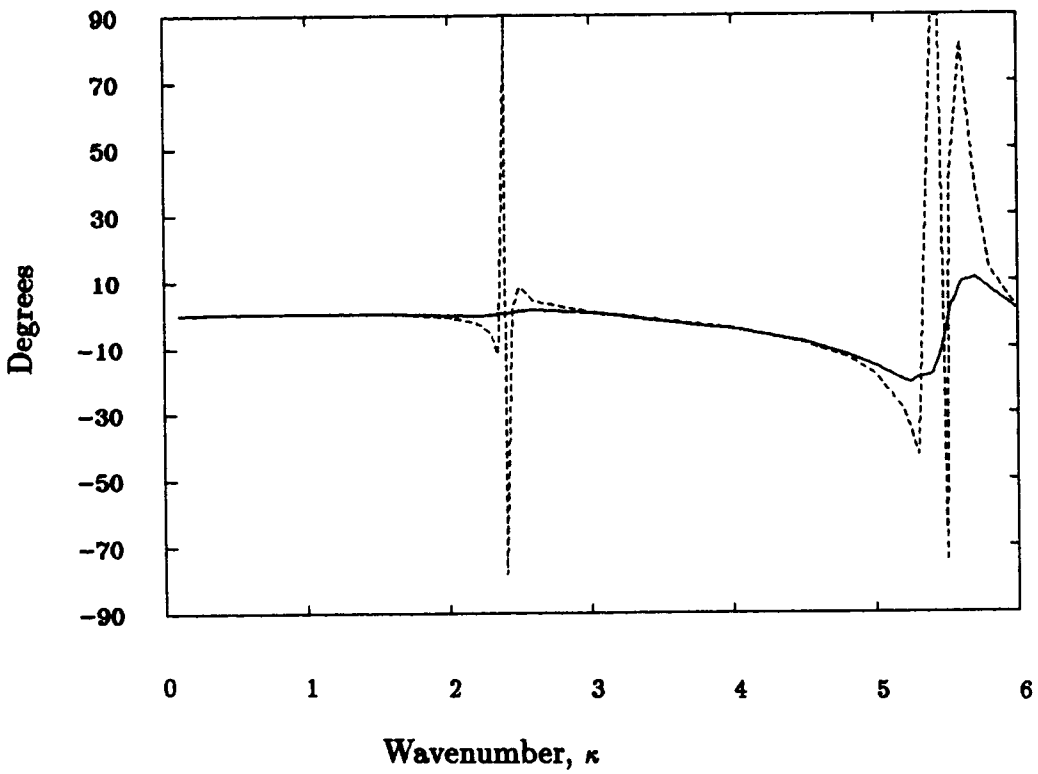

Figure 4: Maximum Phase Errors.

Comparison of CHIEF and HIEF solutions.
64 Boundary Elements.

- - - HIEF; ——— CHIEF (5 points)

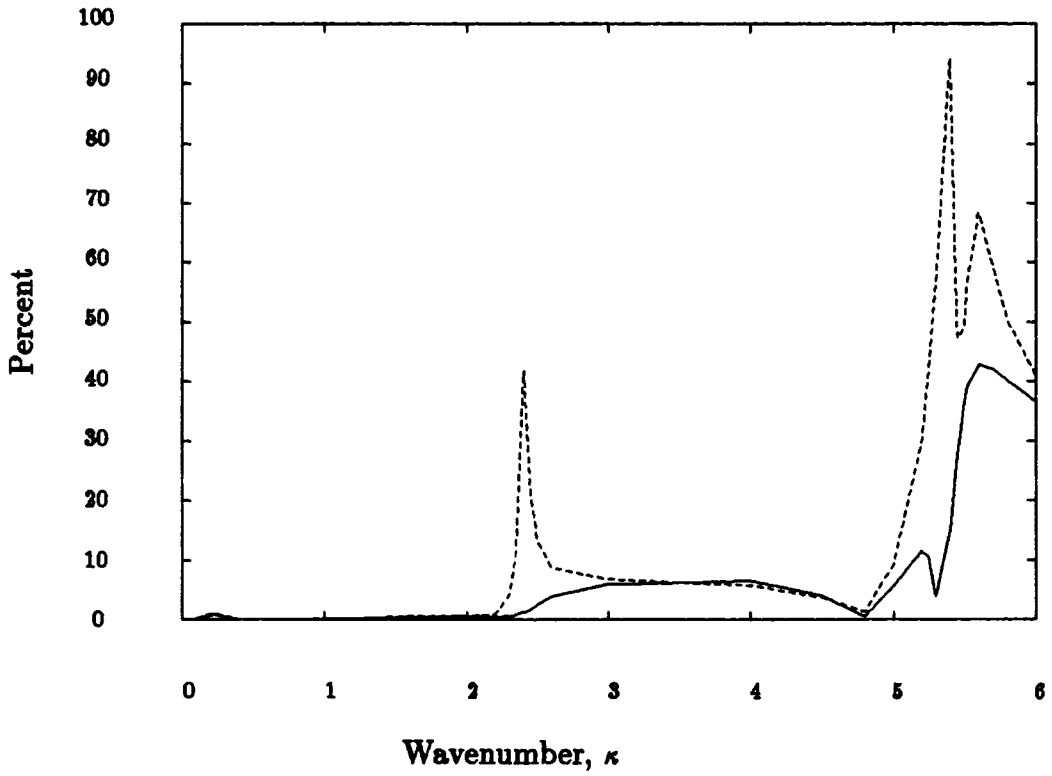

Figure 5: Root Mean Square (RMS) Percent Amplitude Errors.

Comparison of CHIEF and HIEF solutions.
64 Boundary Elements.

- - - HIEF; ——— CHIEF (5 points)

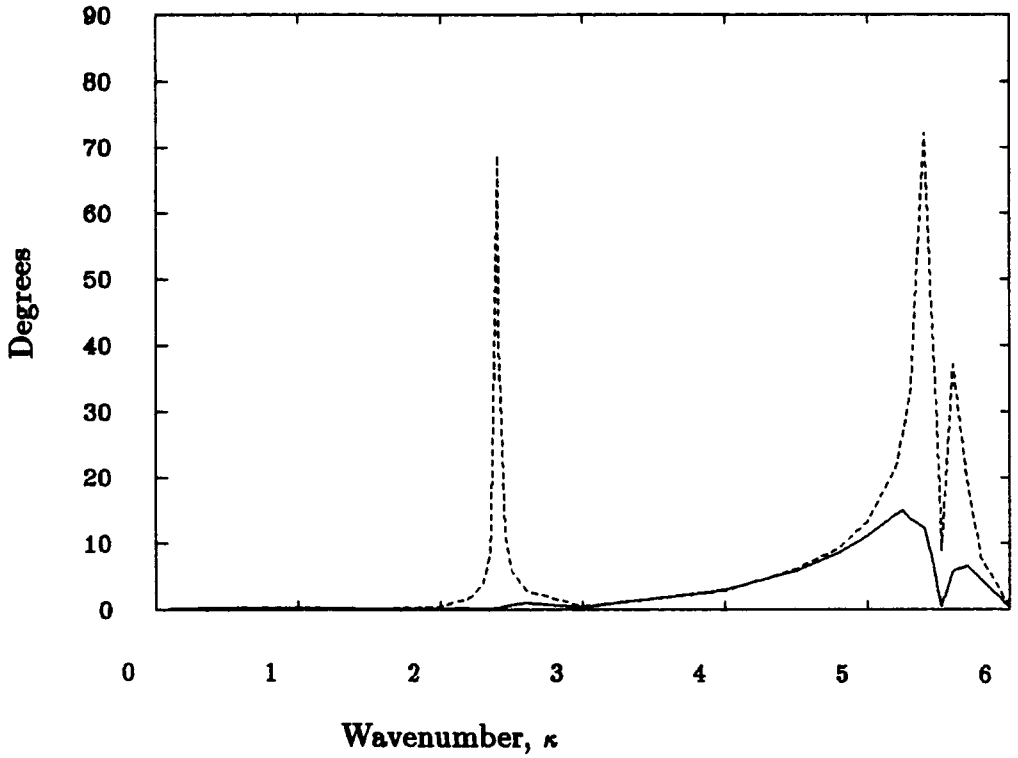

Figure 6: Root Mean Square (RMS) Percent Phase Errors.

Comparison of CHIEF and HIEF solutions.
64 Boundary Elements.

- - - HIEF; ——— CHIEF (5 points)

inadequate element resolution. Figures 7 and 8 show the error dependence on the element resolution at each eigenvalue. The rate of error reduction with increasing element resolution is seen to be very rapid. This rapid error reduction with increasing numbers of boundary elements seems to be a common trait of methods that use an overdetermined set of equations. This phenomenon certainly occurs using other codes, even in three dimensions [38, 39].

It is significant to note that substantial improvements in accuracy can be obtained even at low element resolution by increasing the number of CHIEF points. Figures 9 and 10 present the error dependence on the number of CHIEF points. It appears in both cases that there exists a frequency and element resolution dependent lower error limit which is approached asymptotically as the number of CHIEF points is increased.

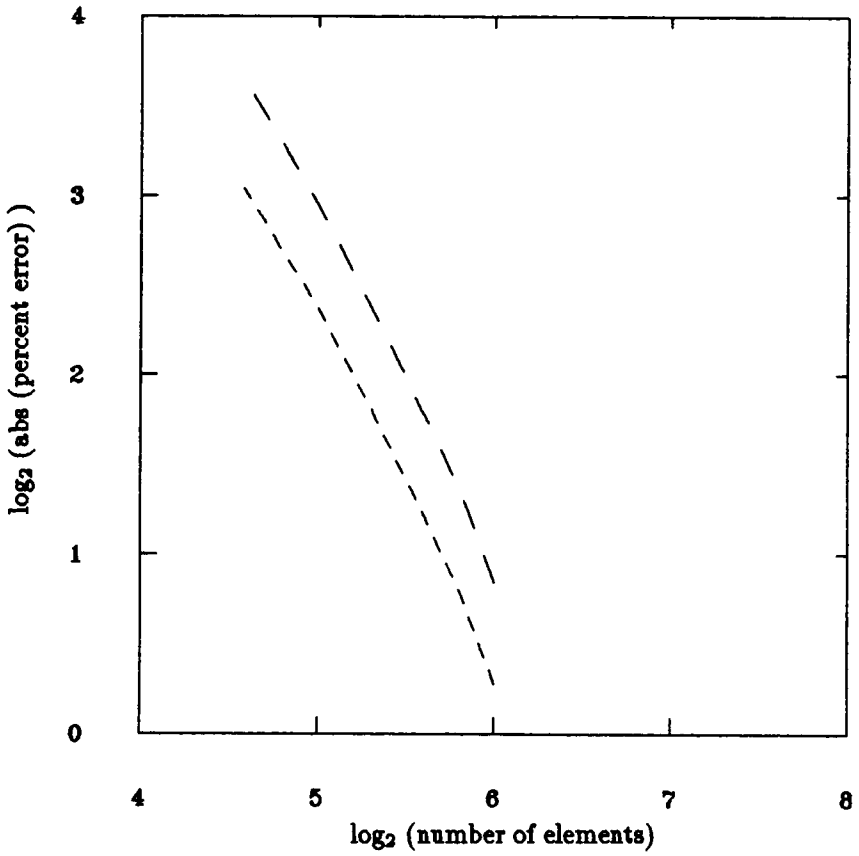

Figure 7: Amplitude Errors Versus Number of Elements, $\kappa = 2.40483$ (first interior resonance).

5 CHIEF points.

— — – Max; - - - RMS

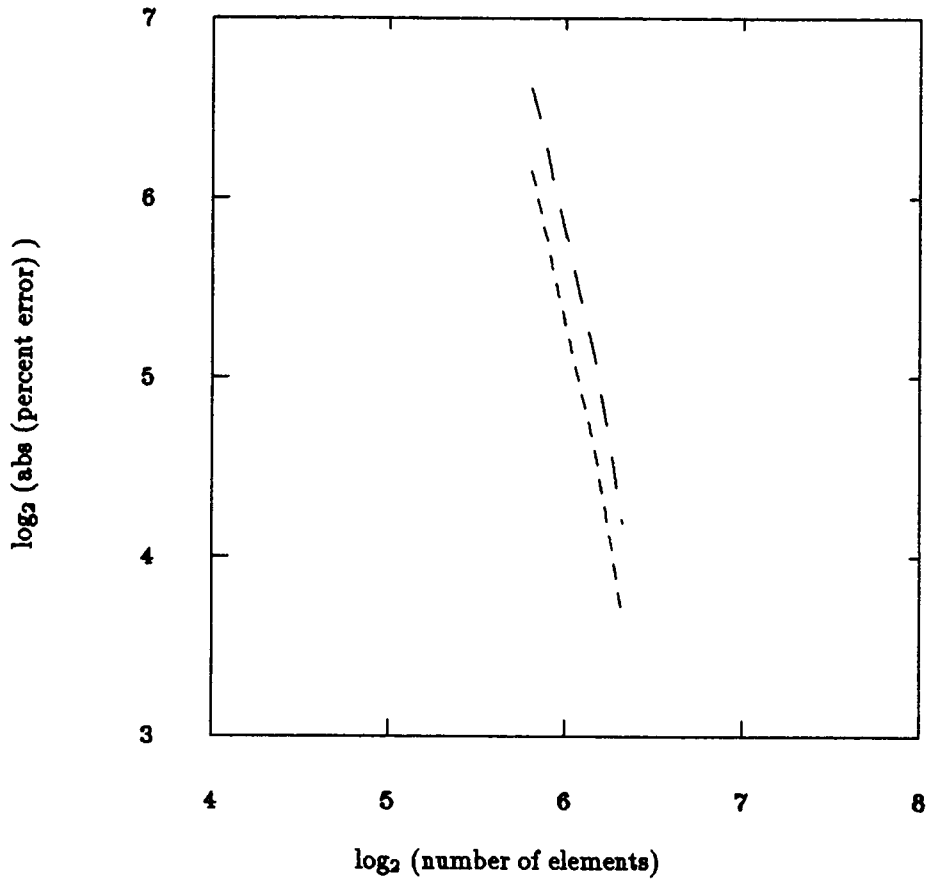

Figure 8: Amplitude Errors Versus Number of Elements, $\kappa = 5.52008$ (second interior resonance).

5 CHIEF points.

— — – Max; - - - RMS

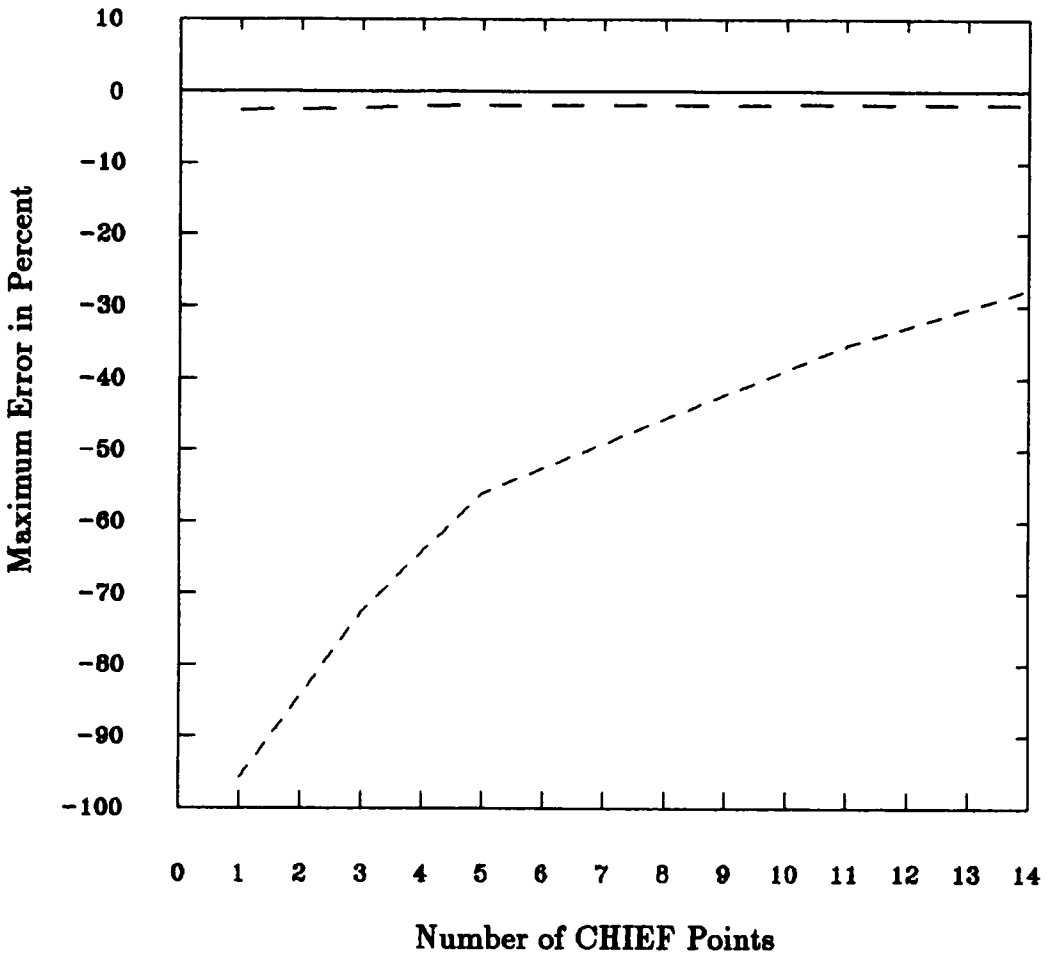

Figure 9: Maximum Amplitude Errors Versus Number of CHIEF Points.

64 Boundary Elements.

— — – $\kappa = 2.40483$; - - - $\kappa = 5.52008$

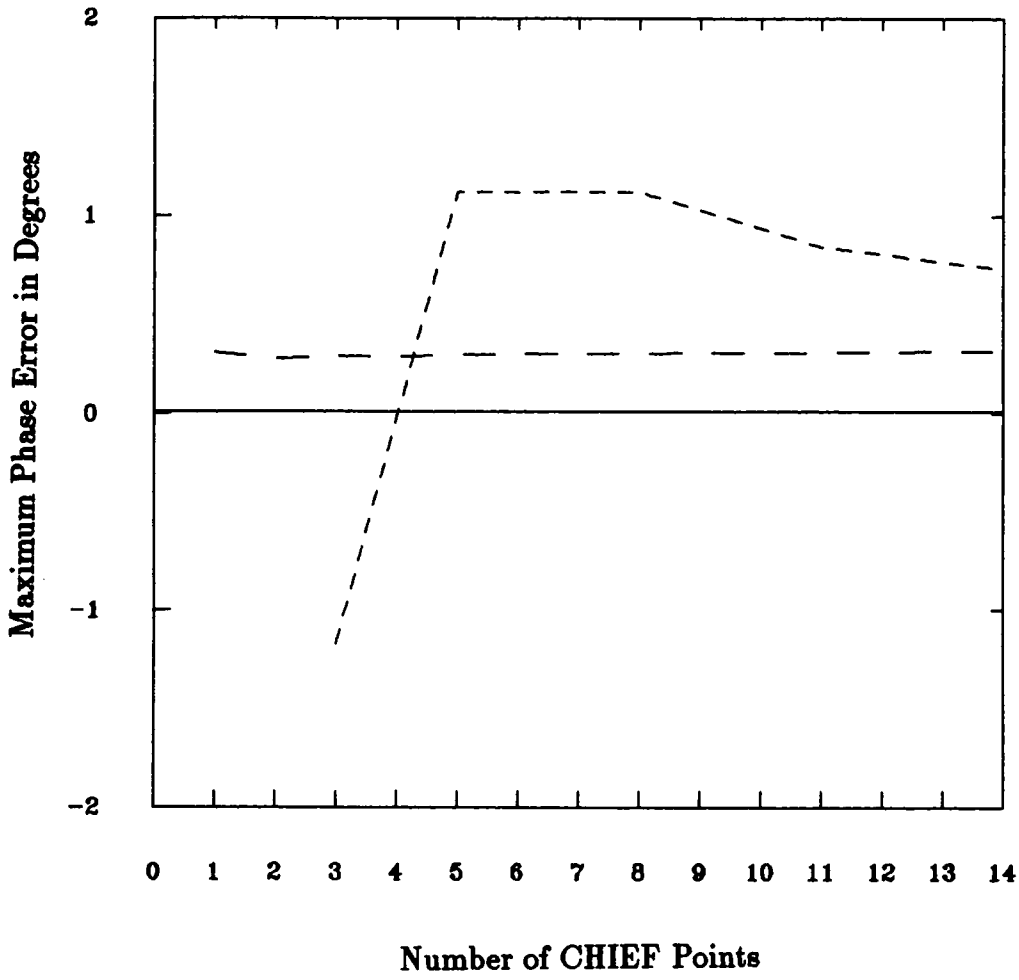

Figure 10: Maximum Phase Errors Versus Number of CHIEF Points.

64 Boundary Elements.

— — – $\kappa = 2.40483$; - - - $\kappa = 5.52008$

CHAPTER 2

GREEN'S FUNCTIONS FOR THE HELMHOLTZ EQUATION

GREEN'S FUNCTIONS

A *Green's function* is a solution of a (linear) partial differential equation and its associated initial or boundary conditions, in which a concentrated forcing function or "point source" is the nonhomogeneous term. It often represents a physical system's response to an excitation. Solutions for problems with other forcing functions are then found by superposition. The Green's function in partial differential equations is analogous to the "transfer function" in ordinary differential equations and linear systems theory.

The theory of Green's functions is well developed, at least for homogeneous media, and can be found in references [40-44] among many others. For initial value problems, a Green's function always exists, again analogous to transfer functions in electrical circuit theory. The analogy is weaker for boundary value problems. Unlike initial value problems, for boundary value problems, a Green's function may not exist. A boundary value problem may possibly have no solution, or the solution may not be unique. The treatise by G. Barton [33] as well as the books by I. Stakgold [44] and E. Zauderer [45] deal with these issues in some depth. These works also define the meaning of terms such as "point source" and "solution" more precisely. An even more general and abstract presentation of these concepts from the viewpoint of mathematical analysis is given by A. H. Zemanian [46, 47]. Zemanian's work considerably strengthens the ties between analysis applied to circuit theory and analysis applied to partial differential equations. It is these ties that the present chapter intends to exploit.

EXACT GREEN'S FUNCTIONS

Many methods have been developed to find exact analytical Green's functions for certain classes of initial value and boundary value problems. Several of these methods are described in various texts and treatises previously referenced [33], [40–44]. Some of these methods seem to be better suited to greater generalization or numerical implementation. Green's functions, or fundamental solutions found by "Transform Methods" in particular, appear amenable to fast numerical techniques and possibly greater generalization. The presentation by G. E. Latta [48] is suggestive of the power of the technique, although the details provided in the book by J. Arsac [49] were necessary to make it actually useful. Generalization and formalization of several aspects of integral transforms relevant to this technique are found in the treatise by Y. A. Brychkov and A. P. Prudnikov [50]. More accessible expositions, though less detailed, can be found in the well-known texts by R. N. Bracewell [51] and A. Papoulis [52].

Regardless of the method used to find it, the exact Green's function of the two-dimensional Helmholtz equation for outgoing waves is:

$$G = \frac{-j}{4} H_0^2(\kappa r) \tag{22}$$

where H_0^2 is the Hankel function of the second kind of zero order, and r is the distance between the "source" and "receiver" or "field" points. Equation (22) is often expressed in terms of Bessel functions [53–55] as:

$$G = -\frac{1}{4} Y_0(\kappa r) - j\frac{1}{4} J_0(\kappa r) \tag{43}$$

which makes clear the behavior of the real and imaginary parts. For illustration and later reference, Figures 11 and 12, respectively, depict the real and

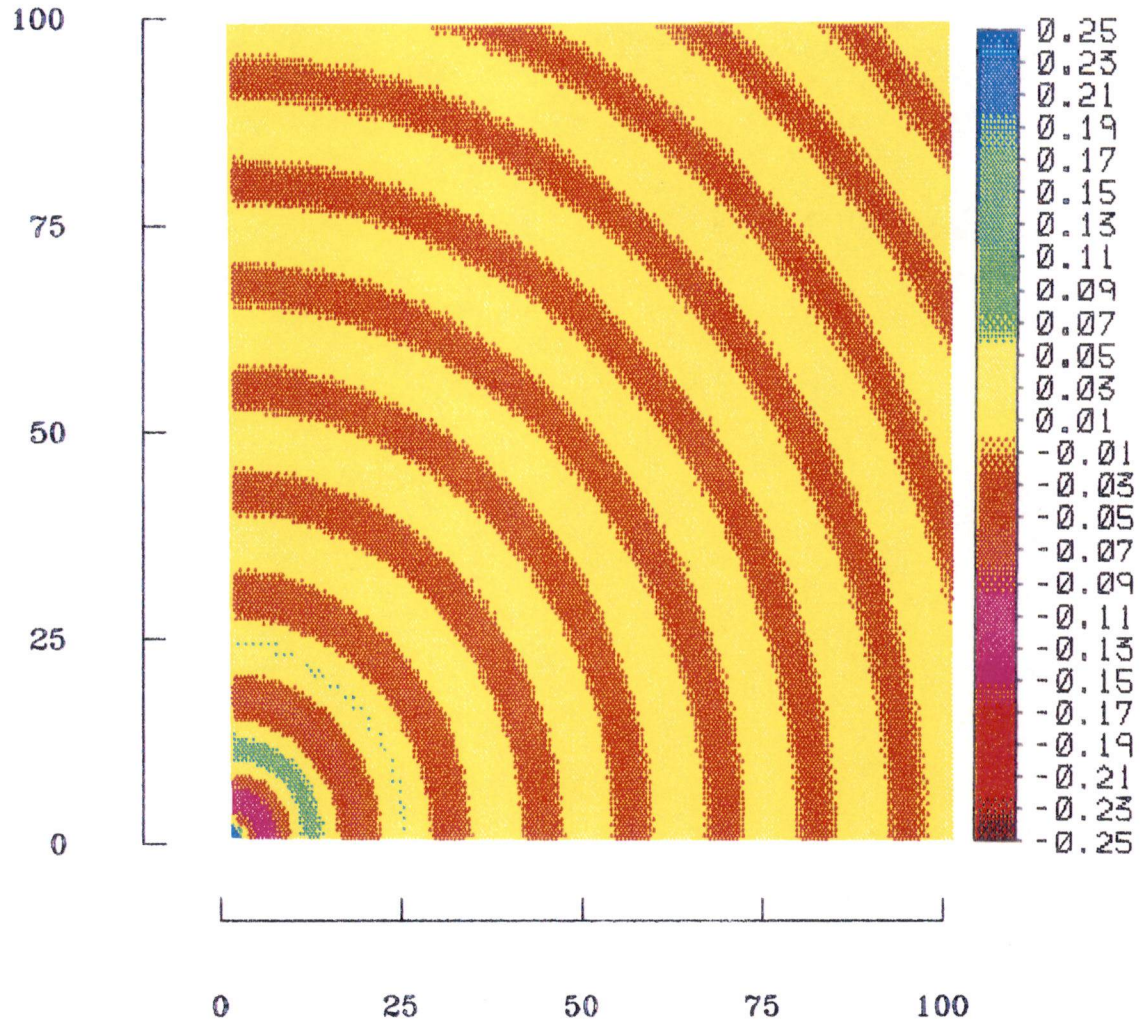

Figure 11: $\Re(G)$ exact values on a 128 x 128 grid, $\kappa = 0.5 - 0.0j$

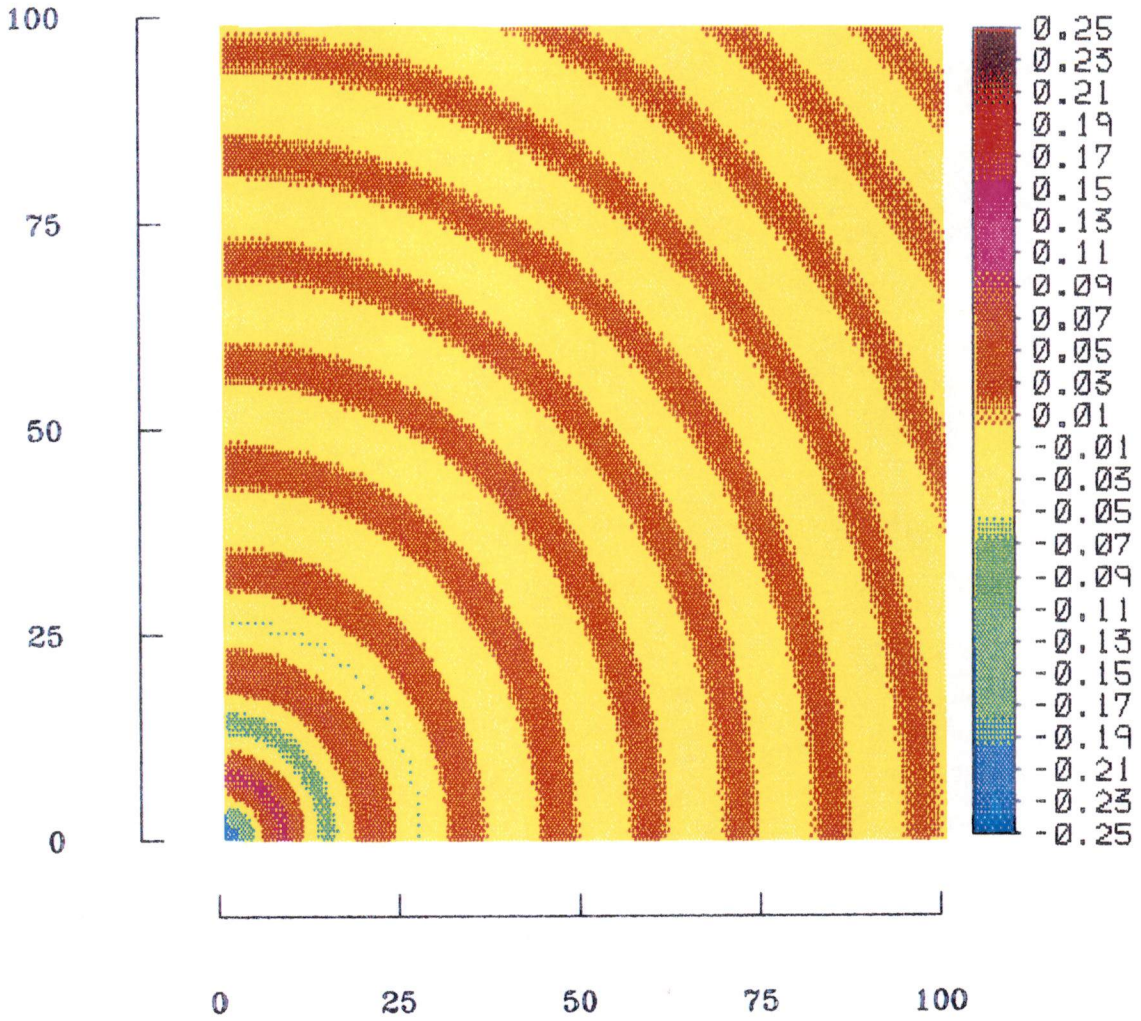

Figure 12: $\Im(G)$ exact values on a 128 x 128 grid, $\kappa = 0.5 - 0.0j$

imaginary parts of the Green's function for the two-dimensional, homogeneous media, Helmholtz equation with $\kappa = 0.5$ computed on the first quadrant of a 128 by 128 point grid. The quadrant shown has 64 by 64, or 4096 points. The circularly symmetric, decaying, wave-like behavior of both parts of the solution are apparent.

FOURIER TRANSFORM METHODS FOR GREEN'S FUNCTIONS

Following a formal approach [48] for seeking the Green's function of the two-dimensional Helmholtz equation for homogeneous media, the following procedure could be used. Start with the two-dimensional Helmholtz equation with a point source at the origin, i.e. the defining relation for the Green's function:

$$\nabla^2 G(x,z) + \kappa^2 G(x,z) = -\delta(x,z) \tag{44}$$

where x and z are the two spatial coordinates. Then perform the two-dimensional Fourier transformation [51, 52, 56–58] on both sides of (44) to get:

$$\mathfrak{F}\{\nabla^2 G(x,z) + \kappa^2 G(x,z)\} = \mathfrak{F}\{-\delta(x,z)\} \tag{45}$$

Denoting the two-dimensional Fourier transform of G by g, that is:

$$\mathfrak{F}\{G(x,z)\} = g(\Omega_x, \Omega_z) \tag{46}$$

and using properties of the Fourier transform, as found in references [51,52] among several others, equation (45) becomes:

$$[(-j\Omega_x)^2 + (-j\Omega_z)^2]g(\Omega_x, \Omega_z) + \kappa^2 g(\Omega_x, \Omega_z) = -1 \tag{47}$$

or simplifying:

$$[-(\Omega_x^2 + \Omega_z^2) + \kappa^2]g(\Omega_x, \Omega_z) = -1 \tag{48}$$

Formally then, one could write:

$$g(\Omega_x, \Omega_z) = \frac{1}{\kappa^2 - (\Omega_x^2 + \Omega_z^2)} \tag{49}$$

to create an expression for the Green's function:

$$G(x, z) = \mathfrak{F}^{-1}\{g(\Omega_x, \Omega_z)\} = \mathfrak{F}^{-1}\left\{\frac{-1}{\kappa^2 - (\Omega_x^2 + \Omega_z^2)}\right\} \tag{50}$$

This suggests a numerical approximation to $G(x, z)$ can be found by computing, on a discrete grid of (Ω_x, Ω_z) coordinates, $g(\Omega_x, \Omega_z)$, followed by taking its inverse discrete Fourier transform. This approach, as it stands, is both simple and wrong!

The astute reader will have noticed two things a bit questionable in the foregoing derivation. First, in going from equation (48) to (49), the division by $\kappa^2 - (\Omega_x^2 + \Omega_z^2)$ in equation (49) is not valid if the denominator goes to zero. Second, nowhere in the derivation, from the defining equation (44) to the final result (50), have any boundary conditions been used, such as radiation conditions. Therefore, equation (50) cannot represent (by itself) incoming or outgoing wave

solutions. If one does compute an approximation to equation (50) for purely real κ, Ω_x, and Ω_z, one gets an approximation to $-\frac{1}{4}Y_0(\kappa\sqrt{x^2+z^2})$, a part of a standing wave solution only. This is in agreement with tables and results in references [48] and [51].

Addressing the division operation going from equation (48) to (49) in terms of the branch of functional analysis known as the theory of distributions [44,46, 49,59,60] can help clarify the problem. For distributions of point support at the points where the denominator of equation (49) is zero, g is arbitrary and can be modified by a Dirac distribution of arbitrary strength at these points. This is a specific case of the more general theorem that if a denominator function, call it $f(\bar{\Omega})$, has a zero of order p at the point $\bar{q}$, then $g(\bar{q})$ which is the distributional solution of:

$$f(\bar{\Omega})g(\bar{\Omega}) = 1 \tag{51}$$

depends on p arbitrary constants such that:

$$g(\bar{\Omega}) = \frac{1}{f(\bar{\Omega})} + \Upsilon_1\delta(\bar{\Omega}-\bar{q}) + \Upsilon_2\delta'(\bar{\Omega}-\bar{q}) + \cdots + \Upsilon_p\delta^{(p-1)}(\bar{\Omega}-\bar{q}) \tag{52}$$

where $1/f(\bar{\Omega})$ is the multiplicative inverse of $f(\bar{\Omega})$ uniquely defined almost everywhere.

Thus in the particular case of interest, expressing $g(\Omega_x, \Omega_z)$ from equation (48) results in the relation:

$$g(\Omega_x, \Omega_z) = \frac{1}{\kappa^2 - (\Omega_x^2 + \Omega_z^2)} + \Upsilon\delta[\kappa^2 - (\Omega_x^2 + \Omega_z^2)] \tag{53}$$

instead of equation (49). The expression for the Green's function then becomes:

$$G(x,z) = \mathfrak{F}^{-1}\left\{\frac{1}{\kappa^2 - (\Omega_x^2 + \Omega_z^2)}\right\} + \Upsilon\mathfrak{F}^{-1}\left\{\delta[\kappa^2 - (\Omega_x^2 + \Omega_z^2)]\right\} \tag{54}$$

where the (complex) constant Υ is determined by other conditions.

Fourier transforms and inverse Fourier transforms of generalized functions are discussed in depth in the book by B. Davies [57]. After a derivation of some length, Davies shows how the application of boundary conditions corresponds to a choice of complex integration contour in performing the transform operation or its inverse. He also states the difficulty in finding the inverse transform arises in considering κ to be a real quantity. This requires a choice of an inversion contour which goes off the real axis. A detailed discussion of radiation conditions and a proof that replacing κ by $\kappa + j\varepsilon$ avoids such problems, is further presented in Davies' book. References [49,61,62] allude to the connection between the choice of contours in inverse Fourier transformation and boundary conditions on the partial differential equation; however, the useful details are largely absent.

Considering the quantity κ to be complex such that:

$$\kappa = \kappa_R + j\kappa_I \tag{55}$$

and the transform-space coordinates Ω_x and Ω_z to be purely real, then the term $[-(\Omega_x^2 + \Omega_z^2) + \kappa^2]$ in equation (48) can never be zero if $\kappa_I \neq 0$. Thus, for $\kappa_I \neq 0$, equation (49) is valid everywhere in Ω_x, Ω_z space and equation (50):

$$G(x,z) = \mathfrak{F}^{-1}\left\{\frac{-1}{\kappa^2 - (\Omega_x^2 + \Omega_z^2)}\right\} \tag{50}$$

does provide a formula for the Green's function. Taking κ_I to be a small positive (real) number results in the Green's function obeying incoming wave boundary conditions or

$$G_{\kappa_I>0} = \frac{j}{4} H_0^{(1)}(\kappa\sqrt{x^2+z^2}) \tag{56}$$

Conversely, $\kappa_I < 0$ results in the outgoing wave solution of present interest:

$$G_{\kappa_I<0} = \frac{-j}{4} H_0^{(2)}(\kappa\sqrt{x^2+z^2}) \tag{57}$$

GREEN'S FUNCTIONS BY NUMERICAL TRANSFORMS

Letting $\kappa = \kappa_R + j\kappa_I$ with $\kappa_R, \kappa_I \in \mathbf{R}$ and $\kappa_I < 0$, then equation (50) can be approximated by using numerical inverse Fourier transforms. The values of $g(\Omega_x, \Omega_z)$ can be computed on a vast variety of two-dimensional grids in Ω_x, Ω_z space. Suitable inverse Fourier transform algorithms exist for almost arbitrary grids. Fast transform algorithms generally require the grid to be periodic. Square, rectangular, hexagonal, and other periodic gridding schemes for use with fast transforms are discussed at length in the book by D. E. Dudgeon and R. M. Mersereau [63].

The present work shall only use the simplest case, a square grid where the spacing in "spatial frequency" $\Delta\Omega$ is constant. Further, the sampling increment $\Delta\Omega$ in Ω_x, Ω_z space will have been chosen so that for $\kappa = 1$, a sinusoid of wavelength:

$$\lambda = \frac{2\pi}{\kappa} \tag{58}$$

in x, z space will have been sampled twice. In other words, $\kappa = 1$ corresponds to sampling in x, z space at the Nyquist frequency. How to suitably sample

continuous functions for discrete transform operations is well-known, although often confusing in its details even to experienced practitioners. The texts by A. Papoulis [52] and F. G. Stremler [64] have especially clear presentations of the connections between continuous spaces and transforms, and discrete spaces and transforms.

For uniformly sampled functions, fast Fourier transform (FFT) and inverse fast Fourier transform (IFFT) algorithms can be readily implemented. For the one-dimensional case, these algorithms have been described in great detail in references [65–67]. Extensions to higher dimensions have also been widely published. Good presentations may be found in references [34,35,63,68,69], among others. Although highly developed [70], FFT and IFFT methods are not the only ways of calculating numerical Fourier transforms and their inverses [71], nor are they the only ways of obtaining a spectral estimate [34,72–75].

Computing $g(\Omega_x, \Omega_z)$ on a 64 by 64 point square grid for $\kappa = 0.5 - 0.03j$ and arranging the results in "wrap around order" yields Figures 13 and 14 for the real and imaginary parts, respectively. Wrap around ordering of input and output to FFT and IFFT routines is required when using FFTs. An explanation appears in reference [34]. Figure 15 illustrates the concept schematically. Ideally there should be no discontinuities across these boundaries or errors will appear in the forward or inverse transforms. This can become an involved topic and the reader is referred to references [34,63–68,76,77] for more detailed explanations. Examining equation (49) for $g(\Omega_x, \Omega_z)$, it is clear that if $\Delta\Omega$ is held constant, then for increasing grid sizes, the wrap boundaries move further away from the origin in Ω_x, Ω_z space, and that $g(\Omega_x, \Omega_z)$ vanishes at these boundaries.

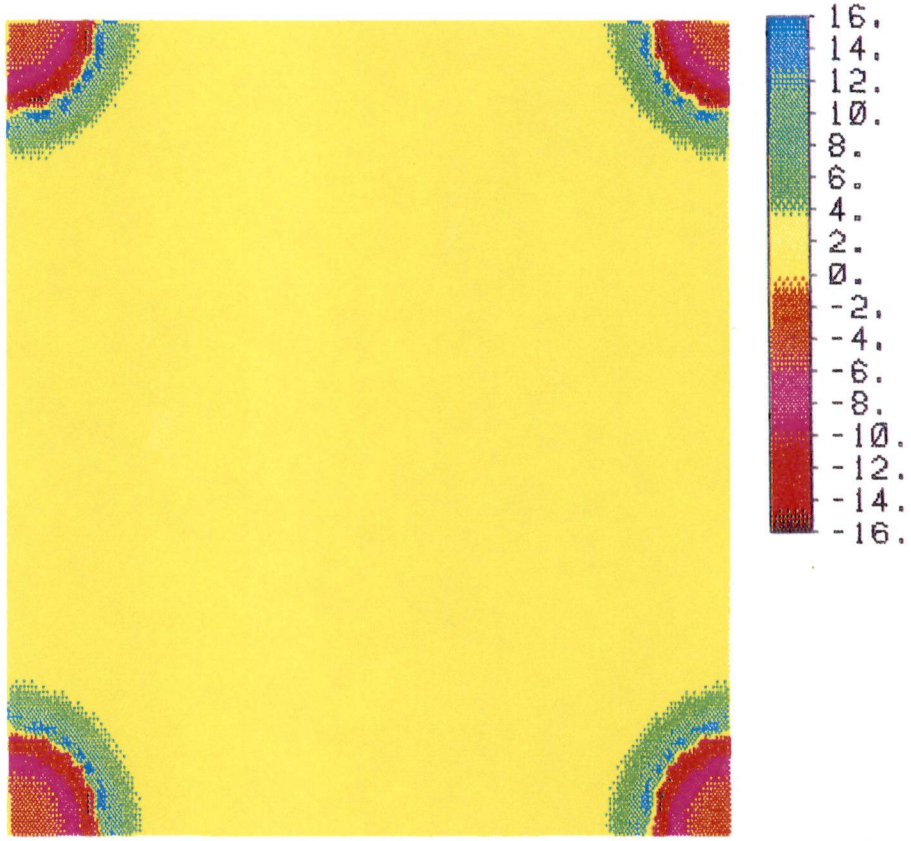

Figure 13: $\Re(\mathcal{F}\{G\})$ computed on a 64 x 64 grid, $\kappa = 0.5 - 0.03j$

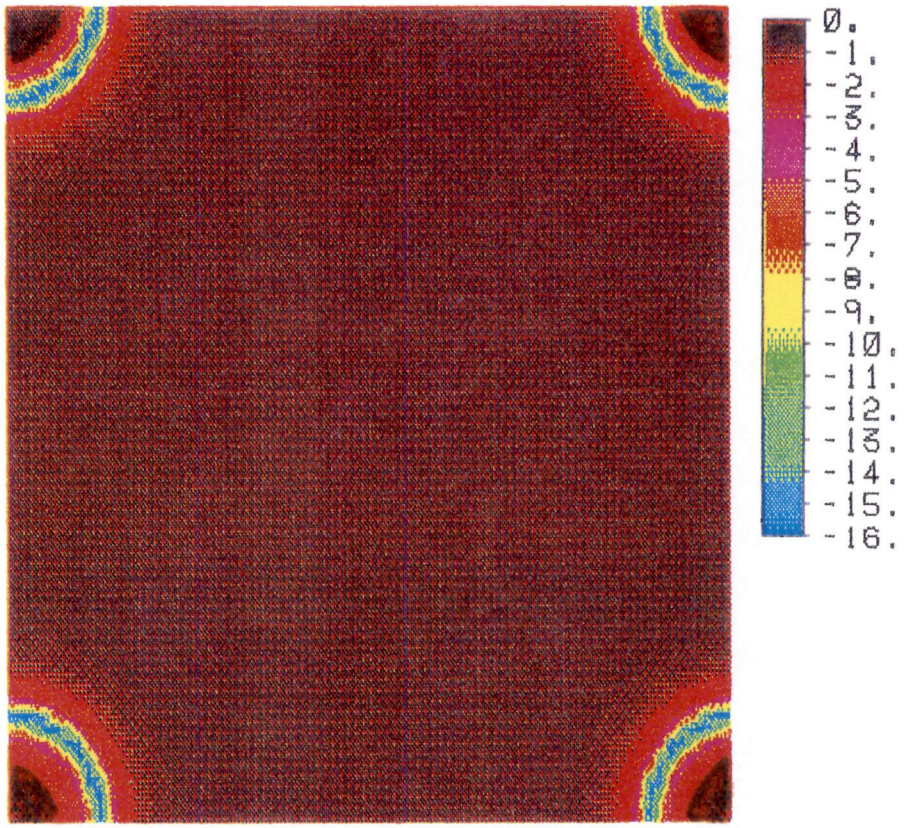

Figure 14: $\Im(\mathcal{F}\{G\})$ computed on a 64 x 64 grid, $\kappa = 0.5 - 0.03j$

ORIGINAL (NORMAL) ORDER

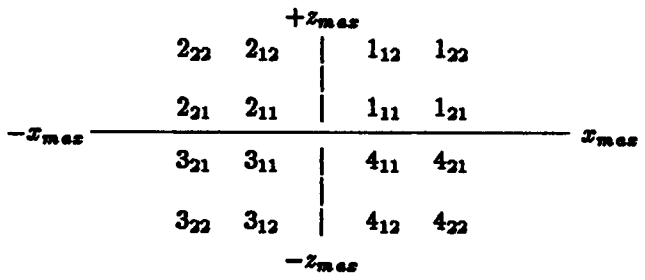

WRAP AROUND ORDER

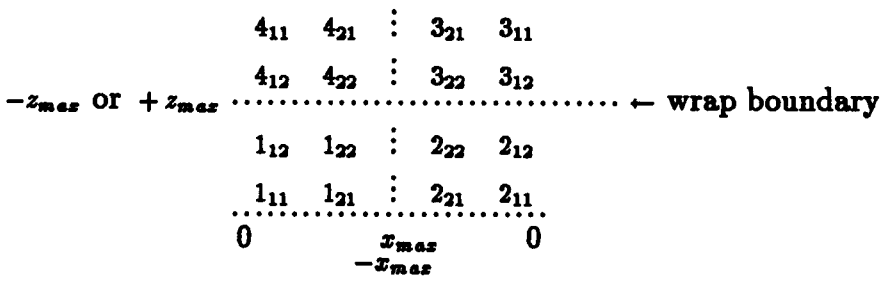

Figure 15: Schematic of wrap around order.

Figures 13 and 14 also illustrate another technique to prepare for a more accurate numerical inverse Fourier transformation. The maximum and minimum allowed values of $g(\Omega_x, \Omega_z)$ are "clipped" to those that suitably represent the appropriate delta function on a given spacing size. As the spacing size becomes smaller, that is as $\Delta\Omega \to 0$, these peak values become larger. For reasonable grid resolutions and values of κ_I, determined by other considerations yet to be discussed, these clipping limits are seldom reached.

Performing the inverse fast Fourier transform on the approximation to the function represented by equation (49) and depicted in Figures 13 and 14, results in an approximation to equation (50), which is shown in Figures 16 and 17. Comparing these to the exact solution represented by equation (57) and illustrated by Figures 11 and 12, several differences are apparent.

First, the IFFT results of Figures 16 and 17 are frequency limited with only 2x oversampling. Thus, the approximation, Figure 17, to the imaginary part of the exact solution, $-\frac{1}{4}J_0(\kappa\sqrt{x^2+z^2})$ is better than the approximation, Figure 16, is to the real part of the exact solution, $-\frac{1}{4}Y_0(\kappa\sqrt{x^2+z^2})$. This is not surprising since $-\frac{1}{4}Y_0(\kappa\sqrt{x^2+z^2})$ is singular at the origin and hence has an arbitrarily high frequency content there. Outside of this region, the numerical approximation to the real part is not too bad. The approximation to the imaginary part is pretty good everywhere. In both cases the region near the intersection of all four wrap boundaries (the center of Figures 16 and 17) is the exception.

Second, with the imaginary part of the wavenumber, κ_I, being only a "small" negative number, i.e. "low damping", significant energy propagates across the wrap boundaries causing increased errors to appear in the wave fields close to these boundaries. Of course, the requirement that κ_I be sufficiently negative

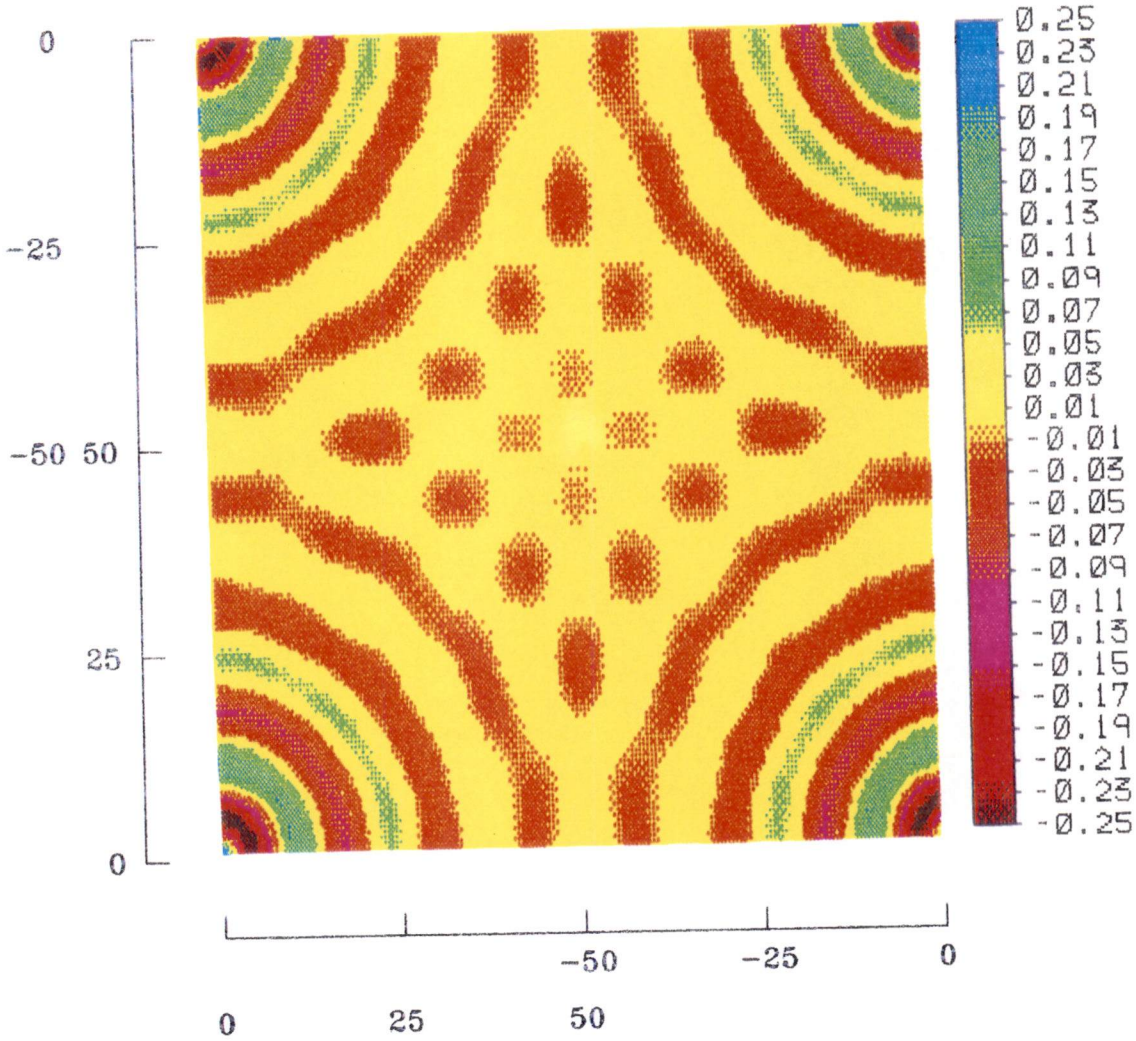

Figure 16: $\Re(G)$ found by IFFT on a 64 x 64 grid, $\kappa = 0.5 - 0.03j$

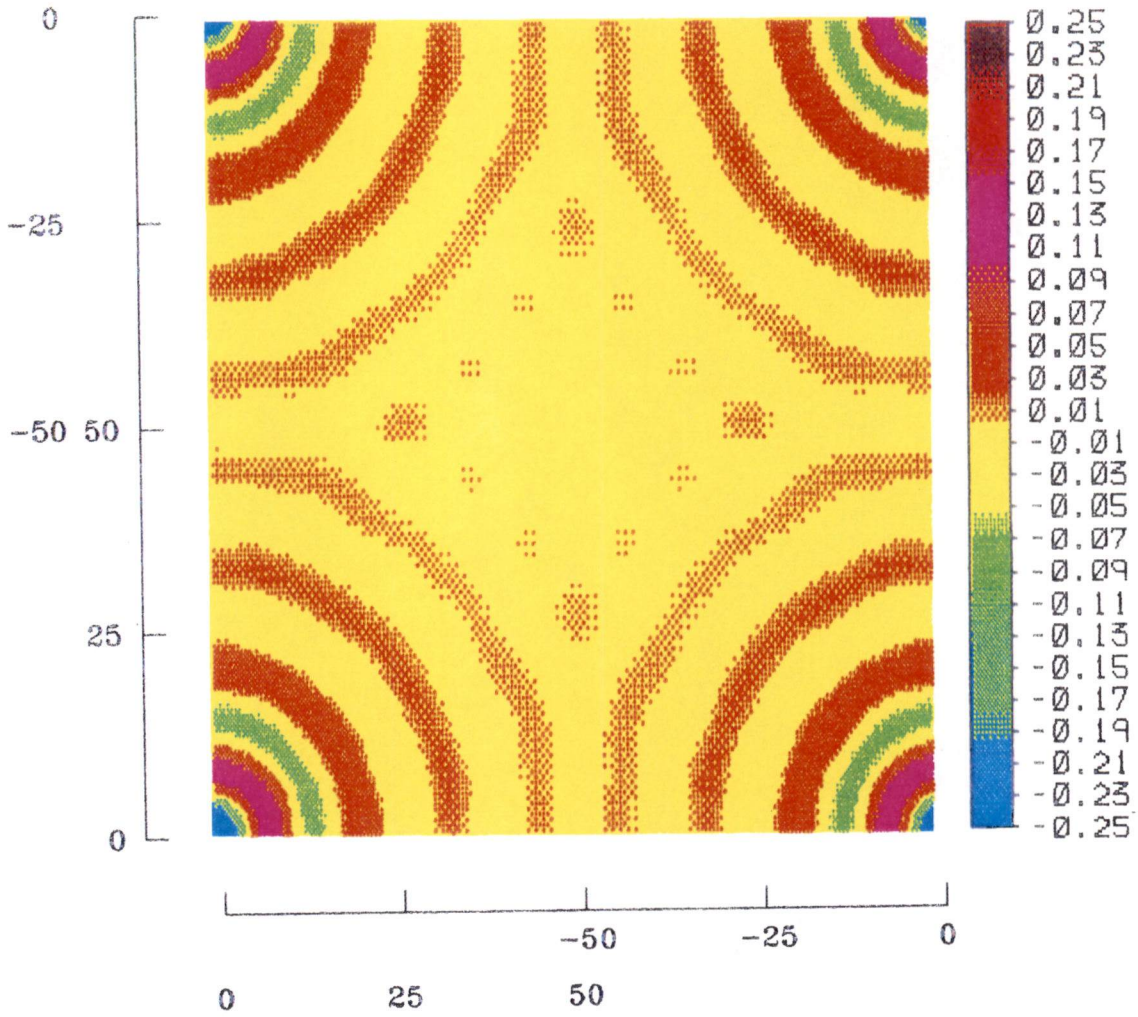

Figure 17: $\Im(G)$ found by IFFT on a 64 x 64 grid, $\kappa = 0.5 - 0.03j$

to damp out wave energy before it reaches a wrap boundary, is itself a source of error. One would hypothesize that if the grid size were increased while maintaining the same spatial sampling increments, Δx and Δz, that κ_I could be decreased (if desired) and better solutions out to larger distances from the origin could be obtained.

For notational simplicity, particularly in the next chapter, denote the IFFT operation by $\mathcal{F}^{-1}$ and the forward discrete transform by $\mathcal{F}$. Thus, the discrete approximation to $g(\Omega_x, \Omega_z)$ on which the IFFT operation ($\mathcal{F}^{-1}$) is to be performed can be written as $\mathcal{F}\{G\}$.

Increasing the grid size to 128 by 128 from 64 by 64 points while maintaining the same spatial sampling increments, Δx and Δz, in the x, z domain causes several changes. First, the wrap boundaries in the x, z domain are moved further out from the origin to twice the distance of the 64 by 64 grid case. Second, the spatial frequency increment, $\Delta\Omega$, in the discrete Ω_x, Ω_z space is halved. The resolution of $\mathcal{F}\{G\}$ in the discrete Ω_x, Ω_z domain is doubled. Finally, array storage requirements are quadrupled in this two-dimensional example. In three-dimensions the storage requirement would increase by eight times or 2^3 for double the resolution in all "spatial frequency" directions.

Figures 18 and 19 show respectively, the real and imaginary parts of the discrete approximation to $g(\Omega_x, \Omega_z)$, that is $\mathcal{F}\{G\}$, on the first quadrant of a 128 by 128 point grid with twice the spatial frequency resolution in all directions. They are considerably more circularly symmetric than those of Figures 13 and 14, with less of a "gridded" appearance. Note that for Figures 18 and 19, $\kappa_I = -0.01$, of less magnitude than that used on the courser grid of Figures 13 and 14. The "clipping limits" have also been doubled with halving $\Delta\Omega$.

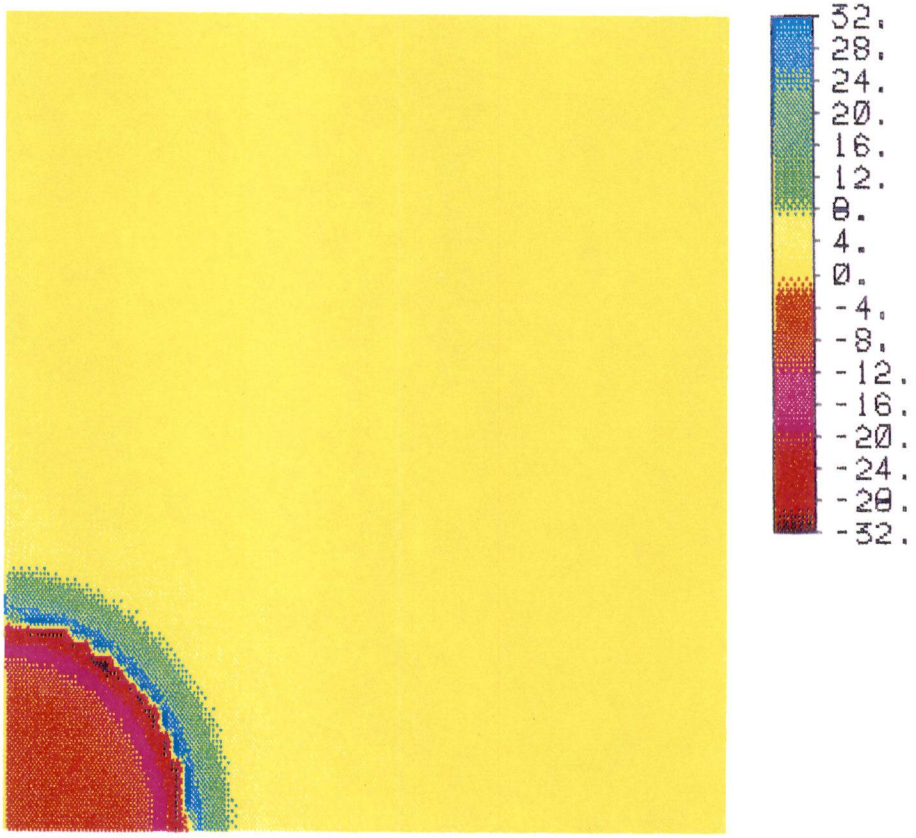

Figure 18: $\Re(\mathcal{F}\{G\})$ computed on a 128 x 128 grid, $\kappa = 0.5 - 0.01j$

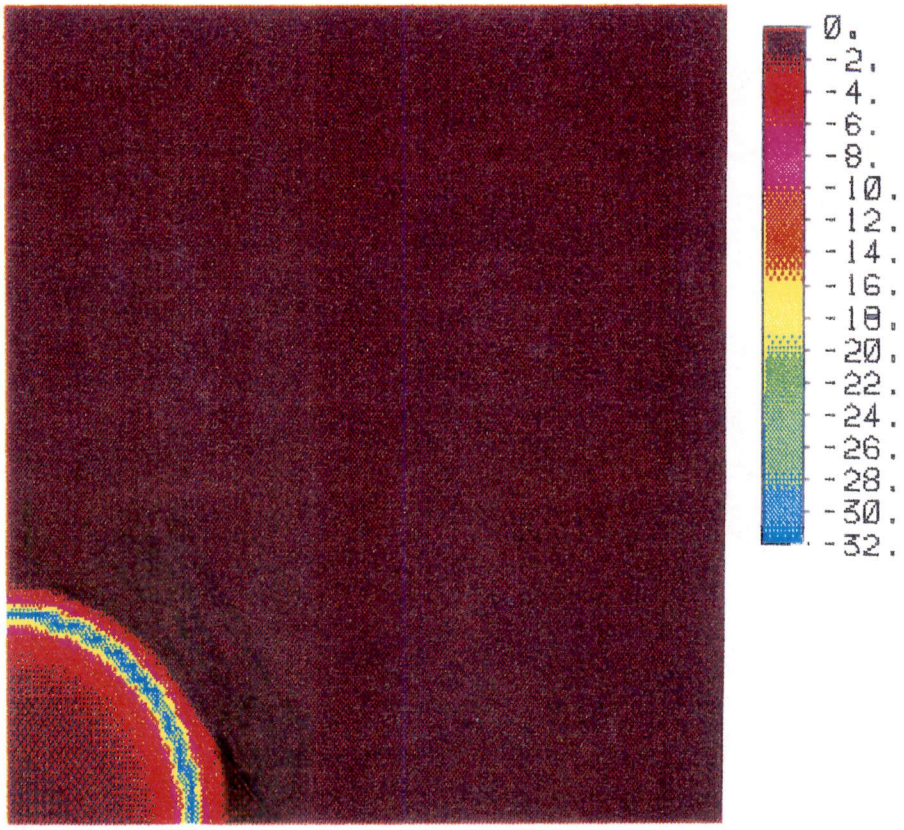

Figure 19: $\Im(\mathcal{F}\{G\})$ computed on a 128 x 128 grid, $\kappa = 0.5 - 0.01j$

Inverse transforming the functions shown on Figures 18 and 19 results in the real and imaginary parts of the approximation to $G(x,z)$ displayed in Figures 20 and 21, respectively. Comparing the results on the 128 by 128 point grid, Figures 20 and 21, to those of the 64 by 64 point grid, Figures 16 and 17, it is clear the wavefronts on the 128 by 128 grid extend further from the origin and also maintain their "coherency" better. Since the results of Figures 20 and 21 were computed using twice the spatial frequency resolution, their frequency content is twice that of the 64 by 64 grid cases depicted in Figures 16 and 17. Thus, they compare more favorably with the exact solutions illustrated in Figures 11 and 12.

Of course, the IFFT approximation to $\Re(G)$, still cannot capture the singularity at the origin of the real part of the exact solution, $-\frac{1}{4}Y_0(\kappa\sqrt{x^2+z^2})$, but it makes a better attempt. The IFFT approximation to $\Im(G)$ matches rather well with the imaginary part of the exact solution over most of the discrete x,z grid space. Except in a tiny neighborhood of the origin (and then only for the real part), it is apparent that as grid sizes and resolutions are increased that this method results in approximations that rapidly approach the exact Green's function.

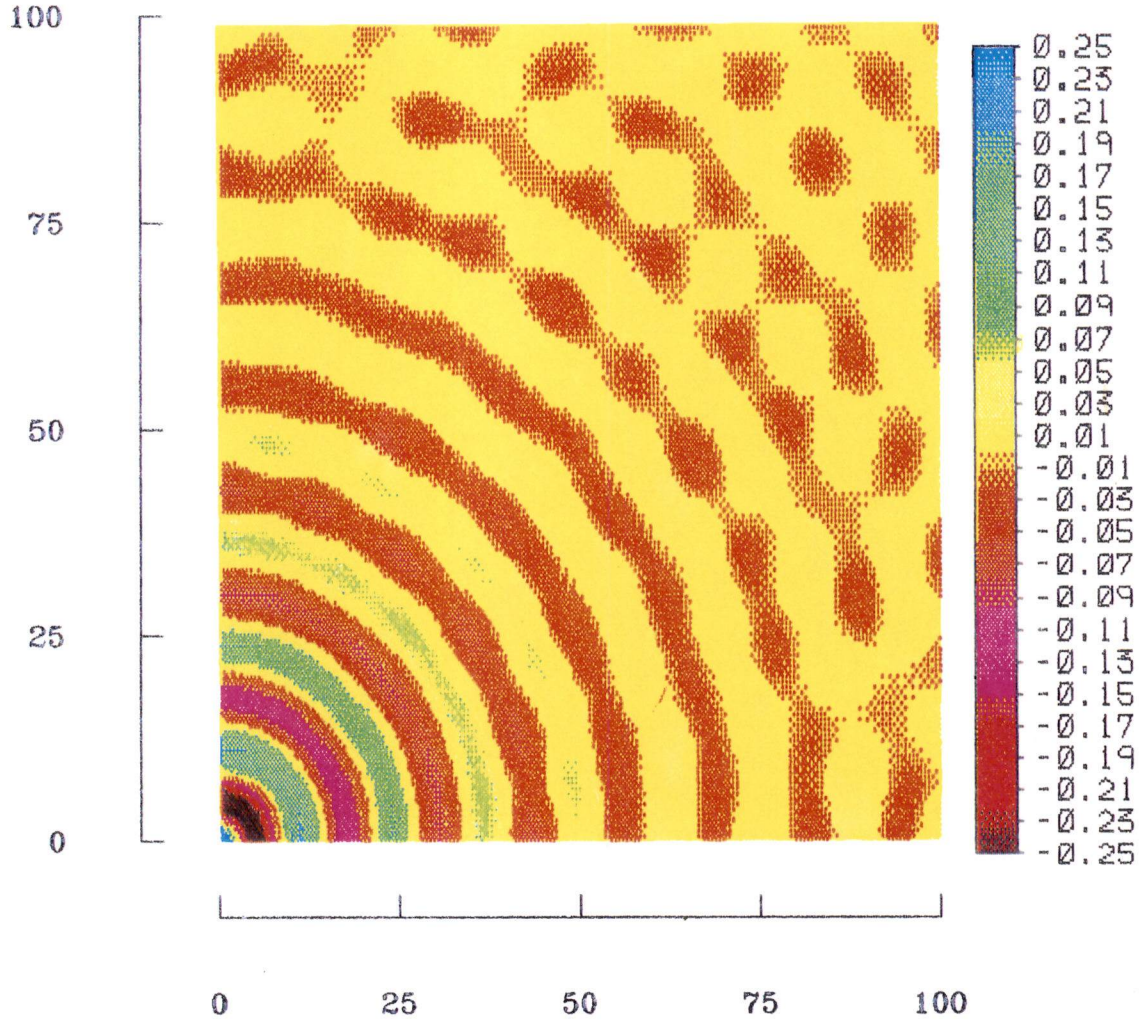

Figure 20: $\Re(G)$ found by IFFT on a 128 x 128 grid, $\kappa = 0.5 - 0.01i$

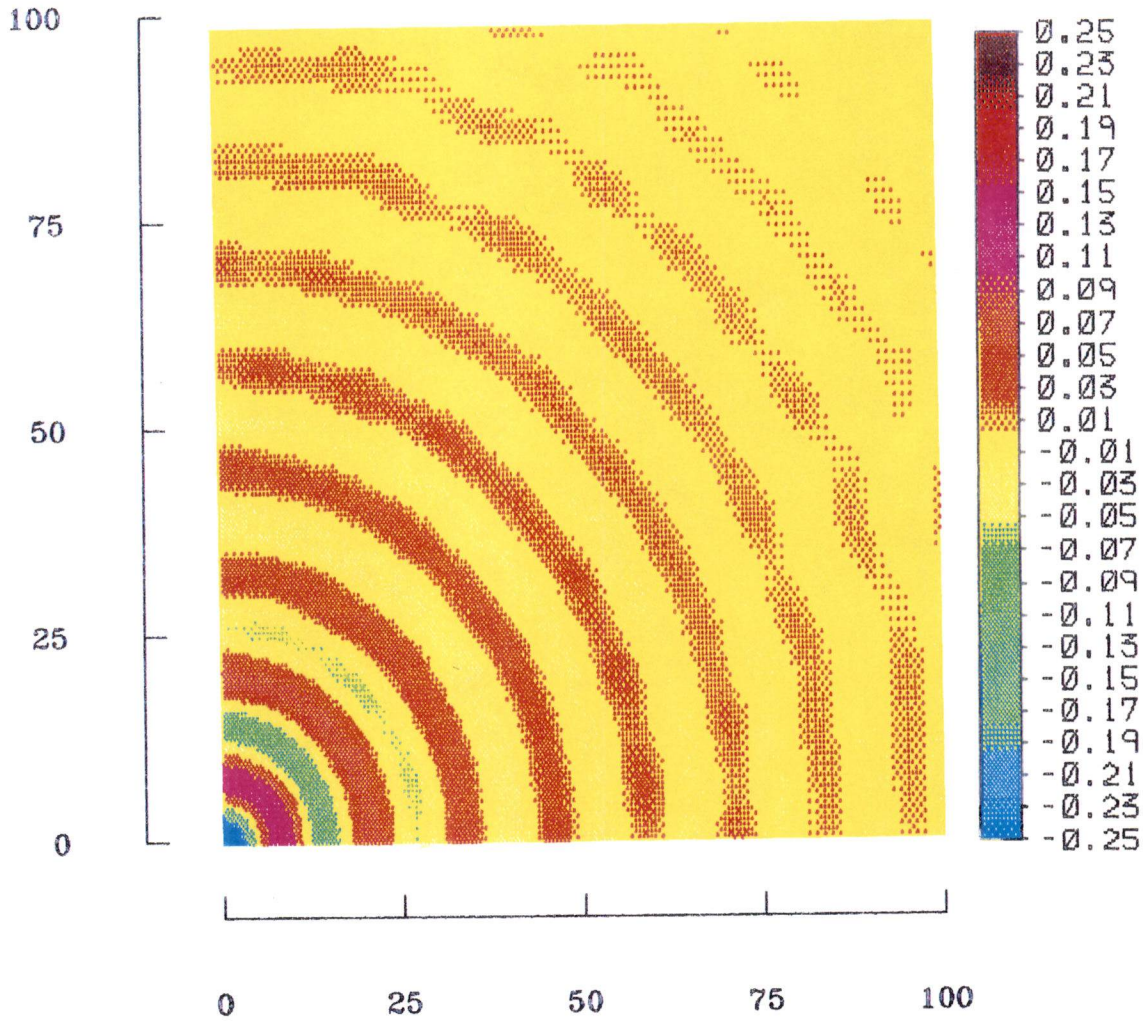

Figure 21: $\Im(G)$ found by IFFT on a 128 x 128 grid, $\kappa = 0.5 - 0.01j$

CHAPTER 3

NUMERICAL GREEN'S FUNCTIONS FOR THE INHOMOGENEOUS MEDIA HELMHOLTZ EQUATION

BACKGROUND

Wave propagation problems in inhomogeneous media, where the wave propagation velocity is variable in two or more directions, are presently (1992) solved almost exclusively using various variations and combinations of finite difference and finite element methods. Well-known papers describing finite difference methods are references [78–85]. Major publications covering finite element methods for wave propagation problems include [86–90]. The literature for both of these methods is vast and deep; the above listing is in no way comprehensive, but only illustrative. The solution of many practical wave propagation problems using finite differences or finite elements often requires the use of a supercomputer.

For certain frequency ranges and geometry restrictions, other methods exist that take advantage of simplifying assumptions. For example, "high" frequency waves in "gradually" varying media can often be approximated using a variety of "ray theoretical" methods [32,91–97]. If the inhomogeneity is in only one direction, multitudes of other "range invariant" methods can be used [92–103]. For many problems where the largest part of a medium's wave propagation speed variation occurs in one coordinate direction, such as in underwater acoustics, range invariant techniques are still used, even if the results are less than ideal [104–106]. Range invariant methods generally require a workstation computer (a few MFLOPS) to find solutions to practical problems in reasonable times

(tens of minutes to hours). Ray theoretic methods, when they can be used, often require less computing power.

The object of this chapter is to introduce a simple and quite general method to obtain solutions for wave propagation in inhomogeneous media. This method, here called the Iterative Dual Domain Method or IDDM, has the significant ancillary benefit of being orders of magnitude faster for sufficiently large problems, than those in prevalent use.

A PRELIMINARY ITERATIVE METHOD

The Helmholtz equation for media [34,63–68 with arbitrary spatial variation of wave propagation speed, c, can be written [107–110] in two dimensions as:

$$\nabla^2 u(x,z) + \kappa^2(x,z) \cdot u(x,z) = 0 \tag{59}$$

where,

$$\kappa^2(x,z) = \frac{\omega^2}{c^2(x,z)} \tag{60}$$

Thus the defining relation for the Green's function for the inhomogeneous media Helmholtz equation with a unit point source at the origin is:

$$\frac{\partial^2 G}{\partial x^2} + \frac{\partial^2 G}{\partial z^2} + \frac{\omega^2}{c^2(x,z)} G = -\delta(x,z) \tag{61}$$

Expressing the reciprocal of the wave propagation speed as:

$$\frac{1}{c^2(x,z)} = \frac{1}{c_0^2}\left[1 + \alpha(x,z)\right] \tag{62}$$

the wavenumber squared, κ^2, can be represented as:

$$\kappa^2(x,z) = \kappa_0^2 \left[1 + \alpha(x,z)\right] \tag{63}$$

that is κ^2 is separated into constant and variable or perturbed parts. The Green's function relation (61) then becomes:

$$\frac{\partial^2 G}{\partial x^2} + \frac{\partial^2 G}{\partial z^2} + \kappa_0^2 \left[1 + \alpha(x,z)\right] G = -\delta(x,z) \tag{64}$$

Denoting the two-dimensional Fourier transform of G by g, that is:

$$\mathfrak{F}\Big\{G(x,z)\Big\} = g(\Omega_x, \Omega_z) \tag{46}$$

the two-dimensional Fourier transform of equation (64) is:

$$-(\Omega_x^2 + \Omega_z^2)g + \kappa_0^2 g + \kappa_0^2 \, \mathfrak{F}\Big\{\alpha(x,z)\Big\} \star g = -1 \tag{65}$$

where the operation represented by $\star$ means two-dimensional convolution [52]. Moving the convolution term to the right-hand side and rearranging, results in:

$$\left[\kappa_0^2 - (\Omega_x^2 + \Omega_z^2)\right] g = -1 - \kappa_0^2 \, \mathfrak{F}\Big\{\alpha(x,z)\Big\} \star g \tag{66}$$

For $\alpha(x,z) = 0$, or constant propagation speed media, define g_0 to be the solution to:

$$\left[\kappa_0^2 - (\Omega_x^2 + \Omega_z^2)\right] g_0 = -1 \tag{67}$$

In other words, g_0, is just the Fourier transform of the solution to the constant media Helmholtz equation (44). When $\alpha(x,z)$ is "small", $\mathfrak{F}\{\alpha(x,z)\} \star g$ is also "small" so

$$\left[\kappa_0^2 - (\Omega_x^2 + \Omega_z^2)\right] g \cong -1 - \kappa_0^2 \mathfrak{F}\Big\{\alpha(x,z)\Big\} \star g_0 \tag{68}$$

This suggests an iterative procedure. Defining g_0 as the solution to (67) and g_1 to be the solution to (68) or:

$$\left[\kappa_0^2 - (\Omega_x^2 + \Omega_z^2)\right] g_1 = -1 - \kappa_0^2 \mathfrak{F}\Big\{\alpha(x,z)\Big\} \star g_0 \tag{69}$$

and further going on to define g_n as the solution to:

$$\left[\kappa_0^2 - (\Omega_x^2 + \Omega_z^2)\right] g_n = -1 - \kappa_0^2 \mathfrak{F}\Big\{\alpha(x,z)\Big\} \star g_{n-1} \tag{70}$$

will lead to a good approximation for g if enough steps are taken, i.e. n sufficiently large, and $\alpha(x,z)$ is sufficiently small. For $\alpha(x,z)$ sufficiently small, g_1 would be close to g_0; g_2 would be even closer to g_1, and so forth till g_n became almost identical to the previous iteration g_{n-1}. For media wave speed variations of less than about 5%, i.e. variations typical of many underwater acoustics problems, this iterative scheme appeared to work pretty well in practice. For $\alpha(x,z)$ "too" large, convergence is not obvious. However, for large $\alpha(x,z)$ there is yet a better way to construct an iterative solution, so this preliminary scheme will not be examined further.

Defining a sequence of α's such that $\alpha_0 = 0$ and $\alpha_n = \alpha(x,z)$, say:

$$\alpha_m(x,z) = m\left[\frac{\alpha(x,z)}{n}\right] \quad \forall m = 0,\ldots,n \quad m,n \in \mathbb{Z}^+ \tag{71}$$

an iteration scheme can be devised for which when the α's are sufficiently close, the iterative solutions for the g's are also close. In fact, for at least a large class of problems, the simple method of revising the parameter α of (71) is adequate. Noting that:

$$\mathfrak{F}\Big\{\alpha(x,z)\Big\} \star g(\Omega_x,\Omega_z) = \mathfrak{F}\Big\{\alpha(x,z)\Big\} \star \mathfrak{F}\Big\{G(x,z)\Big\} = \mathfrak{F}\Big\{\alpha(x,z)\cdot G(x,z)\Big\} \tag{72}$$

and using equation (71), an improved iterative algorithm based on that of equations (68–70) can be written as:

$$\left[\kappa_0^2 - (\Omega_x^2+\Omega_z^2)\right] g_0 = -1 \tag{73}$$

$$\left[\kappa_0^2 - (\Omega_x^2+\Omega_z^2)\right] g_1 = -1 - \kappa_0^2\,\mathfrak{F}\Big\{\alpha_1(x,z)\cdot G_0\Big\} \tag{74}$$

$$\left[\kappa_0^2 - (\Omega_x^2+\Omega_z^2)\right] g_2 = -1 - \kappa_0^2\,\mathfrak{F}\Big\{\alpha_2(x,z)\cdot G_1\Big\} \tag{75}$$

$$\vdots$$

$$\left[\kappa_0^2 - (\Omega_x^2+\Omega_z^2)\right] g_m = -1 - \kappa_0^2\,\mathfrak{F}\Big\{\alpha_m(x,z)\cdot G_{m-1}\Big\} \tag{76}$$

$$\vdots$$

$$\left[\kappa_0^2 - (\Omega_x^2+\Omega_z^2)\right] g_n = -1 - \kappa_0^2\,\mathfrak{F}\Big\{\alpha_n(x,z)\cdot G_{n-1}\Big\} \tag{77}$$

If $\kappa_0 \in \mathbb{C}$ such that:

$$\kappa_0 = \kappa_R + j\kappa_I \quad \kappa_R, \kappa_I \in \mathbb{R} \tag{78}$$

then the $[\kappa_0^2 - (\Omega_x^2 + \Omega_z^2)]$ terms in equations (73–77) can never be zero if $\kappa_I \neq 0$.

For $\kappa_I \neq 0$ and using the techniques of Chapter 2: letting both the space and transform-space coordinates be real and discrete, and numerically approximating the Fourier transform $\mathfrak{F}$ by the fast Fourier transform $\mathcal{F}$, results in the following iterates for the Green's function of equation (61):

$$G_0 = \mathcal{F}^{-1}\left\{\frac{-1}{\kappa_0^2 - (\Omega_x^2 + \Omega_z^2)}\right\} \tag{79}$$

$$G_1 = \mathcal{F}^{-1}\left\{\frac{-1 - \kappa_0^2\,\mathcal{F}\{\alpha_1 G_0\}}{\kappa_0^2 - (\Omega_x^2 + \Omega_z^2)}\right\} \tag{80}$$

$$\vdots$$

$$G_m = \mathcal{F}^{-1}\left\{\frac{-1 - \kappa_0^2\,\mathcal{F}\{\alpha_m G_{m-1}\}}{\kappa_0^2 - (\Omega_x^2 + \Omega_z^2)}\right\} \tag{81}$$

$$\vdots$$

$$G_n = \mathcal{F}^{-1}\left\{\frac{-1 - \kappa_0^2\,\mathcal{F}\{\alpha_n G_{n-1}\}}{\kappa_0^2 - (\Omega_x^2 + \Omega_z^2)}\right\} \tag{82}$$

As in Chapter 2, the choice of sign of κ_I affects the type of boundary conditions. Incoming wave boundary conditions result if κ_I is positive, κ_I negative yields outgoing or radiating wave conditions. Here, only iterates obeying outgoing wave boundary conditions are of present interest, so κ_I was given small negative (real) values only.

Examining equations (79–82), it is apparent that each iteration except the first (79) requires one forward fast Fourier transform $\mathcal{F}$, and one inverse fast Fourier transform $\mathcal{F}^{-1}$. Since each iteration cycle uses **both** the spatial x, z and the transformed Ω_x, Ω_z coordinate domains, the name Iterative Dual Domain Method, or IDDM has been coined for this algorithm.

The fast transforms used in the IDDM are subject to the same considerations discussed in Chapter 2, as well as a few others related to media variations. One such additional consideration is the careful avoidance of aliasing. Each wavelength in the spatial x, z domain **must** be sampled at least twice. Thus, the slowest wave propagation speed regions, those with the largest positive $\alpha(x, z)$ values, determine the highest frequency computable on a given grid spacing. As discussed in Chapter 2, some level of oversampling is generally desirable. Regions with faster wave propagation speeds, i.e. longer wavelengths, are then more oversampled.

Another consideration is that ideally $\alpha(x, z)$ should have no discontinuities across the wrap boundaries or errors will appear in the forward transform of the αG products. The examples in this dissertation do not have any discontinuities of α across wrap boundaries. This is not a severe restriction in practice since for an arbitrary $\alpha(x, z)$ these errors can be reduced to negligible values by expanding the grid and tapering at the edges. This is the same well-known problem, with well-known solutions, as design of windowing functions for use with (perhaps multidimensional) digital filters. References [34,63–68,76,77], among others, address this issue in some depth.

Chapter 2 also discussed choosing κ_I to be sufficiently negative so that the amplitudes of waves radiating across the wrap boundaries are sufficiently small. This is particularly important in the IDDM, since excessive energy crossing the

wrap boundaries will result in divergence. This can become rather tricky for some configurations, such as waveguides, that focus or direct waves toward a wrap boundary. In practice, this problem can be overcome by increasing the spatial extent of the grid, particularly in the direction of the focused waves.

For grids of sufficiently large spatial extent and with κ_I sufficiently negative to allow the IDDM to converge, convergence was obtained after 30–45 iterations for all cases illustrated in this dissertation and in all numerical experiments to date. Letting I represent the number of iterations, if the solution remained the same within 4% of the imaginary part's peak value for all grid points from I iterations to $I + 5$ iterations, the solution was considered to have **converged** in I iterations. The imaginary part's peak value is used, since the imaginary part is bounded.

FOCUSING THROUGH A CIRCULAR LENS

Figure 22 depicts the variation of media wave speed $\alpha(x, z)$ for an inhomogeneity consisting of an embedded circle of radius 16 units with its center at (26,26). This two-dimensional configuration represents an approximation to a thick cylindrical lens. The interior of the circle has a value for α of 0.75, the exterior has α equal to zero. Thus, the interior of the circle has a wave propagation speed about 76% of the exterior value. The spatial extent of the $\alpha(x, z)$ used in the computation was $-100 \leq x \leq 100$ and $-100 \leq z \leq 100$. Only the first quadrant of a 128 by 128 point grid is shown in Figure 22, the other quadrants all had $\alpha = 0$. Note there are no discontinuities across wrap boundaries when α is arranged in wrap around order.

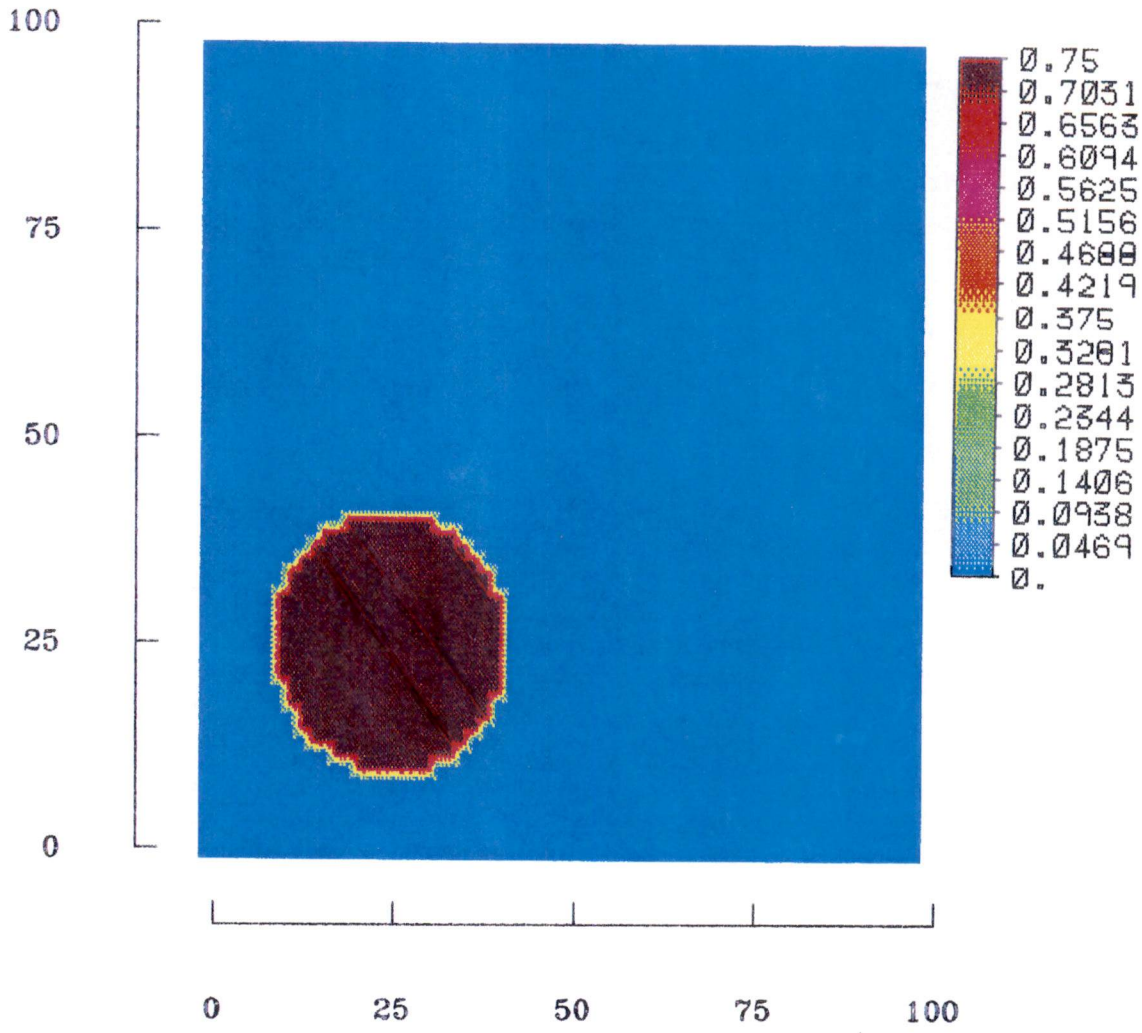

Figure 22: Variation of α in media, circle interior propagation velocity 76% of exterior

For very high frequencies where ray theory becomes valid, the focal length of this "thick circular lens" can be found from:

$$f' = \frac{R(2 - n_r)}{2(n_r - 1)} \tag{83}$$

where R is the radius of the circle and n_r is the index of refraction [111]. The particular geometry of Figure 22 results in a focal length of about 16.8 units. In other words, waves of a sufficiently high frequency emanating from a point source 16.8 units away on one side of the circle would emerge as plane waves on the other side. A point source located at a distance greater than the focal length away from the circle would give rise to waves that focused on the other side. The geometry of Figure 22 has the circle about 20.8 distance units away from the point source at the origin. Thus, one would expect focusing phenomena to appear on the opposite side of the circular inhomogeneity at relatively high frequencies.

The results of 45 iterations of the Iterative Dual Domain Method on a 128 by 128 point grid for the media inhomogeneity depicted in Figure 22 are displayed as Figures 23 and 24 for $\kappa_0 = 0.5 - 0.03j$. Figure 23 shows the real part of the numerical Green's function; the imaginary part is shown as Figure 24. Both Figures 23 and 24 show the wavefronts "slowed down" by the circular inhomogeneity and the resulting focusing behind it. The other quadrants do not contain any inhomogeneities and the solution in them has nearly the same circularly symmetric appearance as the homogeneous media numerical Green's function. A partial exception is the fourth quadrant which shows some of the focused energy from the first quadrant crossing its wrap boundaries. As was the case for Green's functions computed in homogeneous media, the singularity of the real part at

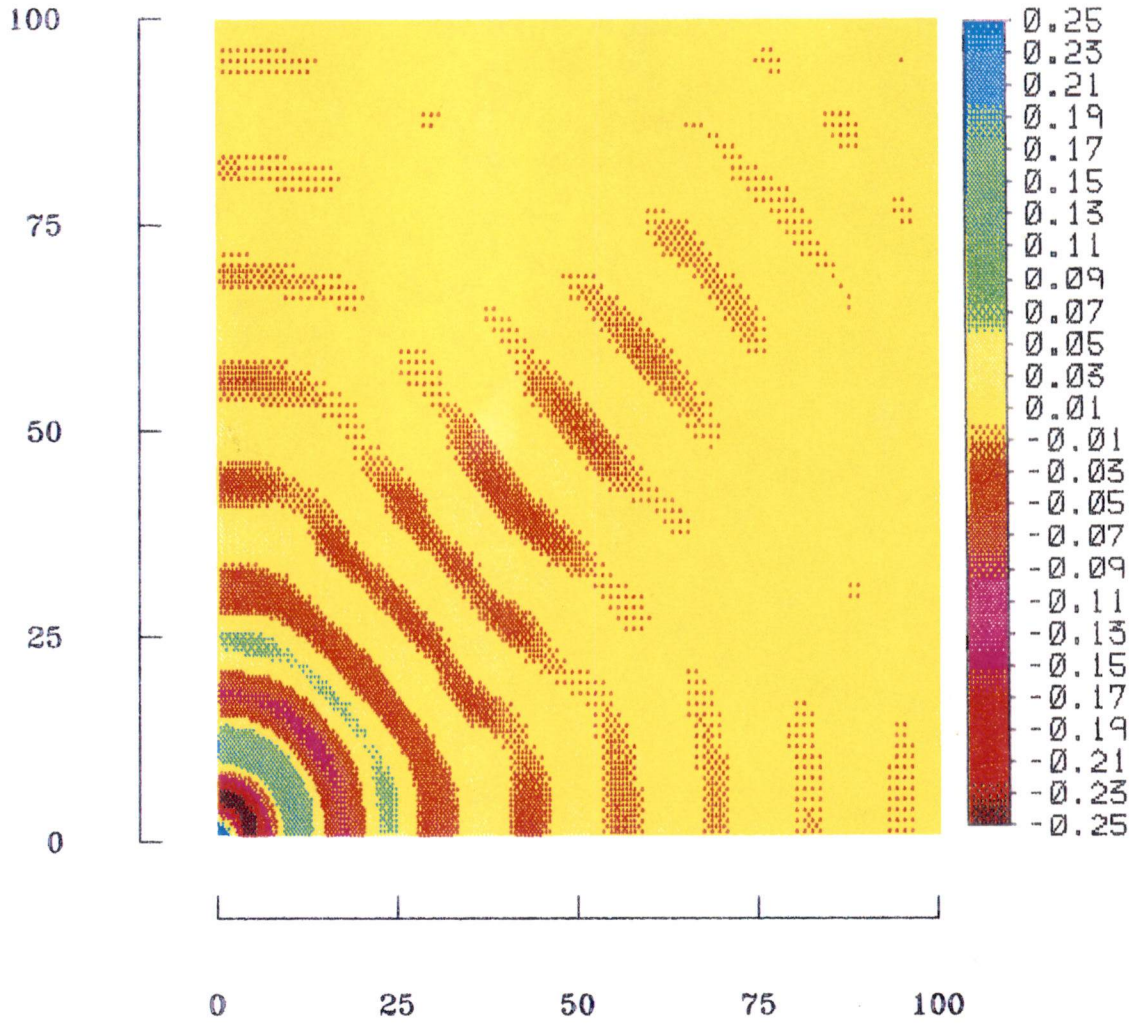

Figure 23: Focusing of $\Re(G)$ through circle with interior propagation velocity 76% of exterior, $\kappa_0 = 0.5 - 0.03j$

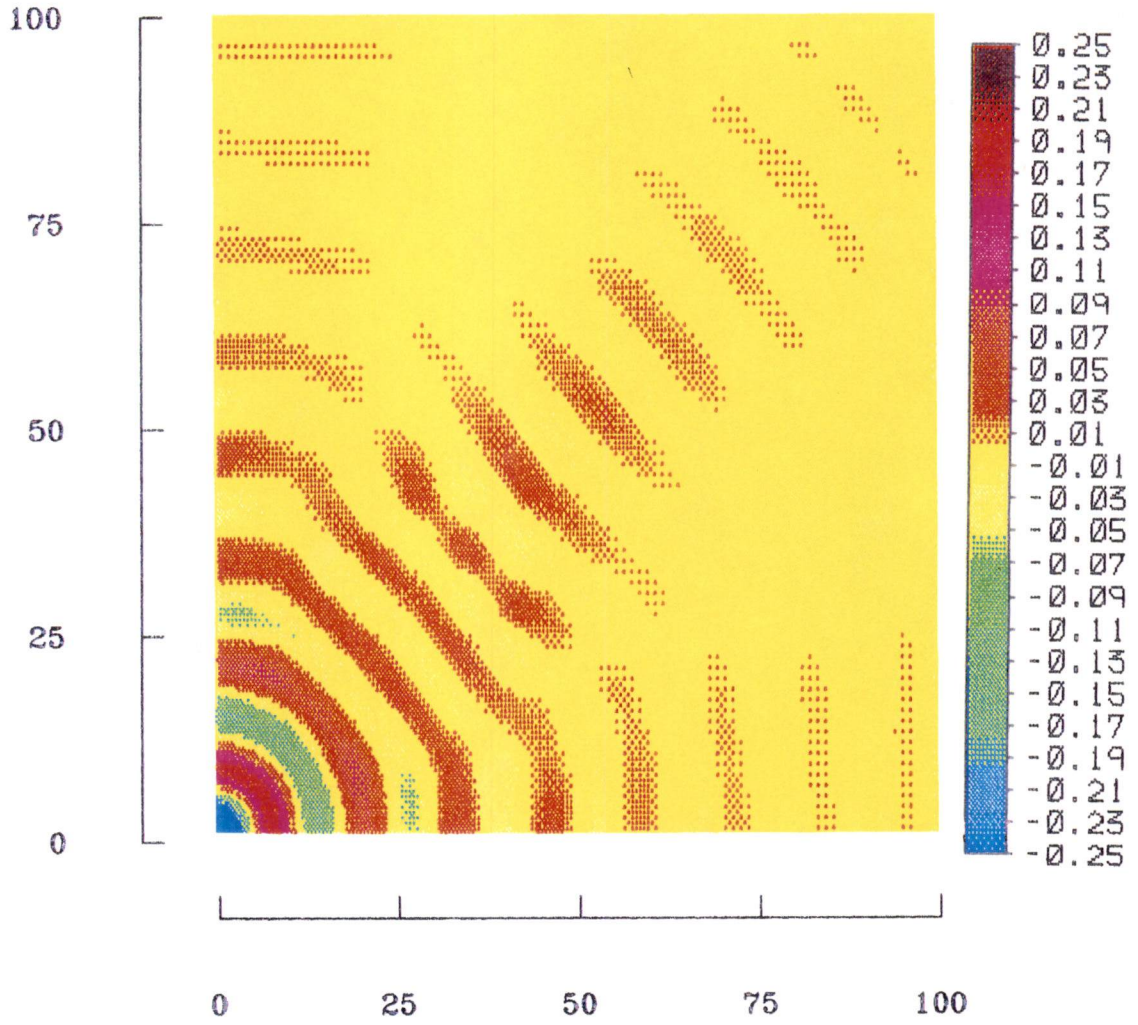

Figure 24: Focusing of $\Im(G)$ through circle with interior propagation velocity 76% of exterior, $\kappa_0 = 0.5 - 0.03j$

the origin cannot be captured using inherently high frequency limited discrete Fourier transformations. At a frequency corresponding to $\kappa_R = 0.5$, the exterior of the circle is 2x oversampled. Interior to the circle the propagation velocity is lower, the wavelength shorter, so it is only 1.52x oversampled.

The Fourier transform of the results of Figures 23 and 24 are illustrated in part by Figures 25 and 26. These are the first quadrants of the real and imaginary parts of g_n immediately prior to inverse transformation to yield G_n of Figures 23 and 24. Despite the considerable differences between the results for inhomogeneous media, Figures 23 and 24, and homogeneous media, Figures 20 and 21, the transform domain results do not appear that much different. Comparing the inhomogeneous transform results, Figures 25 and 26, to their corresponding homogeneous transform results, Figures 18 and 19, one sees the inhomogeneous real part has a less pronounced "doublet ring" behavior, and the imaginary part has a wider "halo" around its "delta function ring". This indicates that the behavior of the transformed Green's functions may not be at all intuitive.

Figures 27 and 28 illustrate the Green's function for the media variation of Figure 22, at half the frequency of Figures 23–26. For $\kappa_0 = 0.25 - 0.03j$ the circular inhomogeneity causes much less focusing with the wavefronts more readily diffracting around it. Since the frequency is half, the results of Figures 27 and 28 are oversampled twice as much as those of Figures 23 and 24. The region outside the circle is oversampled 4x, the interior 3x. As a consequence, each wavefront shows relatively more detail.

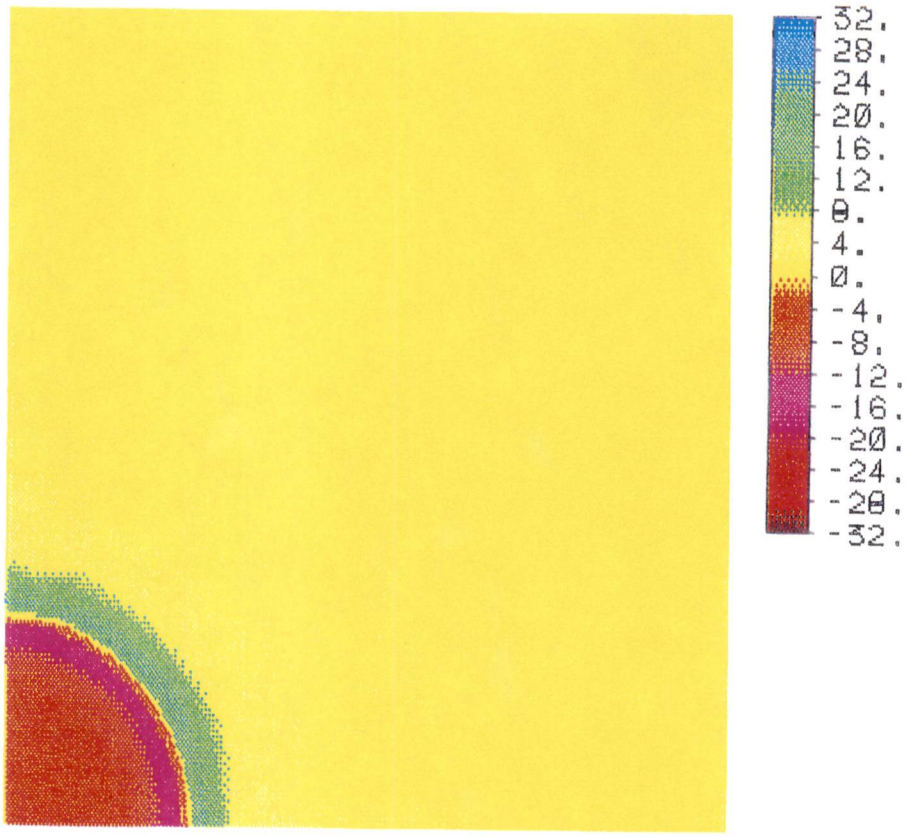

Figure 25: First quadrant of $\Re(\mathcal{F}\{G\})$ for circle with interior propagation velocity 76% of exterior, $\kappa_0 = 0.5 - 0.03j$

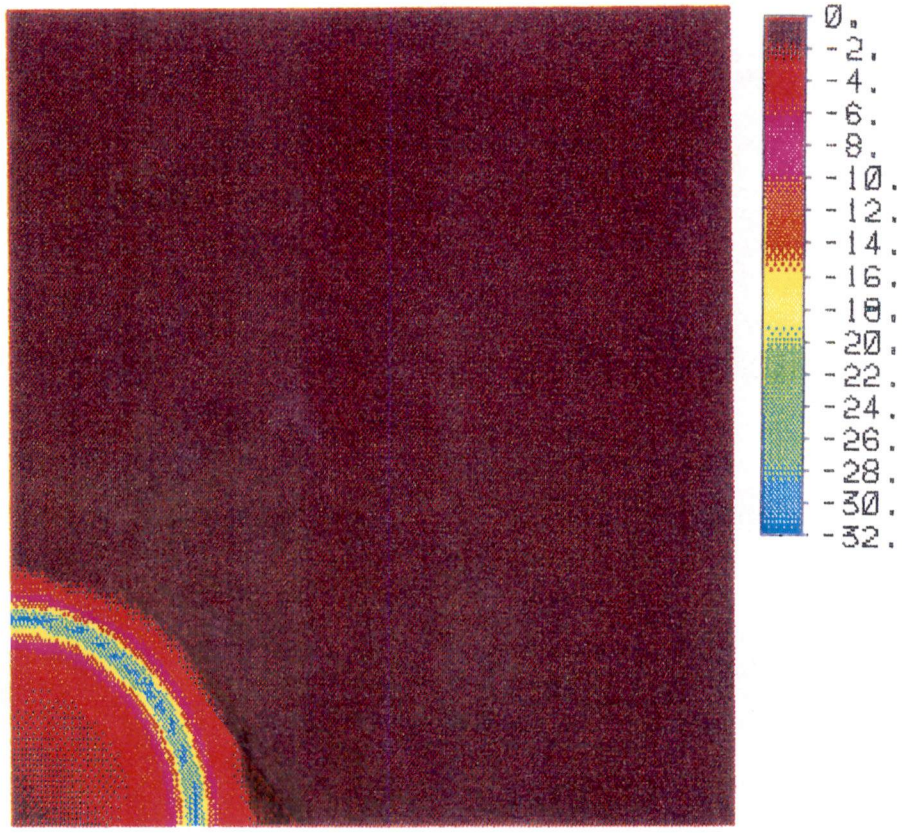

Figure 26: First quadrant of $\Im(\mathcal{F}\{G\})$ for circle with interior propagation velocity 76% of exterior, $\kappa_0 = 0.5 - 0.03j$

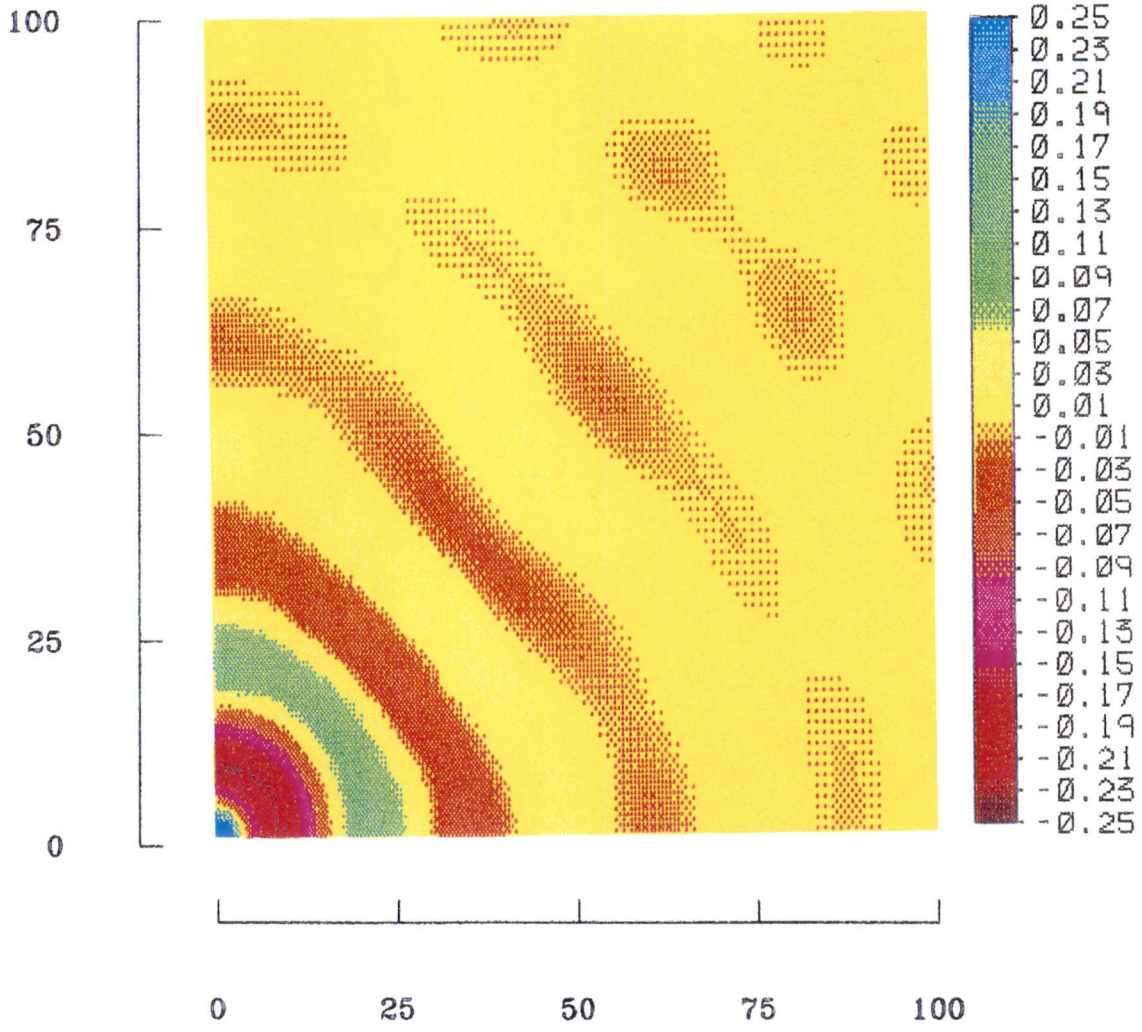

Figure 27: Less focusing and greater diffraction at lower frequencies, $\kappa_0 = 0.25 - 0.03j$, $\Re(G)$ through circle with interior propagation velocity 76% of exterior

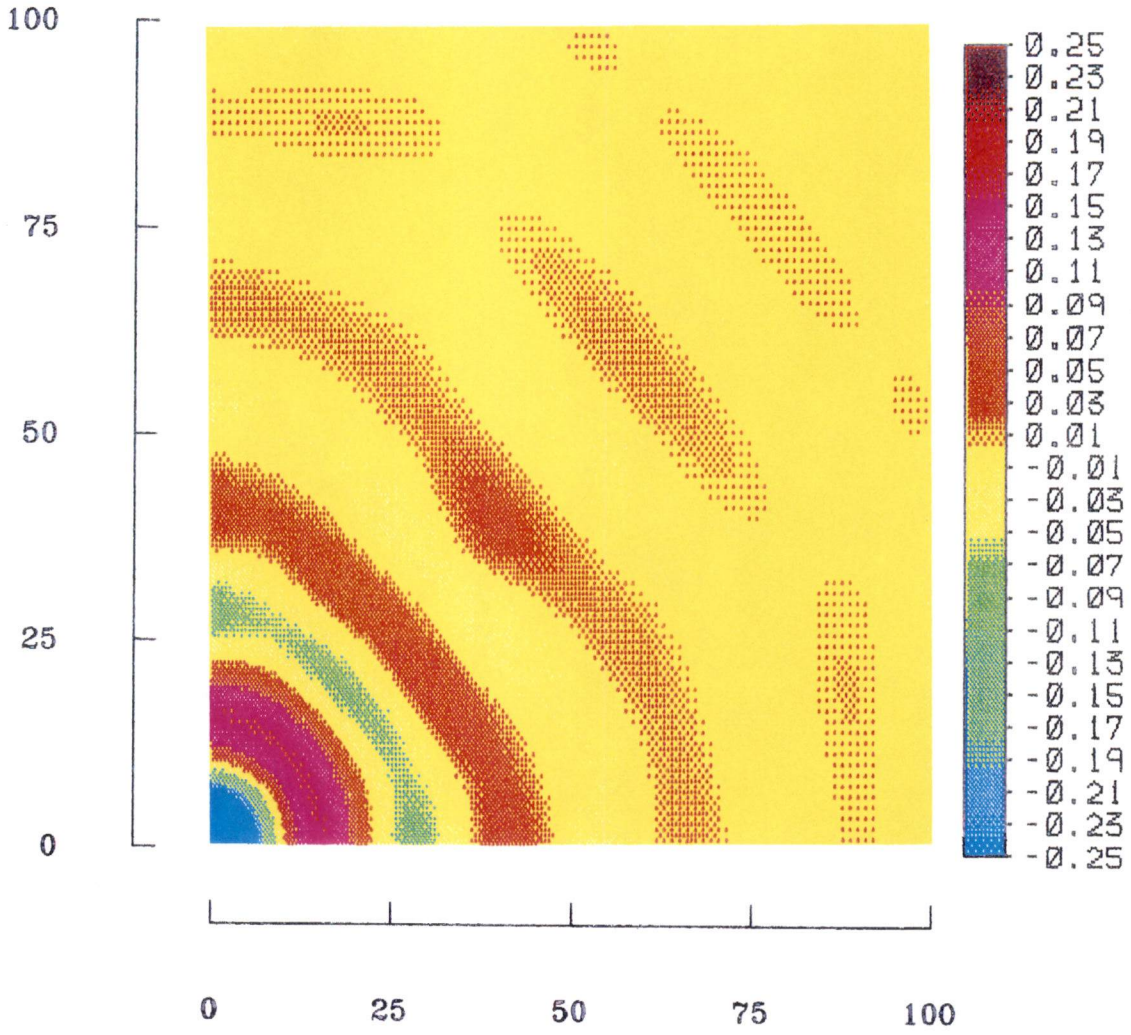

Figure 28: Less focusing and greater diffraction at lower frequencies, $\kappa_0 = 0.25 - 0.03j$, $\Im(G)$ through circle with interior propagation velocity 76% of exterior

SCATTERING BY A HIGHER SPEED CIRCULAR INCLUSION

Similar to the geometry of the previous section, Figure 29 depicts another variation of media wave speed $\alpha(x,z)$ for a circle of radius 16 units with its center at (26,26). The interior of the circle has a value of $\alpha = -0.75$, the exterior has α equal to zero. Thus, the interior of the circle has a wave propagation speed 200% of the exterior value. As in the previous section the spatial extent of $\alpha(x,z)$ used in computations was $-100 \leq x \leq 100$ and $-100 \leq z \leq 100$, with only the first quadrant of the 128 by 128 point grid shown in Figure 29.

When a wave impinges on such a relatively large, smooth solid inhomogeneity, the inhomogeneity reacts to the incoming wave in a multitude of ways. A number of the effects are described in the book by R. J. Urick [96]. First, the wave can generate a specularly reflected echo from the front of the inhomogeneity. The wave can further enter the circular inhomogeneity of Figure 29 and be reflected from the back side to produce a secondary echo. Also diffracted or "creeping" waves originate on the edge of the geometrical shadow and travel around the circle with the wave propagation speed of the exterior medium. Compounding the complexity, the inhomogeneity may oscillate internally in the neighborhood of one or more resonant frequencies, giving rise to "resonant scattering". Finally, all these wave phenomena reradiate in various directions as they travel in and around the inhomogeneity. For a circular inhomogeneity such as that of Figure 29 for $\kappa_R R > 2$, where R is the radius of the circle, one would expect forward scattering and reradiation from the circle to occur [112]. Further, the forward scattering should be less than that for a perfectly rigid inhomogeneity.

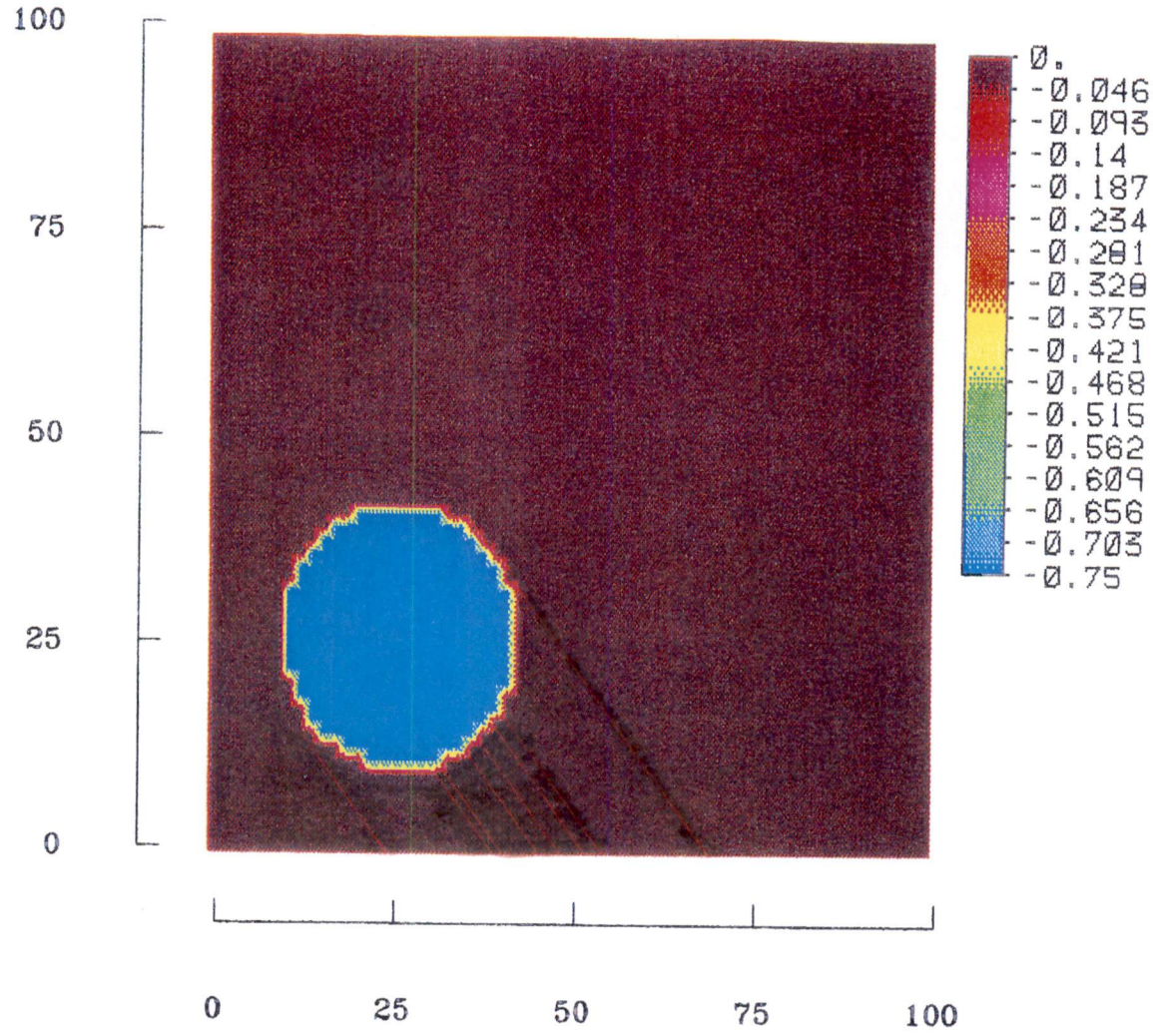

Figure 29: Variation of α in media, circle interior propagation velocity 200% of exterior

The results of 45 iterations of the IDDM on a 128 by 128 point grid for the media inhomogeneity depicted in Figure 29 are displayed as Figures 30 and 31 for $\kappa_0 = 0.5 - 0.03j$. Figure 30 shows the real part of the numerical Green's function; the imaginary part is shown as Figure 31. Both Figures 30 and 31 show the intricate wave field inside the circular inhomogeneity and the reradiation of energy from it. The region between the point source at the origin and the near surface of the circular inhomogeneity clearly shows the echo or backscatter from this surface.

For the configuration of Figure 29 at $\kappa_R = 0.5 - 0.03j$, with respect to the exterior medium $\kappa_R R = 8$. With respect to the interior medium $\kappa_R R = 4$. Since the media velocity contrast is not as great as it would be for a rigid circular inclusion [113,114], the forward radiation pattern of Figures 30 and 31 should not be as severe. In fact, this is the case. On the other hand, the forward radiation pattern should be more pronounced for the present case of double the wave speed interior to the circular inclusion than that of reference [115] for $\kappa R = 4$ where the wave speed variation was 140%. This is also true. The treatise by D. S. Jones [109] supplies scattering coefficients which can be used to estimate the amplitude of the forward scatter. The mean forward scattering coefficient (interpolated for $\kappa_R R = 4$ with respect to the interior medium) indicates the wave amplitudes immediately forward of the circular inclusion should be about double what they would have otherwise been in the absence of the inclusion. Comparing the wave magnitudes at this location in Figures 30 and 31 to those for the homogeneous media, Figures 20 and 21, one observes this is indeed the case. These comparisons have been made with scattering of an incident plane wave, not a point source, so the quantitative behavior of the solutions shown in Figures 30 and 31 is only approximately verified. Also, the results of Figures 30 and 31

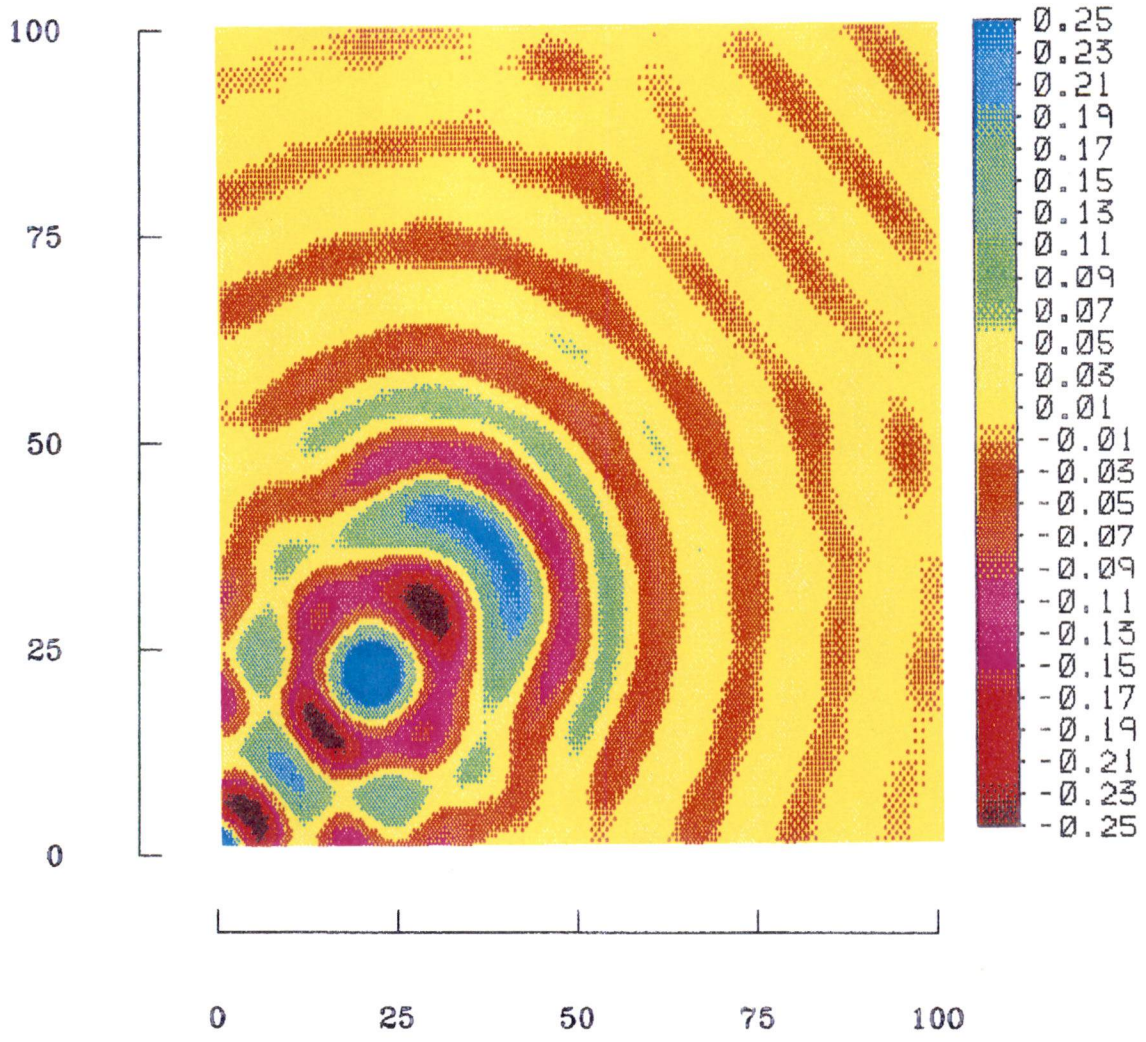

Figure 30: Scattering of $\Re(G)$, circle with interior propagation velocity 200% of exterior, $\kappa_0 = 0.5 - 0.03j$

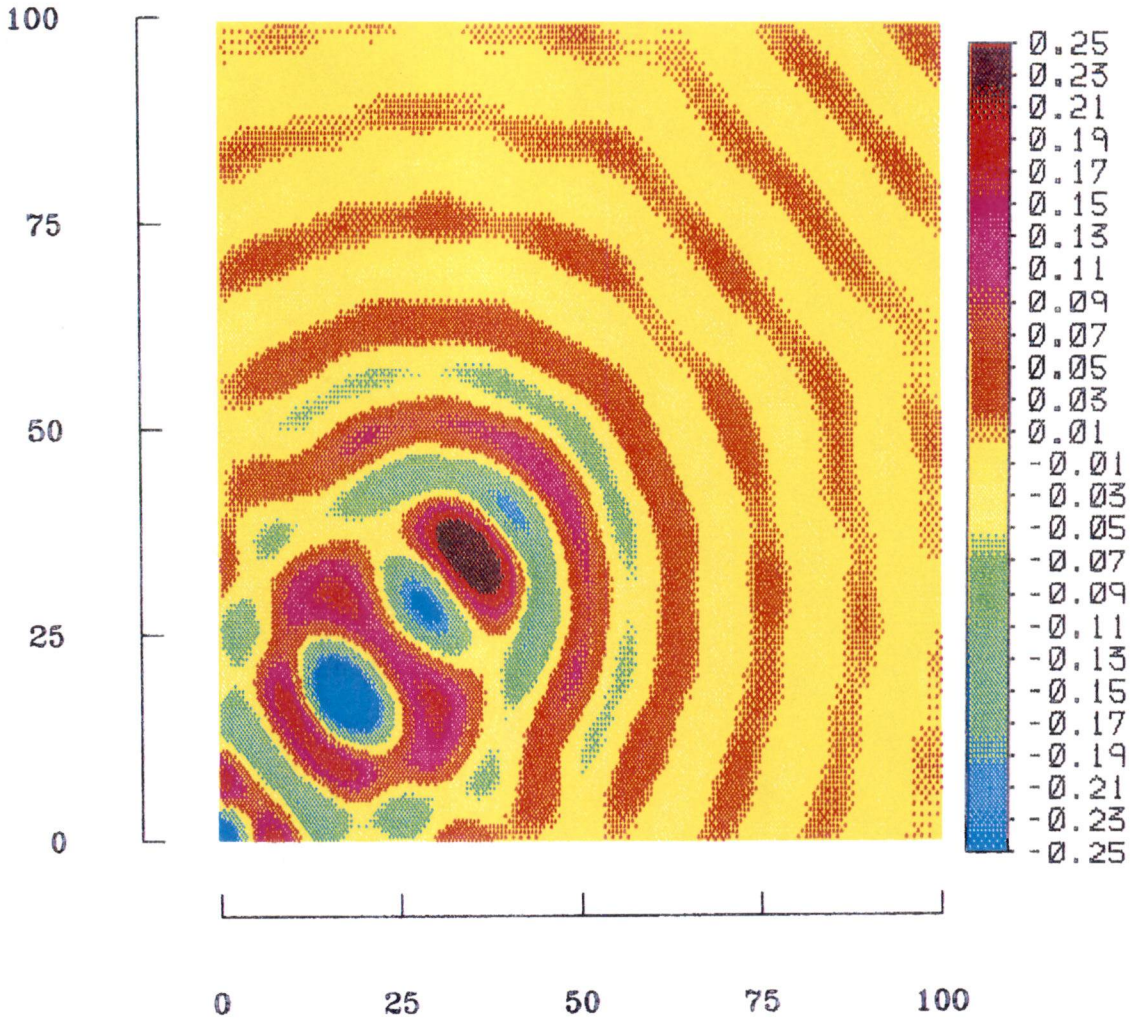

Figure 31: Scattering of $\Im(G)$, circle with interior propagation velocity 200% of exterior, $\kappa_0 = 0.5 - 0.03j$

are for a complex $\kappa = 0.5 - 0.03j$ with a relatively high damping value of $\kappa_I = -0.03$, whereas the previously published results are for negligible damping. However, the qualitative behavior is correct and the quantitative results are quite reasonable.

The Fourier transform of the results of Figures 30 and 31 are illustrated in part by Figures 32 and 33. These are the first quadrants of the real and imaginary parts of g_n. Figures 32 and 33 are radically different in appearance than any other previously displayed transform domain results. This demonstrates the IDDM iterations for the g's in transform space can converge to solutions much different than their starting values. Although the pictures of Figures 32 and 33 are hardly intuitive in their meaning, they do make some sense. Note the high amplitude "ridge" of both the real and imaginary parts of g_n, Figures 32 and 33, respectively. The direction or orientation of this ridge in Ω_x, Ω_z space is perpendicular to the axis of high amplitudes in untransformed x, z space. This is consistent with the properties of two-dimensional Fourier transforms pictorially illustrated in the book by R. C. Gonzalez and P. Wintz [68].

Figures 34 and 35 display the Green's function for the media variation of Figure 29, at half the frequency of Figures 30–33. For $\kappa_0 = 0.25 - 0.03j$, the higher speed circular inhomogeneity causes much less scattering with the wavefronts more readily diffracted around it. Comparison to published scattering results [112–115] indicates the forward radiation pattern, now much less dramatic than the high frequency case, has the correct shape. The faster propagation of the wave fronts and the corresponding stretching of the wavelengths through the circular inhomogeneity are apparent in both the real and imaginary parts, Figures 34 and 35, respectively.

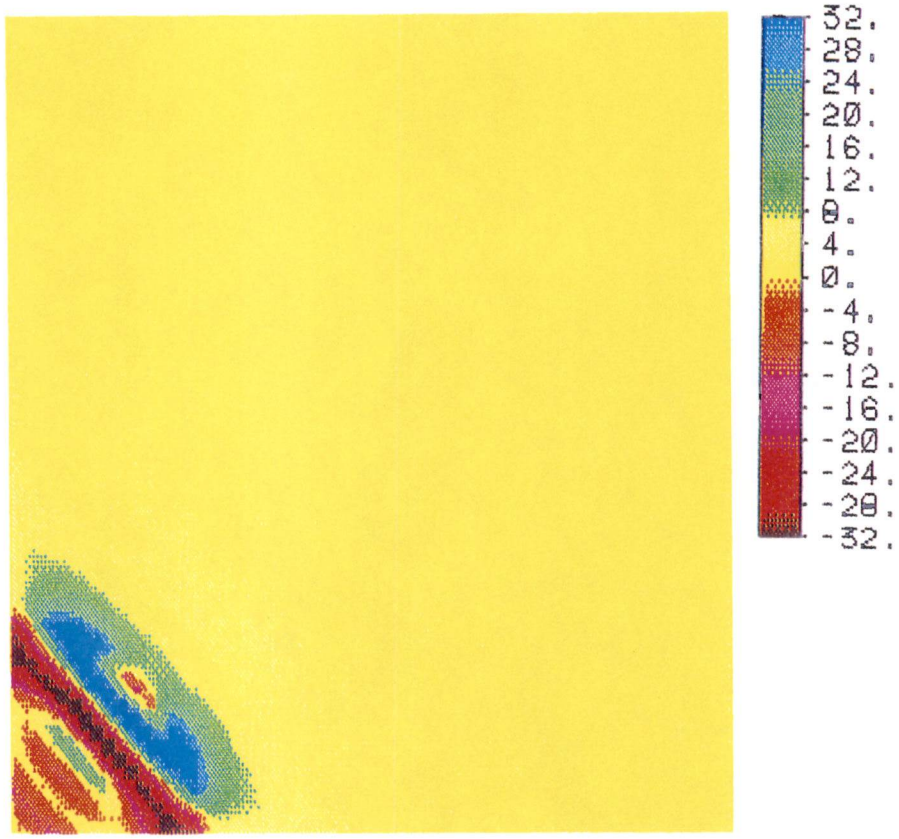

Figure 32: First quadrant of $\Re(\mathcal{F}\{G\})$ for circle with interior propagation velocity 200% of exterior, $\kappa_0 = 0.5 - 0.03j$

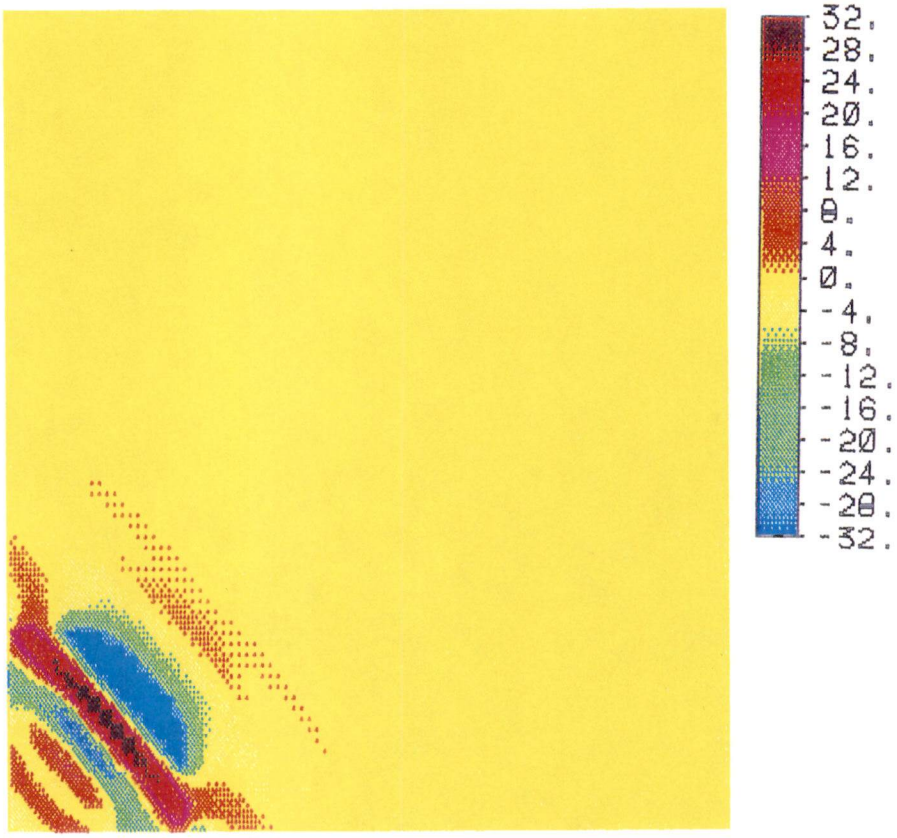

Figure 33: First quadrant of $\Im(\mathcal{F}\{G\})$ for circle with interior propagation velocity 200% of exterior, $\kappa_0 = 0.5 - 0.03j$

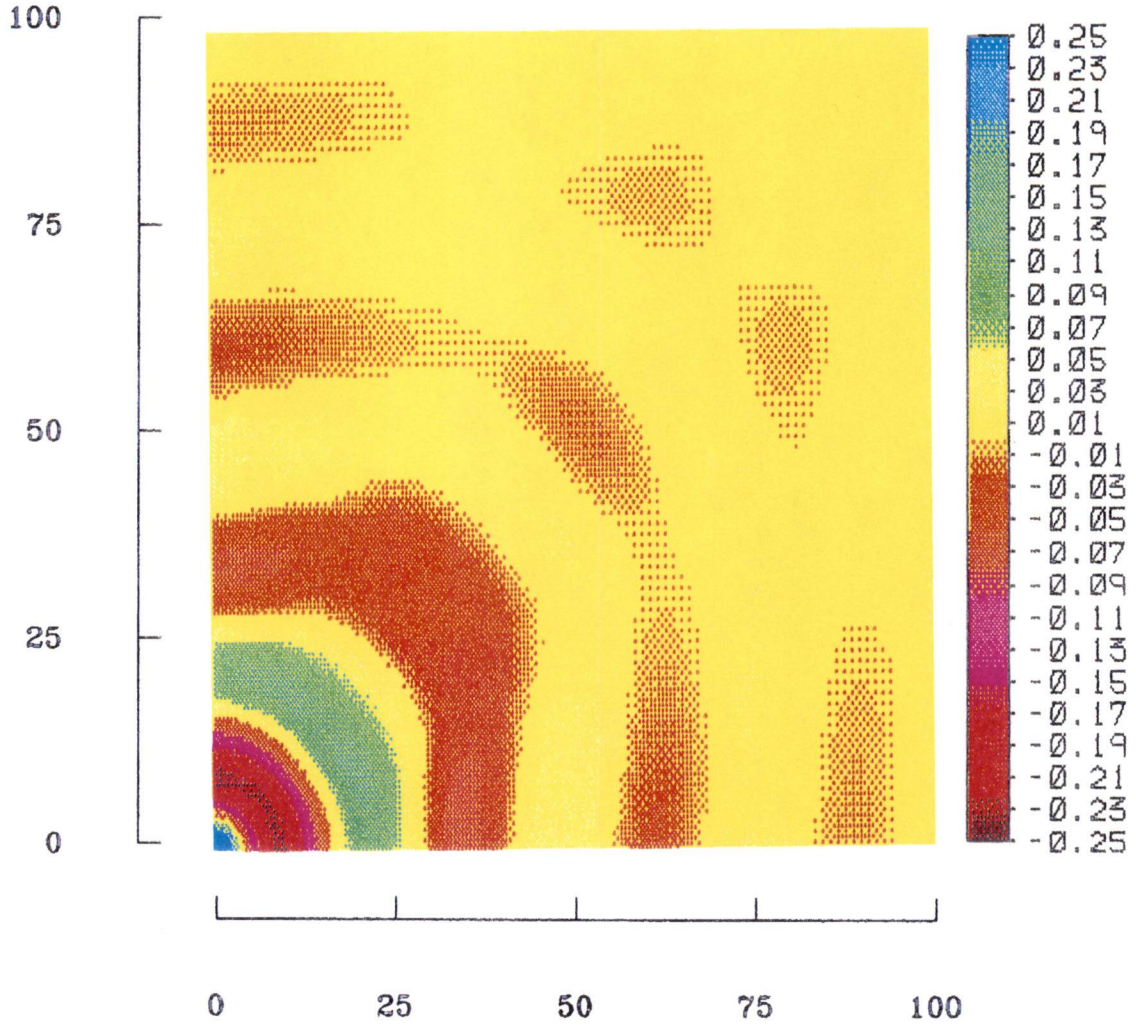

Figure 34: Diffraction of lower frequencies, $\kappa_0 = 0.25 - 0.03\jmath$, $\Re(G)$ through circle with interior propagation velocity 200% of exterior

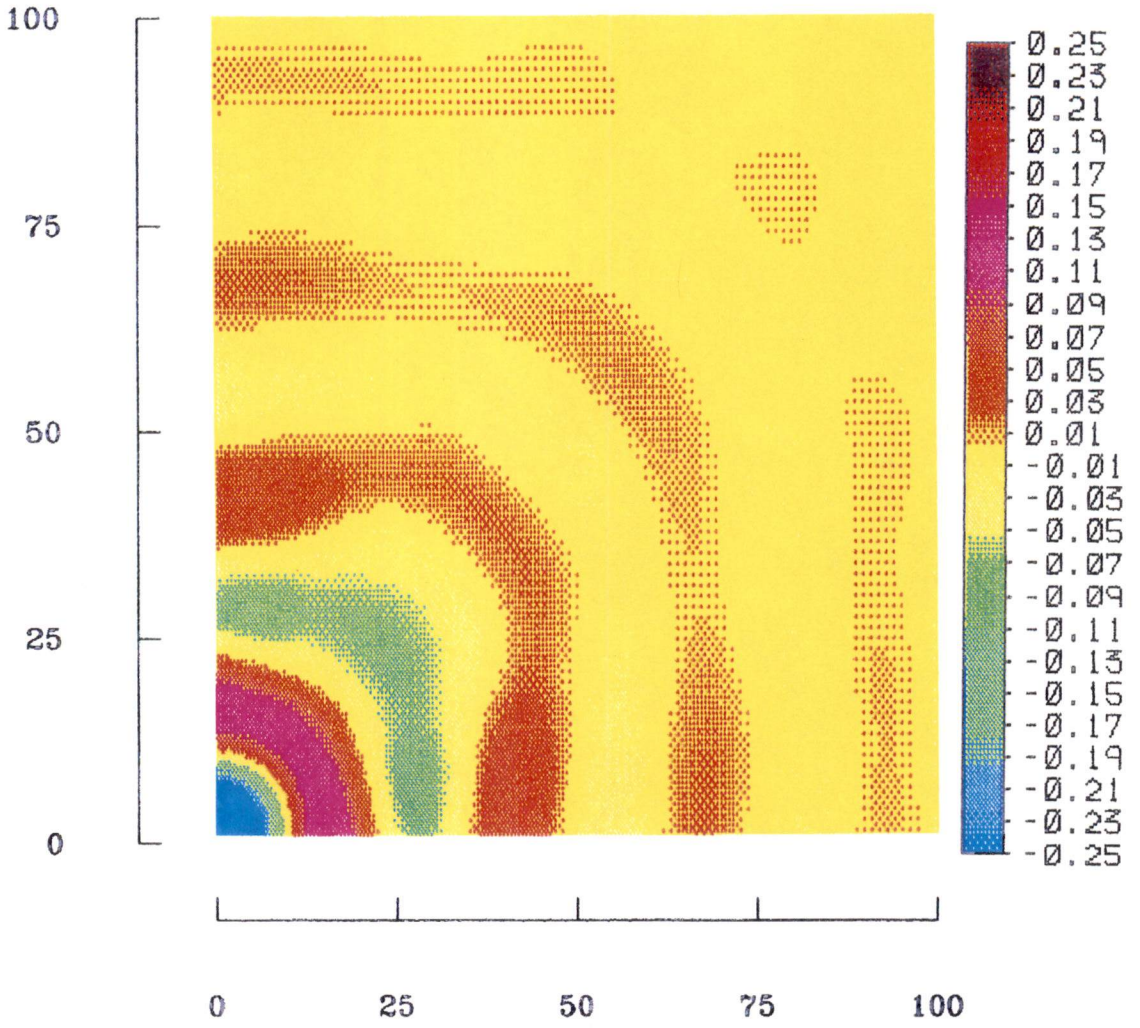

Figure 35: Diffraction of lower frequencies, $\kappa_0 = 0.25 - 0.03\jmath$, $\Im(G)$ through circle with interior propagation velocity 200% of exterior

WAVES IN LAYERED MEDIA

The variation of media wave speed $\alpha(x, z)$ for an example of layered media is depicted Figure 36. The middle layer, shown in brown, has a thickness of 50 distance units and $\alpha = 0.5$. The exterior layers are shown in blue and have $\alpha = -0.5$. This corresponds to the interior layer having a wave propagation speed 57.7% of the exterior media. Only the first quadrant of the 128 by 128 point grid is shown in Figure 36. Since the point source will be located at the origin, the solutions of the IDDM will be symmetric and first quadrant displays will show all the results.

Figures 37 and 38 display the results of 30 iterations of the IDDM for a point source at the origin in the layered medium of Figure 36. These results are for $\kappa_0 = 0.5 - 0.055j$. Both real, Figure 37, and imaginary, Figure 38, parts of the computed Green's function show the penetration of the waves into the higher speed exterior media and the corresponding increase in wavelength. Some interference effects near the media interfaces are also visible.

Moving up in frequency to $\kappa_R = 0.7$ when $\kappa_0 = 0.7 - 0.07j$, Figures 39 and 40 illustrate the IDDM computed Green's function at this higher frequency also using 30 iterations. Although significant wave energy continues to escape into the higher speed exterior media, the lower speed interior layer is beginning to guide the waves down its length. Note the planar wavefronts of the guided waves and the clear interference effects near the media interfaces. Also note that despite the high "damping factor", $\kappa_I = -0.07$, used, the guided wave attenuation is still relatively slight. This causes not totally insignificant wave energy to propagate across a wrap boundary resulting in increased computational errors. Experience with the IDDM suggests that most of the "splotches" in the upper

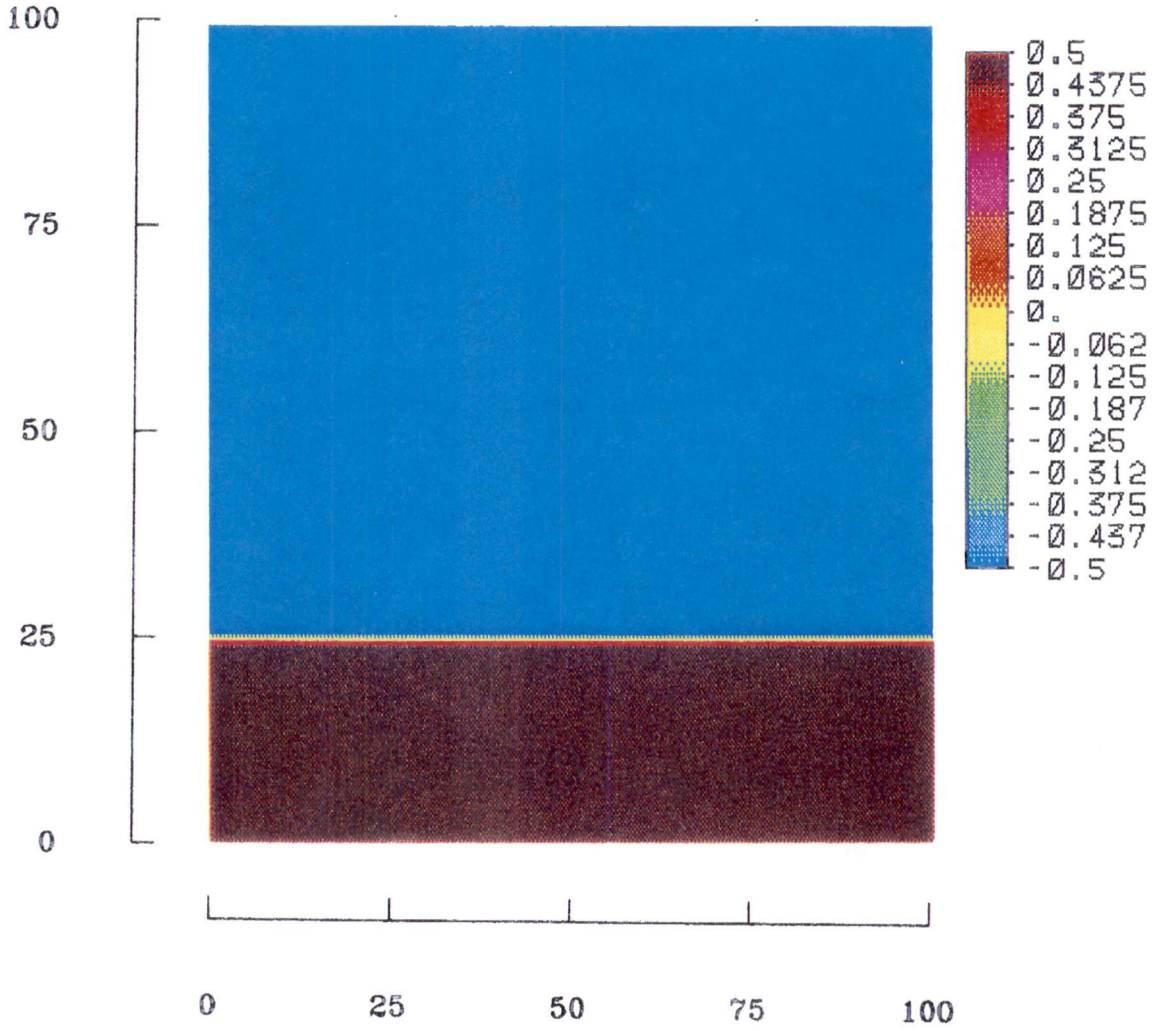

Figure 36: One-dimensional variation in media, middle layer (interior) has propagation velocity 57.7% of exterior

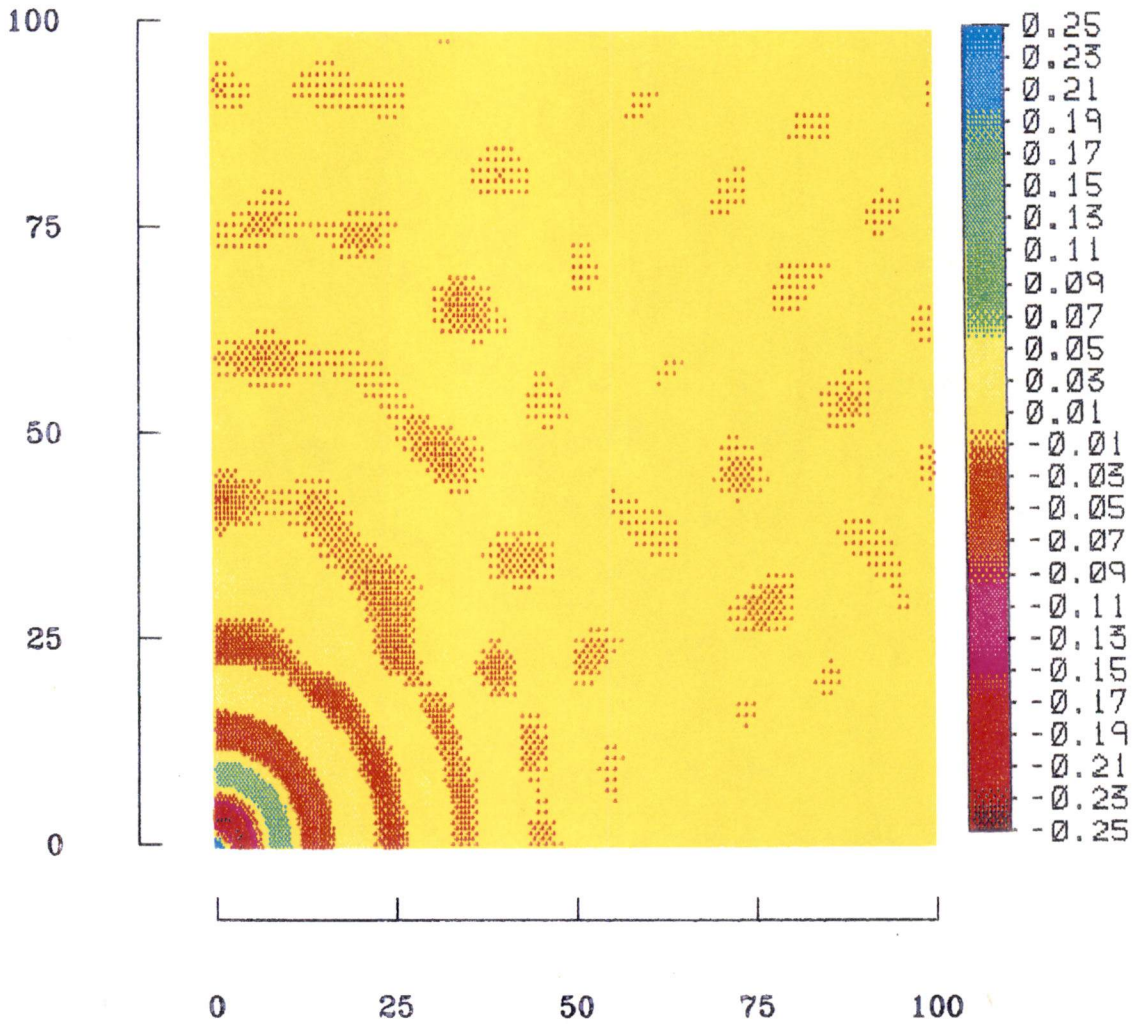

Figure 37: Wavelength of $\Re(G)$ increases in higher speed exterior media, $\kappa_0 = 0.5 - 0.055j$

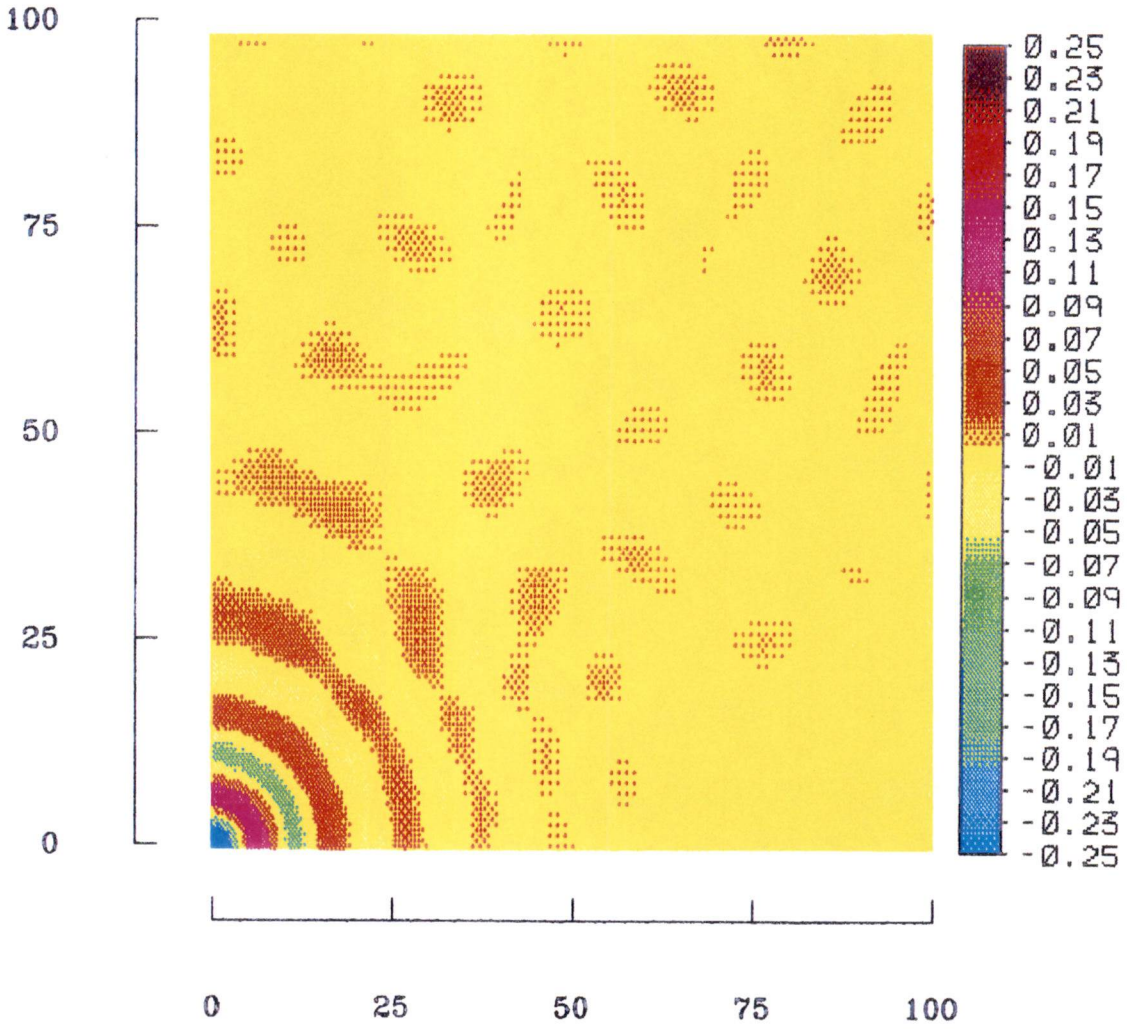

Figure 38: Wavelength of $\Im(G)$ increases in higher speed exterior media, $\kappa_0 = 0.5 - 0.055j$

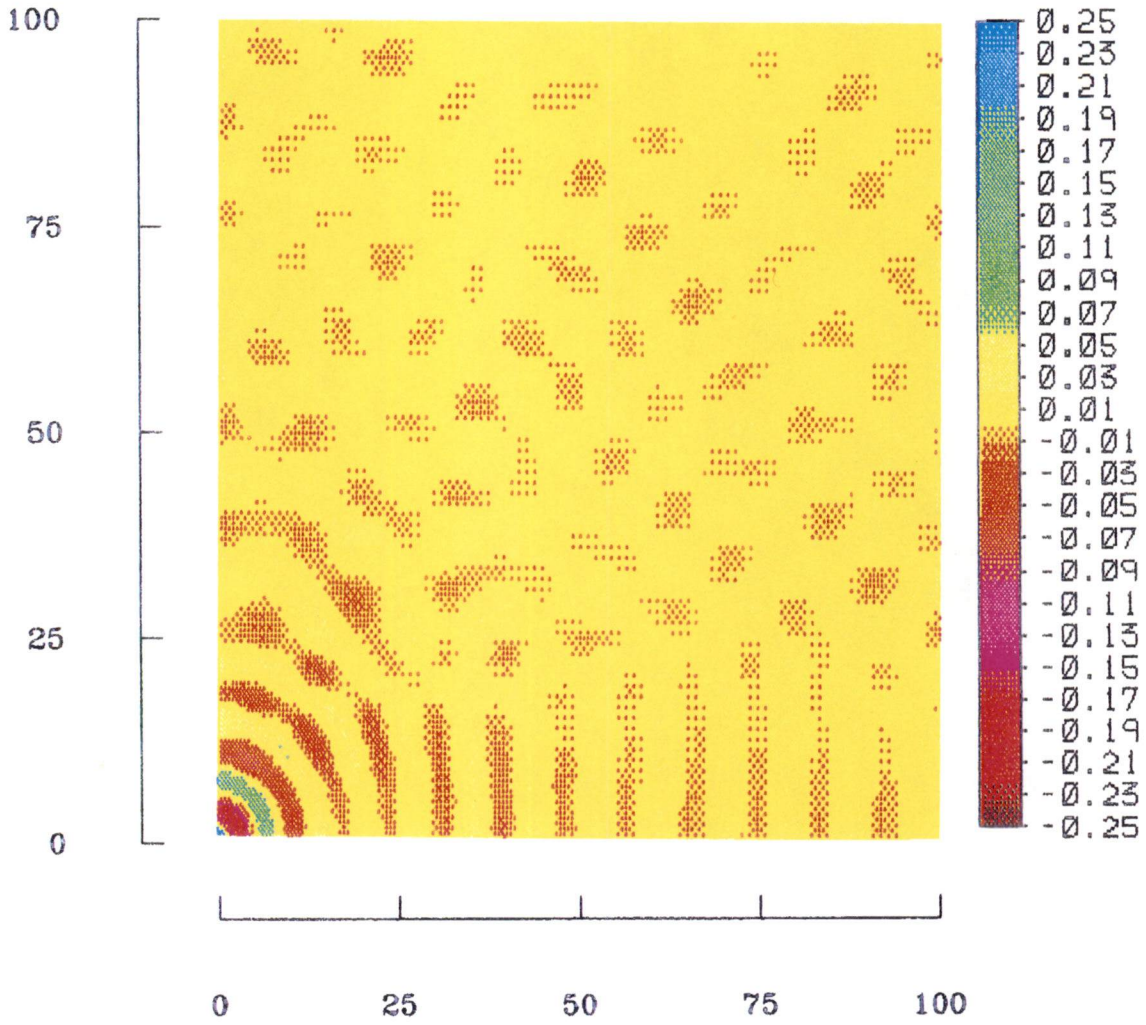

Figure 39: Slower speed interior layer begins to act as a (leaky) waveguide for $\Re(G)$ at $\kappa_0 = 0.7 - 0.07i$

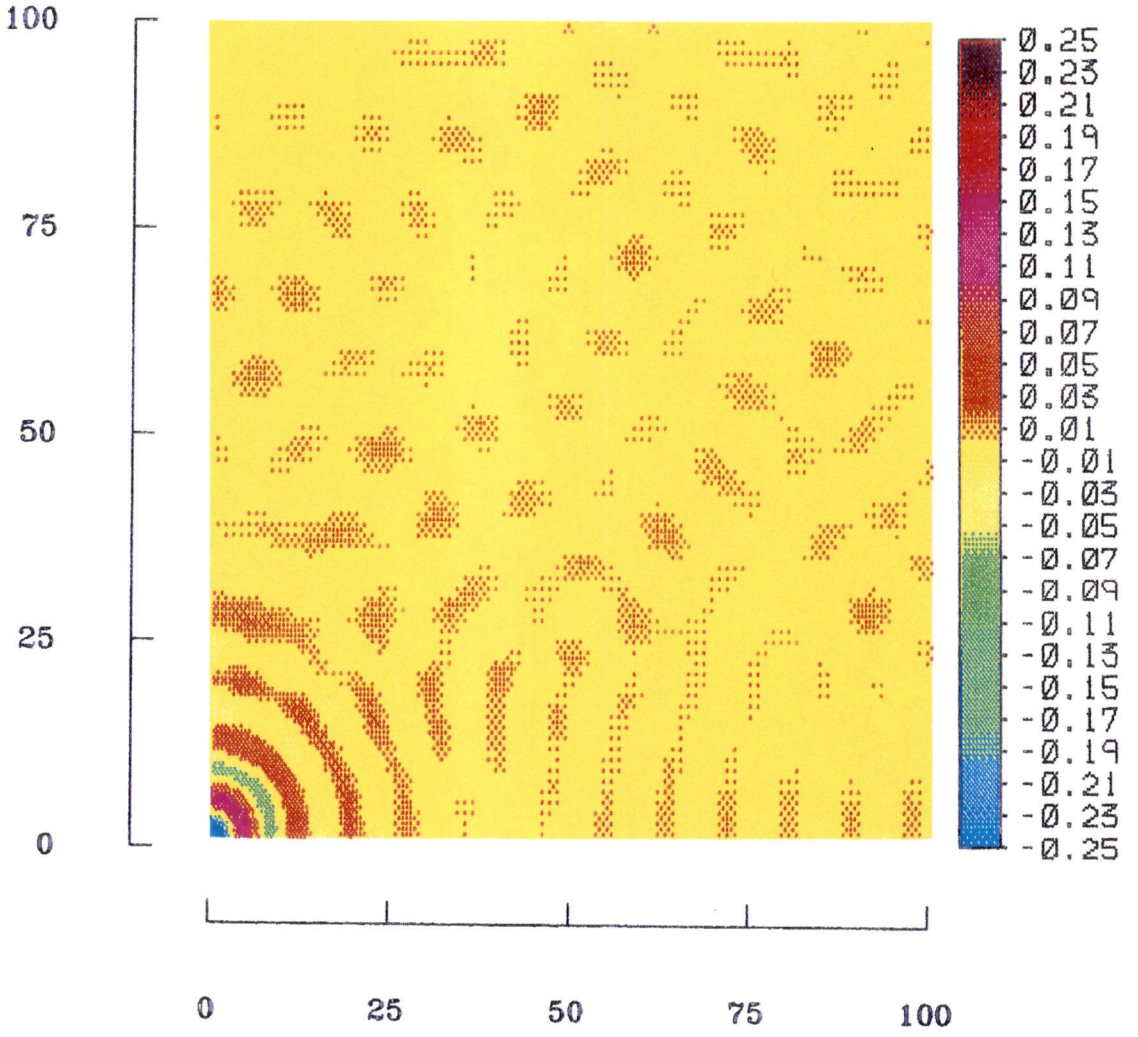

Figure 40: Slower speed interior layer begins to act as a (leaky) waveguide for $\Im(G)$ at $\kappa_0 = 0.7 - 0.07j$

right-hand corners of Figures 39 and 40 are actually noise predominantly due to this source of error.

Finally, moving up in frequency to $\kappa_R = 0.9$ with $\kappa_0 = 0.9 - 0.085j$ results in the real and imaginary parts of the Green's function shown in Figures 41 and 42, respectively. Here the waves are almost entirely trapped inside the slower speed layer. Both the real and imaginary parts show the formation of planar guided waves and pronounced interference patterns near the point source. More so than in the previous example, Figure 39 and 40, significant wave energy crosses a wrap boundary, even with $\kappa_I = -0.085$, causing increased error. The computation of practical waveguide problems with the IDDM will require the use of extended grids and spatial extents in the waveguide directions.

The Fourier transform of the results of Figures 41 and 42 are illustrated in part by Figures 43 and 44. Figure 41 depicts the real part of g_n. The imaginary part is shown as Figure 42. Note the high amplitude "ridges" near the right-hand sides of the main circular features in both Figures 43 and 44. As in the scattering example, the orientation of these ridges in Ω_x, Ω_z space is perpendicular to the axis of high amplitude wave propagation in untransformed x, z space. There are also horizontal striations in Figures 43 and 44. These are most likely due to the (vertically) planar wavefronts in untransformed space, Figures 41 and 42. Further examining Figures 43 and 44, and also magnifying regions on the original computer displays, one notices complicated regions that seem self-similar [116] or fractal in appearance. Although the interpretation of the transformed iterates, g's, of the IDDM is by no means clear at this early stage of development, much information leading to physical insight is probably locked up within them.

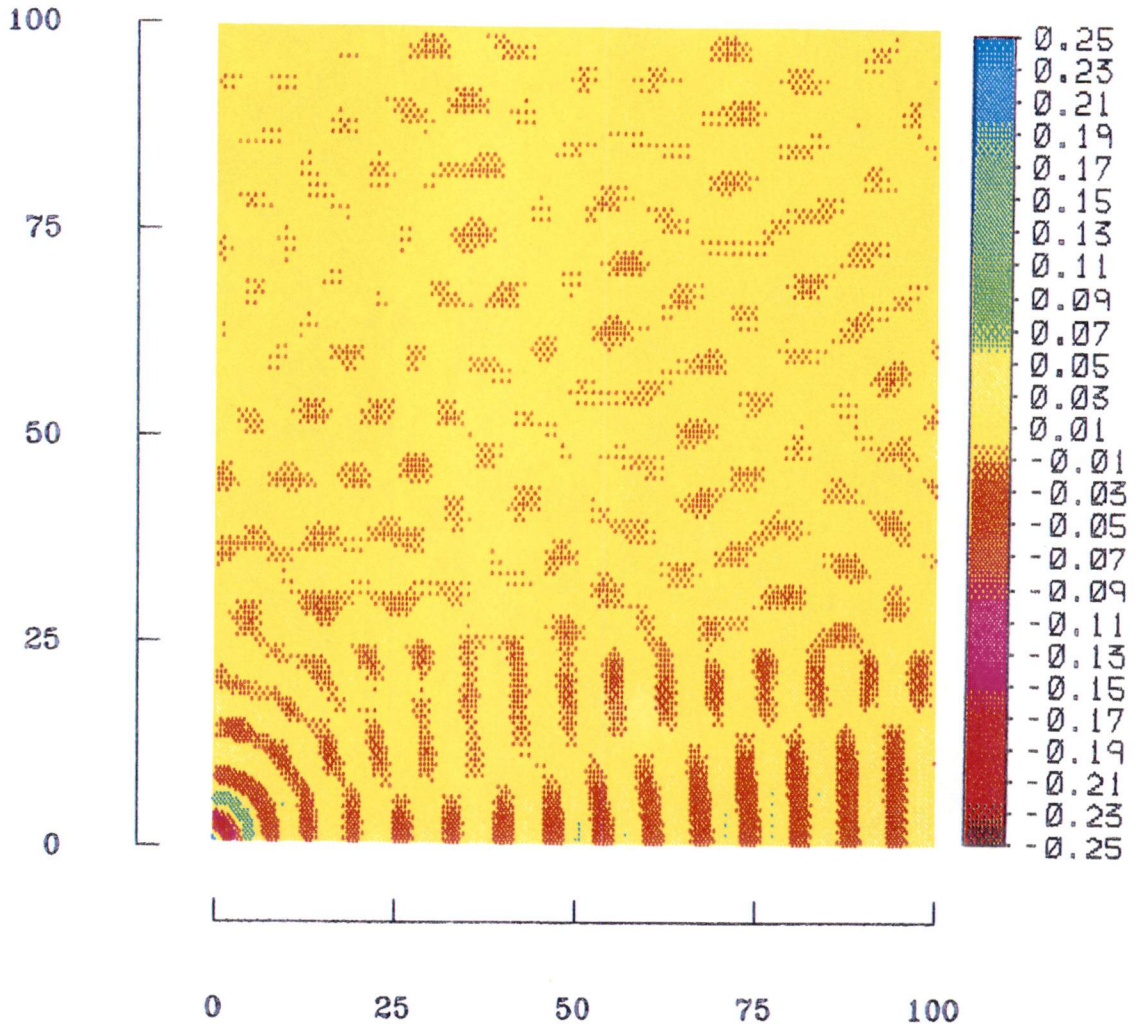

Figure 41: Guided mode behavior of $\Re(G)$ in slow speed layer at $\kappa_0 = 0.9 - 0.085j$

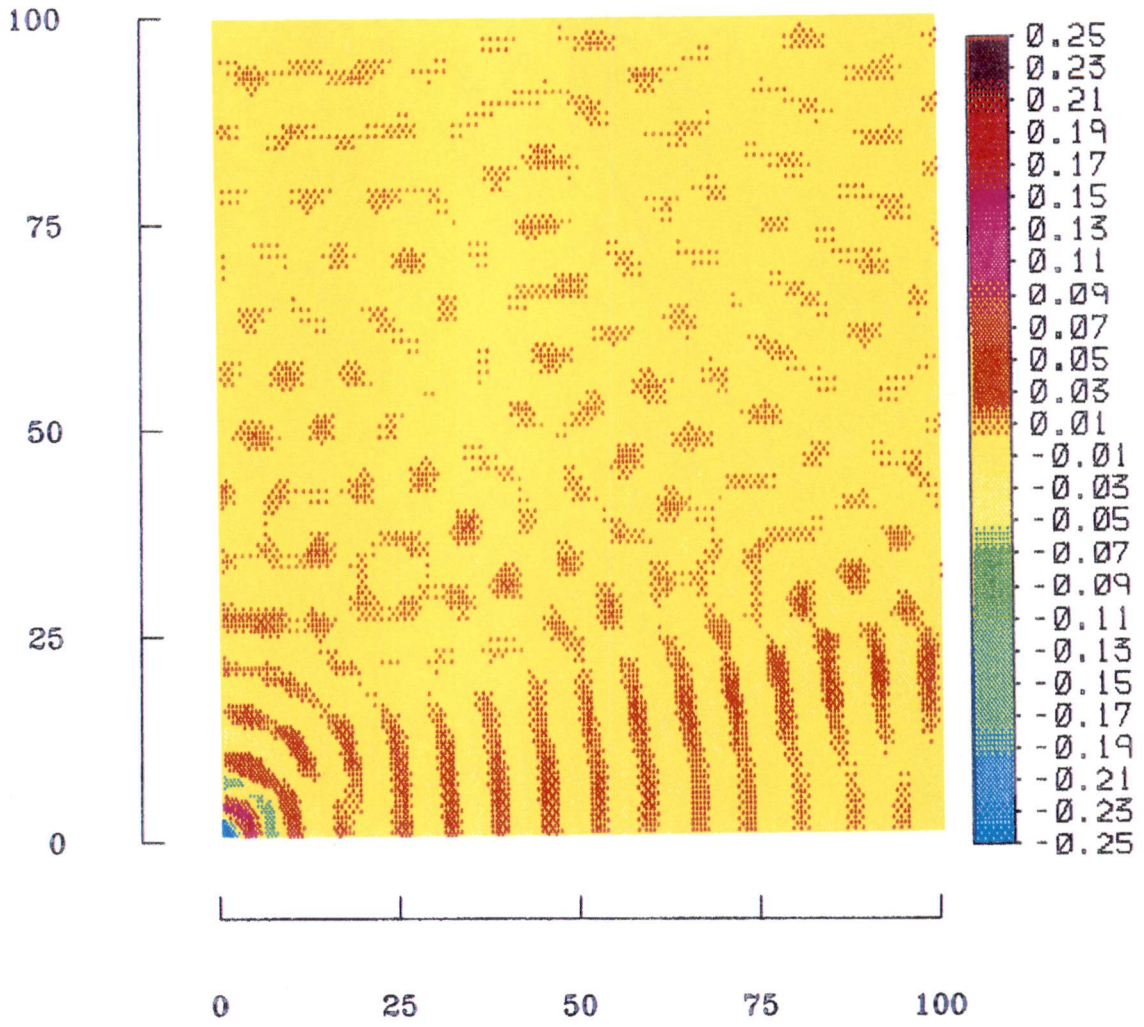

Figure 42: Guided mode behavior of $\Im(G)$ in slow speed layer at $\kappa_0 = 0.9 - 0.085j$

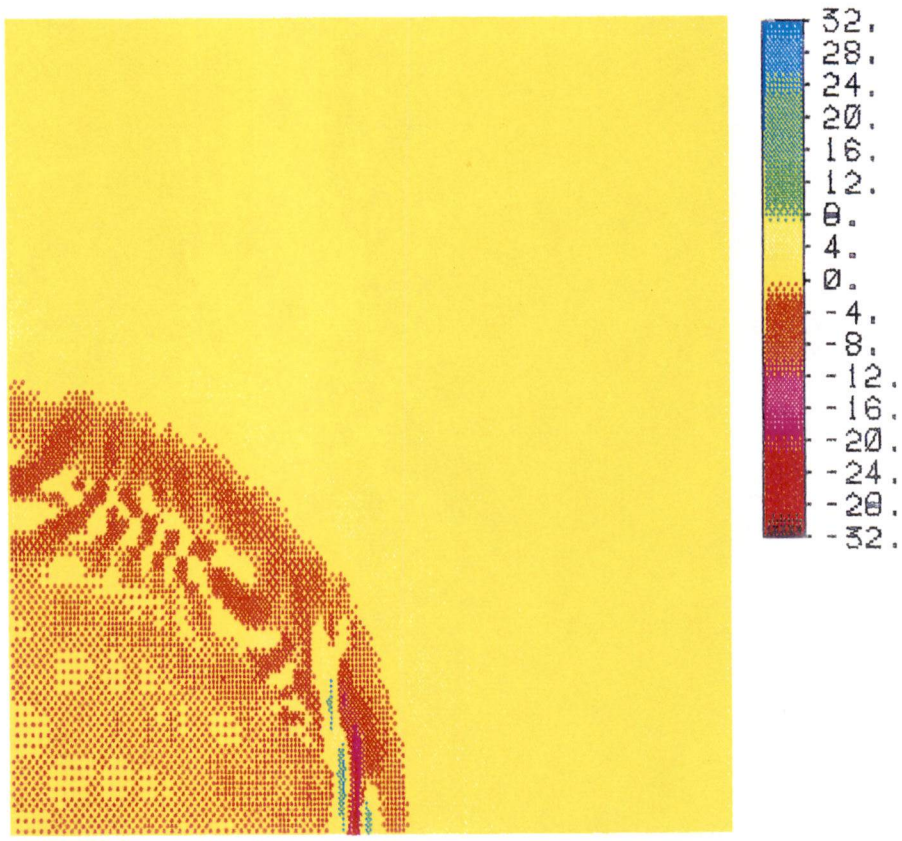

Figure 43: First quadrant of $\Re(\mathcal{F}\{G\})$ for layered media case with $\kappa_0 = 0.9 - 0.085j$

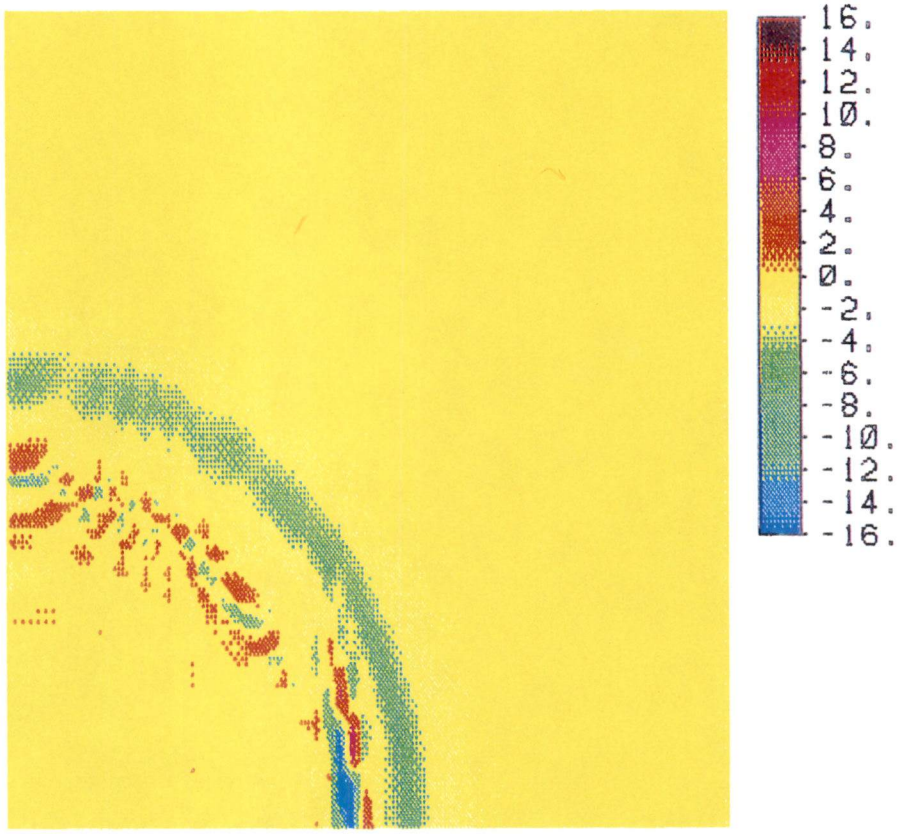

Figure 44: First quadrant of $\Im(\mathcal{F}\{G\})$ for layered media case with $\kappa_0 = 0.9 - 0.085j$

CHAPTER 4

INHOMOGENEOUS MEDIA GREEN'S FUNCTIONS AND THE BOUNDARY ELEMENT METHOD

BACKGROUND

Examining the Chapter 1 derivations of the governing relations of the boundary element method for the Helmholtz equation, (20) for the HIEF and (21) for the CHIEF methods, the reader will observe that although the Green's function values between points must be known, there is no requirement that the Green's function must be for homogeneous media. The derivations of Chapter 1 work just as well for the inhomogeneous media Helmholtz equation (59). Thus, the Green's function values for the Helmholtz equation in a medium with a particular variation of wave propagation speed computed via finite elements or finite differences, for example, could be used in a boundary element method. Practically, of course, this would be senseless, since the original problem could have been solved in the first place by one of these methods with little or no extra work. However, for specialized geometries where certain simplifications hold, computing the Green's functions via some auxiliary method can be eminently practical.

One auxiliary method for computing Green's function values for the inhomogeneous media Helmholtz equation that has been the subject of significant research is the scattering matrix method. The combination of this, together with the boundary element method, has been described by G. T. Schuster and L. C. Smith [117] and in the series of papers by T. W. Dawson [118,119]. Likewise, when the approximations inherent in various other methods are acceptable, i.e. ray theoretical methods [91,95], parabolic equation methods [95,120], and

coupled mode methods [95,121], then they can be used. The object of this chapter is to outline where the Iterative Dual Domain Method (IDDM) can provide an effective and efficient approach.

INHOMOGENEOUS MEDIA WITH A STRONG INFLUENCE ON A BODY'S NEARFIELD RADIATION

Figure 45 shows an example where the inhomogeneities of the medium may be expected to exert a strong influence on the nearfield wave radiation from the body. This particular example is drawn from geophysical acoustics and depicts a borehole acoustic source used in well-logging and vertical seismic profiling. The acoustic source is embedded in the inhomogeneous media with perhaps strong wave propagation velocity contrasts occurring along the body's length. Further, the salt dome flank to the right of the diagram represents a strong reflector that could send much of the energy radiated from the body back to it.

This is an example where nearly all simplified methods, i.e. ray theoretical and range invariant methods, will not work. Candidate methods traditionally include finite elements and finite differences. A possible alternative is to use the IDDM to calculate the Green's functions needed for a boundary element method. The calculation of these Green's functions would have to be done on a grid covering the spatial extent of the inhomogeneous media that significantly influenced the body's nearfield radiation. Also, for a body divided up into M elements, M such grids of Green's functions would have to be found. After order M^3 computations solving the matrix system, the boundary element method will then have solved for the potential values on the body's boundary. Calculation of N field points using a BEM would further require finding NM Green's functions each on a substantial grid.

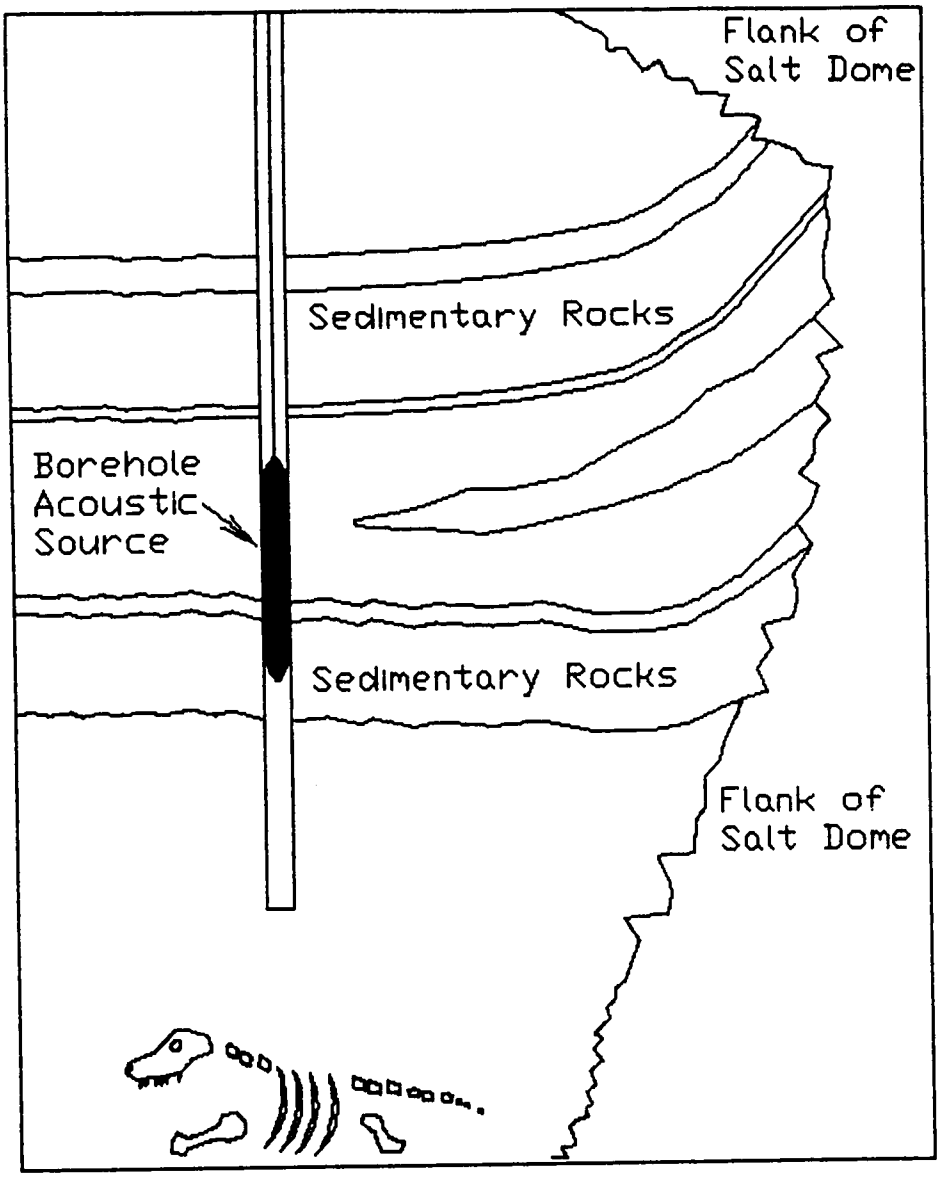

Figure 45: Borehole acoustic source example.

Reconsidering this approach, one realizes that the field points could be calculated directly from the boundary potentials using the IDDM, thus avoiding the work of the second stage BEM computations. One almost immediately further realizes that the whole boundary element computation is itself superfluous in this case. Whenever the calculation of the Green's functions for the radiating body's boundary elements would require large spatial extents at high resolution, it pays to recast the problem so it can be solved by the IDDM directly. In other words, instead of considering the body as a surface with an array of sources and panels of impedance values, the body would be treated as an equivalent region of inhomogeneous media and source points. This is not to say the two different solution approaches require the same or equivalent information in the mathematical sense. However, for most practical engineering problems, enough information is known about the geometries, materials, and so forth, that either BEM or IDDM may be used.

Finite elements, finite differences, and the Iterative Dual Domain Method all can be used to solve the Helmholtz equation in a medium with spatial variation in wave propagation speed. Although the IDDM might be perhaps somewhat trickier to deal with at the edges of the computational domain, it has one great advantage: speed. Both finite element and finite difference methods require computational effort of order N^3, where N is the number of field points calculated. Of course, most often finite element and finite difference method formulations lead to the solution of banded matrix systems, as opposed to full ones, so the computational effort is much reduced for many problems. In other words, a "small" bandwidth matrix system results in a "small" constant in front of the N^3 in the operation count. It should also be observed that at present (1992) some lesser known sophisticated matrix solvers exist of order less than N^3 (but

greater than N^2). They have not yet, however found widespread application in finite element and finite difference codes. Letting I represent the number of iterations required, the iterative dual domain method is of order $IN \log_2 N$. Typically $30 < I < 50$, so effectively the IDDM is of order $N \log_2 N$.

The computational costs in terms of arithmetic operations and memory storage requirements of the finite element method for the solution of wave propagation problems in inhomogeneous media are discussed in detail in references [28,90,115]. References [35,90] address the costs of finite difference methods on similar problems. The particular implementation of the IDDM used for this dissertation employed multidimensional FFT and IFFT algorithms based on the Danielson-Lanczos FFT formula. Any good FFT algorithm could have been used with roughly equivalent results. Detailed FFT descriptions can be found in references [34,35,51,63–70,75,76], among others.

INHOMOGENEOUS MEDIA WITH A WEAK INFLUENCE ON A BODY'S NEARFIELD RADIATION

Many, if not most, inhomogeneous media wave propagation problems occur in a setting where the influence of the spatial variation of the media's wave propagation speed on the nearfield emission from a radiating body is small. Such a common situation is illustrated in Figure 46. The example of Figure 46 is drawn from underwater acoustics and depicts a sidescan sonar as used in subbottom profiling and geophysical site surveys. The acoustic source is typically located on the bottom of the sidescan sonar towbody. The acoustic medium around the towbody is nearly uniform for some distance. Beyond this distance, the acoustic environment has considerable variation in wave propagation speed.

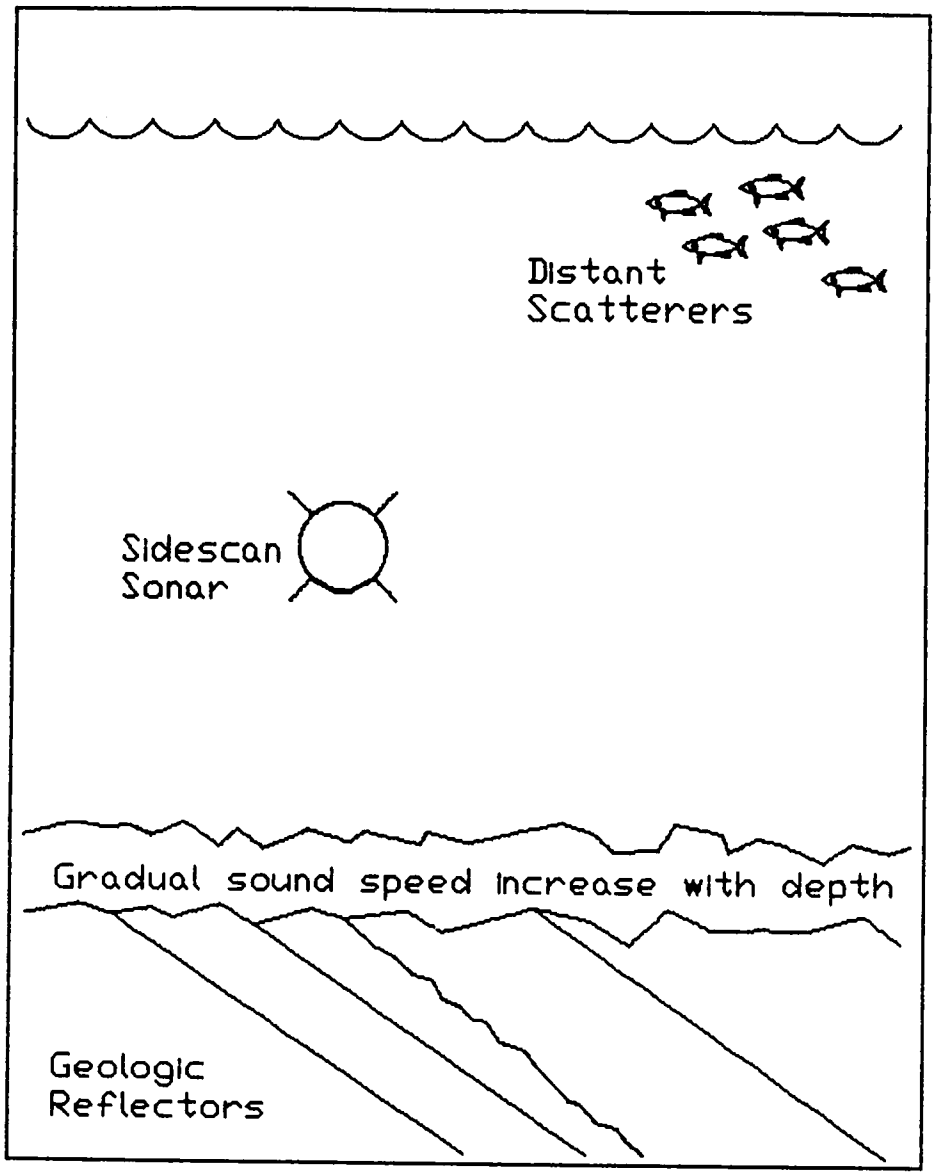

Figure 46: Sidescan sonar example.

Ocean bottom sediments, geologic formations, and assorted distant scatterers, all contribute to the far field radiation pattern.

Unlike the example of the previous section, this kind of problem is amenable to a hybrid boundary element method and Iterative Dual Domain Method approach. Taking the transducer source strengths and the acoustic impedances of the surfaces of the towbody as known, the acoustic field could be computed using a hybrid BEM and IDDM approach. Since the inhomogeneities of the media are assumed not to significantly influence the nearfield of the body, the equivalent acoustic source strengths on the surfaces of the towbody could be found using a conventional homogeneous media boundary element method. This configuration of source strengths on, say, M boundary elements comprising the towbody could then be used as the source term in the IDDM to compute the acoustic field in the inhomogeneous media. Alternatively, if one wanted to examine the effects of the individual boundary elements on the far field radiation pattern, one could compute the Green's function for each boundary element source, weigh each result, and sum, since the principle of superposition holds.

The hybrid boundary element method with the IDDM is of order M^3 to solve for the boundary element source strengths and then of order $N\log_2 N$ to solve for the field points. If the influence of each boundary element is examined separately and then a total solution found, the field point computation would require on the order of $MN\log_2 N$ operations, only slightly more work than the order MN field point calculations in conventional homogeneous media boundary element methods.

HIGHER DIMENSIONS

Although the examples in this dissertation were all two-dimensional, the derivations of the boundary element method and the development of the IDDM are completely general with respect to the dimensions. The methods described should work equally well in three-dimensions (or higher) as in two-dimensions. The actual coding and implementation becomes more difficult as the number of dimensions increases. This is due to much larger memory and storage requirements, more complicated indexing, and (of course) substantially more difficult display and visualization of input data and results. The data organization with respect to wrap around ordering in the IDDM can become particularly tricky in higher dimensions. Despite these difficulties, which are characteristic of many numerical methods with increasing dimension, the Iterative Dual Domain Method allows the solution of wave propagation problems, previously only within reach of the largest supercomputers, on modest computer workstations.

SUMMARY

A boundary element method for the numerical solution of the exterior Helmholtz problem was specified. Its accuracy and convergence characteristics were examined. Boundary element methods have been restricted to applications where the Green's functions were known. For general inhomogeneous media, the Green's function must be found by some other means in order to use BEM.

The Iterative Dual Domain Method developed in Chapters 2 and 3 provides a very powerful means of computing Green's functions in an inhomogeneous media. The IDDM requires of order $N\log_2 N$ computations compared to of order N^3 for other well-known and popular methods. The Green's functions found by

the IDDM can be used in a BEM, or alternatively for many engineering problems the IDDM can be used to solve the problem in its entirety.

LIST OF REFERENCES

LIST OF REFERENCES

1. H. HELMHOLTZ 1859 *Journal für die Reine und Angewandte Mathematik* **57**, 1–72. Theorie der Luftschwingungen in Röhren mit offenen Enden.

2. LORD RAYLEIGH 1896 *Theory of Sound* (two volumes), vol. 2 143–147. Articles 293 and 294. New York: Dover Publications, second revised and enlarged edition, 1945 re-issue.

3. H. LAMB 1932 *Hydrodynamics*, 496–502. Articles 289–291. New York: Dover Publications, sixth edition, 1945 re-issue.

4. R. LEIS 1958 *Archive for Rational Mechanics and Analysis* **2**, 101–113. Über das Neumannsche Randwertproblem für die Helmholtzsche Schwingungsgleichung.

5. L. H. CHEN AND D. G. SCHWEIKART 1963 *Journal of the Acoustical Society of America* **35**, 1626–1632. Sound radiation from an arbitrary body.

6. G. CHERTOCK 1964 *Journal of the Acoustical Society of America* **36**, 1305–1313. Sound radiation from vibrating surfaces.

7. G. B. BRUNDRIT 1965 *Quarterly Journal of Mechanics and Applied Mathematics* **18**, 473–489. A solution to the problem of scalar scattering from a smooth bounded obstacle using integral equations.

8. L. G. COPLEY 1967 *Journal of the Acoustical Society of America* **41**, 807–816. Integral equation method for radiation from vibrating bodies.

9. H. A. SCHENCK 1967 *Journal of the Acoustical Society of America* **44**, 41–58. Improved integral formulation for acoustic radiation problems.

10. A. F. SEYBERT, B. SOENARKO, F. J. RIZZO, AND D. J. SHIPPY 1984 *ASME Journal of Vibration, Acoustics, Stress, and Reliability in Design* **106**, 414–420. Application of the BIE method to sound radiation problems using an isoparametric element.

11. A. F. SEYBERT, B. SOENARKO, F. J. RIZZO, AND D. J. SHIPPY 1985 *Journal of the Acoustical Society of America* **77**, 362–368. An advanced computational method for radiation and scattering of acoustic waves in three dimensions.

12. A. F. SEYBERT, B. SOENARKO, F. J. RIZZO AND D. J. SHIPPY 1986 *Journal of the Acoustical Society of America* **80**, 1241–1247. A special integral equation formulation for acoustic radiation and scattering for axisymmetric bodies and boundary conditions.

13. A. F. SEYBERT AND C. Y. R. CHENG 1987 *ASME Journal of Vibration, Acoustics, Stress, and Reliability in Design* **109**, 15–21. Application of the boundary element method to acoustic cavity response and muffler analysis.

14. A. F. SEYBERT AND T. K. RENGARAJAN 1987 *Journal of the Acoustical Society of America* **81**, 1299–1306. The use of CHIEF to obtain unique solutions for acoustic radiation using boundary integral equations.

15. A. F. SEYBERT AND T. K. RENGARAJAN 1987 *ASME Journal of Vibration, Acoustics, Stress, and Reliability in Design* **109**, 381–387. The high-frequency radiation of sound from bodies of arbitrary shape.

16. A. F. SEYBERT, T. W. WU AND X. F. WU 1988 *Journal of the Acoustical Society of America* **84**, 1906–1912. Radiation and scattering of acoustic waves from elastic solids and shells using the boundary element method.

17. A. F. SEYBERT AND T. W. WU 1989 *Journal of the Acoustical Society of America* **85**, 19–23. Modified Helmholtz integral equation for bodies sitting on an infinite plane.

18. A. F. SEYBERT AND T. W. WU 1991 *Fundamentals and Applications of the BEM and FEM in Acoustics and Noise Control*, 72–75. Lexington: University of Kentucky.

19. A. F. BURTON AND G. F. MILLER 1971 *Proceedings of the Royal Society of London Series A* **323**, 201–210. The application of integral equation methods to the numerical solution of some exterior boundary-value problems.

20. A. J. BURTON 1973 NPL Report NAC 30, National Physical Laboratory, Division of Numerical Analysis and Computing, Teddington, Middlesex. The Solution of Helmholtz' Equation in Exterior Domains Using Integral Equations.

21. W. L. MEYER, W. A. BELL, B. T. ZINN AND M. P. STALLYBRASS 1978 *Journal of Sound and Vibration* **59**, 245–262. Boundary integral solutions of three dimensional acoustic radiation problems.

22. W. L. MEYER, W. A. BELL, M. P. STALLYBRASS AND B. T. ZINN 1979 *Journal of the Acoustical Society of America* **65**, 631–638. Prediction of the sound field radiated from axisymmetric surfaces.

23. W. TOBOCMAN 1984 *Journal of the Acoustical Society of America* **76**, 599–607. Calculation of acoustic wave scattering by means of the Helmholtz integral equation.

24. W. TOBOCMAN 1987 *Journal of the Acoustical Society of America* **80**, 1828–1837. Extension of the Helmholtz integral equation method to shorter wavelengths.

25. T. TERAI 1980 *Journal of Sound and Vibration* **69**, 71–100. On calculation of sound fields around three dimensional objects by integral equation methods.

26. Z. REUT 1985 *Journal of Sound and Vibration* **103**, 297–298. On the boundary integral methods for the exterior acoustic radiation problem.

27. K. A. CUNEFARE, G. KOOPMANN AND K. BROD 1989 *Journal of the American Acoustical Society of America* **85**, 39–48. A boundary element method for acoustic radiation valid for all wavenumbers.

28. I. HARARI AND T. J. R. HUGHES 1992 *Computer Methods in Applied Mechanics and Engineering* **97**, 77–102. A cost comparison of boundary element and finite element methods for problems of time-harmonic acoustics.

29. I. HARARI AND T. J. R. HUGHES 1992 *Computer Methods in Applied Mechanics and Engineering* **97**, 103–124. Analysis of continuous formulations underlying the computation of time-harmonic acoustics in exterior domains.

30. C. A. BREBBIA AND S. WALKER 1980 *Boundary Element Techniques in Engineering*. London: Newnes-Butterworths.

31. R. E. KLEINMAN AND G. F. ROACH 1974 *SIAM Review*, **16**, 214–236. Boundary integral equations for the three-dimensional Helmholtz equation.

32. A. P. DOWLING AND J. E. FFOWCS WILLIAMS 1989 *Sound and Sources of Sound*. Chichester: Ellis Horwood Ltd.

33. G. BARTON 1989 *Elements of Green's Functions and Propagation*. Oxford: Clarendon Press.

34. W. PRESS, B. FLANNERY, S. TEUKOLSKY, AND W. VETTERLING 1986 *Numerical Recipes, The Art of Scientific Computing*. Cambridge: Cambridge University Press.

35. D. KAHANER, C. MOLER, AND S. NASH 1989 *Numerical Methods and Software*, 155–160. Englewood Cliffs: Prentice Hall.

36. G. W. STEWART 1973 *Introduction to Matrix Computations*. London: Academic Press.

37. J. J. DONGARRA, C. B. MOLER, J. R. BUNCH, AND G. W. STEWART 1979 *LINPACK User's Guide*, 11.1–11.23. Philadelphia: SIAM.

38. M. WEAVER 1991 in *U.S. Air Force Summer Research Program Reports*, 31-1–31-27. Boundary element acoustic analysis of the exhaust gas management system in the AEDC aeropropulsion systems test facility. Washington, D.C.: Air Force Office of Scientific Research.

39. R. A. MARSCHALL 1992 in *U.S. Air Force Summer Research Program Reports*, 4-1–4-20. CAD and acoustic BEM applied to the modelling of the AEDC ASTF EGMS. Washington, D.C.: Air Force Office of Scientific Research.

40. R. COURANT AND D. HILBERT 1924 *Methoden Der Mathematischen Physik* Berlin: Verlang von Julius Springer.

41. A. N. TIKHONOV AND A. A. SAMARSKII 1963 *Equations of Mathematical Physics*. New York: Dover Publications, 1990 re-issue.

42. S. L. SOBOLEV 1964 *Partial Differential Equations of Mathematical Physics*, 265–324. Lectures 20–22. New York: Dover Publications, 1989 re-issue.

43. G. F. CARRIER AND C. E. PEARSON 1976 *Partial Differential Equations*. London: Academic Press.

44. I. STAKGOLD 1979 *Green's Functions and Boundary Value Problems*. Toronto: John Wiley and Sons.

45. E. ZAUDERER 1983 *Partial Differential Equations of Applied Mathematics*. New York: John Wiley and Sons.

46. A. H. ZEMANIAN 1965 *Distribution Theory and Transform Analysis*. New York: Dover Publications, 1987 re-issue.

47. A. H. ZEMANIAN 1987 *Generalized Integral Transformations*. New York: Dover Publications, corrected re-issue.

48. G. E. LATTA 1990 in *Handbook of Applied Mathematics, Selected Results and Methods* (Carl E. Pearson, editor), 571–630. New York: Van Nostrand Reinhold, second revised and extended edition. Transform methods.

49. J. ARSAC 1966 *Fourier Transforms and the Theory of Distributions*. Englewood Cliffs: Prentice-Hall.

50. Y. A. BRYCHKOV AND A. P. PRUDNIKOV 1989 *Integral Transforms of Generalized Functions*. London: Gordon and Breach Science Publishers.

51. R. N. BRACEWELL 1986 *The Fourier Transform and Its Applications*. St. Louis: McGraw-Hill Book Company, second revised and expanded edition.

52. A. PAPOULIS 1977 *Signal Analysis*. New York: McGraw-Hill Book Company.

53. G. N. WATSON 1922 *Bessel Functions*. Cambridge: University Press.

54. E. JAHNKE AND F. EMDE 1945 *Funktionentafeln mit Formeln und Kurven*. New York: Dover Publications, fourth corrected and expanded edition.

55. M. R. SPIEGEL 1968 *Mathematical Handbook of Formulas and Tables*. New York: McGraw-Hill Book Company.

56. I. N. SNEDDON 1951 *Fourier Transforms*. New York: McGraw-Hill Book Company.

57. B. DAVIES 1978 *Integral Transforms and Their Applications*. Heidelberg: Springer-Verlag.

58. P. M. DUFFIEUX 1983 *The Fourier Transform and Its Applications to Optics*. Toronto: John Wiley and Sons, second revised edition.

59. M. J. LIGHTHILL 1958 *Introduction to Fourier Analysis and Generalized Functions*. Cambridge: University Press.

60. L. SCHWARTZ 1966 *Mathematics for the Physical Sciences*. Paris: Hermann.

61. G. F. CARRIER, M. KROOK, AND C. E. PEARSON 1966 *Functions of a Complex Variable, Theory and Technique*, 336–337. St. Louis: McGraw-Hill Book Company.

62. A. G. SVESHNIKOV AND A. N. TIKHONOV 1973 *The Theory of Functions of a Complex Variable*, 279–281. Moscow: MIR Publishers, revised from the 1967 Russian edition.

63. D. E. DUDGEON AND R. M. MERSEREAU 1984 *Multidimensional Digital Signal Processing*. Englewood Cliffs: Prentice-Hall.

64. F. G. STREMLER 1977 *Introduction to Communication Systems*. Don Mills: Addison-Wesley Publishing Co.

65. A. V. OPPENHEIM AND R. W. SCHAFER 1975 *Digital Signal Processing*. Englewood Cliffs: Prentice-Hall.

66. A. V. OPPENHEIM AND R. W. SCHAFER 1989 *Discrete-Time Signal Processing*. Englewood Cliffs: Prentice-Hall.

67. J. S. WALKER 1991 *Fast Fourier Transforms*. Boca Raton: CRC Press.

68. R. C. GONZALEZ AND P. WINTZ 1977 *Digital Image Processing*. Don Mills: Addison-Wesley Publishing Company.

69. J. S. LIM 1988 in *Advanced Topics in Signal Processing* (Jae S. Lim and Alan V. Oppenheim, editors), 338–415. Englewood Cliffs: Prentice-Hall. Two-Dimensional Signal Processing.

70. C. S. BURRUS 1988 in *Advanced Topics in Signal Processing* (Jae S. Lim and Alan V. Oppenheim, editors), 338–415. Englewood Cliffs: Prentice-Hall. Efficient Fourier transform and convolution algorithms.

71. V. I. KRYLOV AND N. S. SKOBLYA 1977 *A Handbook of Methods of Approximate Fourier Transformation and Inversion of the Laplace Transformation*. Moscow: MIR Publishers, revised from the 1974 Russian edition.

72. S. L. MARPLE, JR. 1987 *Digital Spectral Analysis with Applications*. Englewood Cliffs: Prentice-Hall.

73. S. M. KAY 1988 *Modern Spectral Estimation, Theory and Application*. Englewood Cliffs: Prentice-Hall.

74. J. H. MCCLELLAN 1988 in *Advanced Topics in Signal Processing* (Jae S. Lim and Alan V. Oppenheim, editors), 1–57. Englewood Cliffs: Prentice-Hall. Parametric Signal Processing.

75. B. W. BOMAR 1991 Class notes for ECE 692 Special Topics in Advanced Signal Analysis. University of Tennessee Space Institute, Tullahoma, Tennessee.

76. F. J. HARRIS 1977 *Trigonometric Transforms, A Unique Introduction to the FFT*. San Diego: Spectral Dynamics Corporation.

77. R. W. HAMMING 1983 *Digital Filters*. Englewood Cliffs: Prentice-Hall, second revised and enlarged edition.

78. R. M. ALFORD, K. R. KELLY, AND D. M. BOORE 1974 *Geophysics* **39**, 834–842. Accuracy of finite-difference modelling of the acoustic wave equation.

79. K. R. KELLY, R. W. WARD, S. TREITEL, AND R. M. ALFORD 1976 *Geophysics* **41**, 2–27. Synthetic seismograms: A finite-difference approach.

80. A. BAYLISS, K. E. JORDAN, B. J. LEMESURIER, AND E. TURKEL 1985 *Bulletin of the Seismological Society of America* **76:4**, 1115–1132. A fourth-order accurate finite-difference scheme for the computation of elastic waves.

81. I. R. MUFTI 1985 *Geophysical Prospecting* **33**, 619–656. Seismic modelling in the implicit mode.

82. M. A. DABLAIN 1986 *Geophysics* **51**, 54–66. The application of high-order differencing to the scalar wave equation.

83. J. VIRIEUX 1986 *Geophysics* **51**, 889–901. P-SV wave propagation in heterogeneous media: Velocity-stress finite difference method.

84. O. HOLBERG 1987 *Geophysical Prospecting* **35**, 629–655. Computational aspects of the choice of operator and sampling interval for numerical differentiation in large-scale simulation of wave phenomena.

85. P. MORA 1989 *59th Annual International Meeting, Society of Exploration Geophysicists, Expanded Abstracts*, 1039–1043. Modelling anisotropic seismic waves in 3-D.

86. K. J. BATHE AND E. L. WILSON 1976 *Numerical Methods in Finite Element Analysis*. Englewood Cliffs: Prentice-Hall.

87. O. C. ZIENKIEWICZ 1977 *The Finite Element Method*. New York: McGraw-Hill Book Company, third revised edition.

88. Z. P. BAŽANT 1978 *Computer Methods in Applied Mechanics and Engineering* **16**, 91–100. Spurious reflection of elastic waves in nonuniform finite element grids.

89. T. BELYTSCHKO AND R. MULLEN 1978 in *Modern Problems in Elastic Wave Propagation*, 67–82. New York: John Wiley and Sons. On dispersive properties of finite element solutions.

90. K. J. MARFURT 1984 *Geophysics* **49**, 533–549. Accuracy of finite -difference and finite-element modelling of the scalar and elastic wave equations.

91. R. MADARIAGA 1984 *Geophysical Journal of the R.A.S.* **79**, 589–612. Gaussian beam synthetic seismograms in a vertically varying medium.

92. I. TOLSTOY AND C. S. CLAY 1966 *Ocean Acoustics*. New York: McGraw-Hill Book Company.

93. C. S. CLAY AND H. MEDWIN 1977 *Acoustical Oceanography: Principles and Applications*. New York: John Wiley and Sons.

94. L. E. KINSLER, A. R. FREY, A. B. COPPENS, AND J. V. SANDERS 1982 *Fundamentals of Acoustics*. Toronto: John Wiley and Sons, third expanded and revised edition.

95. R. J. URICK 1982 *Sound Propagation in the Sea*. Los Altos: Peninsula Publishing, revised and edited edition.

96. R. J. URICK 1983 *Principles of Underwater Sound*. New York: McGraw-Hill Book Company, third expanded and revised edition.

97. W. S. BURDIC 1991 *Underwater Acoustic System Analysis*. Englewood Cliffs: Prentice-Hall, second revised and expanded edition.

98. W. T. THOMSON 1950 *Journal of Applied Physics* **21**, 89–93. Transmission of elastic waves through a stratified solid.

99. N. A. HASKELL 1953 *Bulletin of the Seismological Society of America* **43**, 17–34. The dispersion of surface waves in multilayered media.

100. F. R. DINAPOLI AND R. L. DEAVENPORT 1980 *Journal of the Acoustical Society of America* **67**, 92–105. Theoretical and numerical Green's function solution in plane layered medium.

101. H. SCHMIDT AND J. GLATTETRE 1985 *Journal of the Acoustical Society of America* **78**, 2105–2114. A fast field model for three-dimensional wave propagation in a stratified environment based on the global matrix method.

102. H. SCHMIDT AND F. B. JENSON 1985 *Computers and Mathematics with Applications* **II**, 699–715. Efficient numerical solution techniques for wave propagation in horizontally stratified environments.

103. O. VILMANN, P. GERSTOFT, S. KRENK 1989 Ødegaard and Danneskiold-Samsøe Reports 89.238 and 89.239, Copenhagen, Denmark. High-speed Forward Modelling Applied in Seismic Data Processing.

104. T. M. BROCHER, B. T. IWATAKE, AND D. A. LINDWALL 1983 *Journal of the Acoustical Society of America* **74**, 960–972. Experimental studies of low-frequency waterborne and sediment-borne acoustic wave propagation on a continental shelf.

105. J. E. MATTHEWS, P. J. BUCCA, AND W. H. GEDDES 1985 NORDA Report 120, Naval Oceanic Research and Development Activity, Numerical Modelling Division, Ocean Acoustics and Technology Directorate, NSTL, Mississippi. Preliminary Environmental Assessment of the PROJECT GEMINI Site.

106. R. A. MARSCHALL AND M. R. BRADLEY 1986 PSI Technical Report TR-S377073, Planning Systems Inc., McLean, Virginia. Noise, and Signal to Noise (S/N) Performance of Submerged and Buried Normal-stress and Particle Velocity Component Sensors.

107. L. M. BREKHOVSKIKH 1960 *Waves in Layered Media.* London: Academic Press.

108. W. C. ELMORE AND M. A. HEAD 1969 *Physics of Waves.* New York: Dover Publications, Inc., unabridged and corrected publication.

109. D. S. JONES 1986 *Acoustic and Electromagnetic Waves.* Oxford: Clarendon Press.

110. W. LICK 1990 in *Handbook of Applied Mathematics, Selected Results and Methods* (Carl E. Pearson, editor), 815–877. New York: Van Nostrand Reinhold, second revised and extended edition. Wave propagation. See section 15.3.15 (Inhomogeneous Media).

111. F. S. CRAWFORD, JR. 1968 *Waves.* New York: McGraw-Hill Book Company, Volume 3 of the Berkeley Physics Course.

112. A. D. PIERCE 1981 *Acoustics, An Introduction to Its Physical Principles and Applications.* New York: McGraw-Hill Book Company.

113. A. N. LOWAN, P. M. MORSE, H. FESHBACH, AND M. LAX 1946 USN Report C-67897, United States Navy Department, Office of Research and Inventions, Washington, D.C. Scattering and Radiation from Circular Cylinders and Spheres, Tables of Amplitudes and Phase Angles.

114. R. P. BANAUGH AND W. GOLDSMITH 1963 *Journal of the Acoustical Society of America* **35**, 1590–1601. Diffraction of steady acoustic waves by surfaces of arbitrary shape.

115. G. T. SCHUSTER AND L. C. SMITH 1985 *Journal of the Acoustical Society of America* **77**, 850–864. A comparison among four direct boundary integral methods.

116. M. F. BARNSLEY, R. L. DEVANEY, B. B. MANDELBROT, H. O. PEITGEN, D. SAUPE, AND R. F. VOSS 1988 *The Science of Fractal Images.* Berlin: Springer-Verlag.

117. G. T. SCHUSTER AND L. C. SMITH 1985 *Journal of the Acoustical Society of America* **78**, 1387–1394. Modelling scatterers embedded in plane-layered media by a hybrid Haskell-Thomson and boundary integral equation method.

118. T. W. DAWSON 1991 *Journal of the Acoustical Society of America* **90**, 1560–1574. Scattering matrix and boundary integral equation methods for long-range propagation in an acoustic waveguide with repeated boundary deformations.

119. T. W. DAWSON 1991 *Journal of the Acoustical Society of America* **90**, 1575–1581. Scattering matrix and boundary integral equation methods for acoustic propagation over a slope.

120. F. TAPPERT 1977 in *Wave Propagation and Underwater Acoustics* (J. B. Keller and J. S. Papadakis, editors), 224–287. New York: Springer. The parabolic approximation method.

121. R. B. EVANS 1983 *Journal of the Acoustical Society of America* **74**, 188–195. A coupled mode solution for acoustic propagation in a waveguide with stepwise variations of a penetrable bottom.

VITA

Born in 1958, Richard Anton Marschall wasted no time in earning a Bachelor of Science in Mathematics in 1978 from the University at Buffalo, State University of New York. A few months later, he was also awarded a Bachelor of Science in Electrical Engineering from the same institution. During this period, he was elected to membership in the honorary professional societies $\pi\mu\epsilon$ and $\tau\beta\pi$. He received a Master of Science in Applied Mathematics in 1981 and a Master of Science in Mechanical and Aerospace Engineering in 1987, both from the University of Virginia. Richard Anton Marschall has published refereed journal articles in neurophysiology, geophysics, and acoustics. In addition to holding several patents, he has authored numerous reports, mostly in the areas of fluid-structure interactions, acoustics, and remote sensing.